

# The consequences of adjoining pixel processing in persistent scatterer interferometry

A case study on the Hondsbossche zeewering

Tjerk C.K. Bermon



Front page: Image of the Hondsbossche zeewering (2003) before the reinforcements were added.

# The consequences of adjoining pixel processing in persistent scatterer interferometry

A case study on the Hondsbossche zeewering

Earth and Planetary Observation Technology  
Masters Thesis



**Tjerk Cornelis Kuylenburg Bermon**

Mathematical Geodesy and Positioning (MGP)  
Department of Earth Observation and Space Systems (DEOS)  
Faculty of Aerospace Engineering  
Delft University of Technology

Supervisors: Prof. dr. ir. R.F. Hanssen  
Ir. F.J. van Leijen





# Contents

<b>1</b>	<b>Introduction</b>	<b>1</b>
1.1	Motivation . . . . .	1
1.2	Problem formulation . . . . .	2
1.3	Methodology . . . . .	4
1.4	Outline . . . . .	5
<b>2</b>	<b>Advances in Synthetic Aperture Radar Processing</b>	<b>7</b>
2.1	Spaceborne Interferometric Synthetic Aperture Radar . . . . .	7
2.1.1	Principles of InSAR . . . . .	8
2.1.2	Resolution and Posting . . . . .	9
2.1.3	Limitations of InSAR . . . . .	12
2.2	Persistent scatterer technique . . . . .	14
2.2.1	PSI processing . . . . .	14
2.2.2	PS Estimation . . . . .	17
2.2.3	Advantages and Limitations of PSI . . . . .	19
2.3	Nibbling in PSI . . . . .	19
2.3.1	Expected Advantages and Limitations . . . . .	20
<b>3</b>	<b>Nibbling approach</b>	<b>21</b>
3.1	Implementation and methodology . . . . .	21
3.1.1	Area of interest . . . . .	23
3.1.2	Selection of seed pixels . . . . .	24
3.1.3	Expanding and merging of regions . . . . .	25
3.1.4	Acceptance criteria . . . . .	26
3.2	Spatial correlation of neighboring pixels . . . . .	27
3.2.1	Correlation in range . . . . .	29
3.2.2	Correlation in azimuth . . . . .	31
3.2.3	Differences in range and azimuth correlation . . . . .	33
3.3	Ambiguities for neighboring resolution cells . . . . .	34
3.3.1	Baseline dependent causes for ambiguities . . . . .	34
3.3.2	Ambiguity detection and adaption . . . . .	37
3.3.3	Ambiguity adaptation results . . . . .	40
3.4	Mathematical framework . . . . .	42
3.4.1	Functional model . . . . .	42
3.4.2	Stochastic model . . . . .	43

<b>4</b>	<b>Results and Discussion</b>	<b>47</b>
4.1	De Hondsbossche zeewering . . . . .	48
4.1.1	Characteristics of the area . . . . .	48
4.1.2	Available dataset . . . . .	49
4.2	Conventional PS processing . . . . .	50
4.2.1	Processing setup . . . . .	50
4.2.2	Results . . . . .	52
4.3	Nibbling . . . . .	54
4.3.1	Validation of the parameter estimation . . . . .	54
4.3.2	Nibbling results . . . . .	55
4.3.3	Analysis of adjoining pixels . . . . .	57
4.3.4	Increased coherence threshold . . . . .	63
4.3.5	Concluding remarks . . . . .	63
4.4	Improving the Nibbling approach . . . . .	64
4.4.1	Results of improved Nibbling . . . . .	64
4.5	Nibbling with increased kernel size . . . . .	65
4.5.1	Search area expansion . . . . .	65
4.5.2	Results with increased kernel size . . . . .	66
4.5.3	Topography . . . . .	66
4.5.4	Deformation . . . . .	68
4.6	Methodological differences . . . . .	69
4.6.1	Random noise . . . . .	71
4.6.2	Atmosphere and orbital errors . . . . .	71
4.6.3	Ambiguities . . . . .	72
4.6.4	Sidelobe observations . . . . .	72
4.6.5	Implementation and conceptual errors . . . . .	73
<b>5</b>	<b>Conclusions and Recommendations</b>	<b>75</b>
5.1	Conclusions . . . . .	75
5.2	Recommendations . . . . .	76
<b>A</b>	<b>Fourier Transform and Convolution</b>	<b>85</b>
A.1	Continuous Fourier Transform . . . . .	85
A.2	Convolution . . . . .	86
<b>B</b>	<b>Envisat ASAR Dataset</b>	<b>87</b>
<b>C</b>	<b>Algorithm construction</b>	<b>89</b>

# Preface

This Masters thesis is the final report for the Earth and Planetary Observation Technology Master track at the faculty of Aerospace Engineering, Delft University of Technology. This thesis was written under supervision of Ramon Hanssen and Freek van Leijen, within the Department of Earth Observation and Space Systems. It is the product of one year of research dedicated to the development of a new processing method based on adjoining pixel processing in persistent scatterer interferometry, a relatively new processing technique within the field of radar remote sensing.

During this Masters I developed an interest in radar remote sensing while attending the lectures on this subject. New dedicated radar remote sensing satellites are currently in development, which ensures new research in this field for at least the coming decades. The future of radar remote sensing is therefore established and with the upcoming increased resolution the applications seem to be endless. The research involved in developing new applications and approaches to exploit the improving earth observation data are both interesting and challenging.

One of the latest applications with the current sensors (ERS and Envisat) is deformation monitoring of Water Defense Structures (WDS). In the Netherlands the main natural hazard is flooding, therefore applications that are dedicated to enhance the security of the population are stimulated by the government. This thesis embeds radar remote sensing into global monitoring for security by developing an approach specifically designed to monitor deformation of WDS. The gathered (interpreted) information on the stability of the WDS is useful for ensuring the safety of the population. Hopefully this research will positively contribute to a new processing approach for this application.

## Acknowledgments

I would hereby like to take the opportunity to recognize and thank all the people that supported me during this last phase of my Masters. Firstly I would like to thank professor Ramon Hanssen for his constructive criticism and feedback within this research. His ideas and insights on this research lead me through the development of the Nibbling approach and the continuing improvements. Secondly many thanks to Freek van Leijen as my supervisor within this project, who substantially contributed to my understanding of the full processing cycle of persistent scatterer interferometry. His dedication and in depth understanding of the technique and the processing created a solid basis for this research.

I would also like to thank all colleagues within the Department of Earth Observation and Space Systems. Not only for their assistance with my research but also for their friendship and the

pleasant working environment they supplied. Special thanks to Petar Marinkovic for his dedication to answer all of the questions I had and his detailed explanations of radar remote sensing and Persistent Scatterer Interferometry (PSI). To Gert-jan van Zwieten and Davide Nitti for their assistance in the Fourier Transforms and specific mathematical problems I endured there. To Sami Esfahany for his discussions especially during the initial phase of my research. To Andy Hooper who assisted me in the period that my supervisors were unavailable. Also I would like to thank all of the remaining (ex-)colleagues of the Department of Earth Observation and Space Systems for their help in general: Mahmut Arıkan, Miguel Caro Cuenca, Shizhuo Liu, Gini Ketelaar, Rossen Grebenitcharsky, Zbigniew Perski, and Saad Aldin. And lastly I thank the co-reader, Jos Groot, for taking the time and effort to read this thesis.

Finally I would like to thank all of my family that supported and motivated me during my study, especially my parents Tjerk and Marianne, my brother Willem, and my sister Marieke. Also I would like to thank all my friends for their continuing support and stress reduction methods during the weekends.

Tjerk Bermon  
Delft, March 2009.

# Summary

Persistent scatterer interferometry (PSI) is a relatively new technique for deformation monitoring of the Earth's surface with mm/yr precision. Throughout the last decade this technique proved to be very effective by overcoming the three main limitations of conventional interferometry (geometrical-, temporal decorrelation, and atmosphere). To further develop PSI for specific applications, new approaches are investigated to improve the performance of currently developed techniques. This study focuses on ensuring the civil security, by monitoring the deformation of Water Defense Structures (WDS) specifically. This is therefore directly related to Global Monitoring for Environment and Security (GMES), an initiative to combine space- and ground-based observations to develop an integrated environmental monitoring capability to effectively manage the environment, mitigate the effects of climate change, and ensure civil security (ESA, 2008).

The approach investigated in this study is a one-dimensional persistent scatterer technique, applied to adjoining pixels. It is assumed that the phase difference between adjoining pixels is smaller than  $2\pi$  (a full phase cycle). The approach is not strictly one-dimensional, because of the width of the area of interest (the WDS). The topography and deformation estimations are done in a sequential order, hence the name of the approach: Nibbling. Nibbling is used to evaluate those pixels which are currently not identified as PS, in order to extract more information of the local topography and deformation. This information is important, especially in the case of very local deformation which indicate possible upcoming dike failures.

Neighboring pixels effectively overlap introducing a correlation between the observations. This correlation affects the parameters of interest (topography and deformation), but also the quality measure that is used. This is not accounted for in the functional or stochastic model, because of the varying correlation with the dominance of the scatterer in the resolution cell, and the not well known (co-)variances of the data. In order to remove the correlation effects, pixels with a separation of at least one pixel are used. This poses new challenges on the initial assumption of the ambiguities, for which two proposed methods are discussed. These unwrapping methods either use the fact that there is redundancy in the functional model, or that the ambiguities only occur at large baselines.

The feasibility of the methodology is evaluated by analysing timeseries of identified PS using conventional processing with respect to the timeseries obtained by Nibbling. It is observed with conventional processing that many resolution cells on the WDS contain coherent phase observations (Persistent Scatterers or PS), therefore it is assumed that pixels which are not identified as PS do contain valuable information of the deformation (false rejections). The current result of this approach increases the number of identified PS, however, the information gathered is not reliable when comparing the results to those obtained with conventional processing. Ambiguity errors propagate spatially because of the sequential processing setup, and is the main reason for

the unreliability of the results. The topography is also affected by sidelobe observations, which explains the (larger than actual) topographic trend towards the crown of the WDS.

# Nomenclature

## List of acronyms

APS	Atmospheric Phase Screen
CSA	Canadian Space Agency
DEM	Digital Elevation Model
DEOS	Delft Institute for Earth-Oriented Space Research
DePSI	Delft implementation of Persistent Scatterer Interferometry
DLR	Deutsches Zentrum für Luft- und Raumfahrt e.V. (German Aerospace Center)
DORIS	Delft Object-oriented Radar Interferometric Software
ERS	European Remote Sensing Satellite
ESA	European Space Agency
GDP	Gross Domestic Product
GMES	Global Monitoring of Environment and Security
IFT	Inverse Fourier Transform
ILS	Integer Least Squares
InSAR	Interferometric SAR / SAR interferometry
JPL	Jet Propulsion Laboratory
LOS	Line of Sight
MRM	Multi-image Reflectivity Map
NAP	Normaal Amsterdams Peil (Dutch vertical reference datum)
NASA	National Aeronautics and Space Administration
OMT	Overall Model Test
OSF	Oversampling Factor
PRF	Pulse Repetition Frequency
PS	Persistent scatterer
PSC	Persistent Scatterer Candidate
PSI	Persistent Scatterer Interferometry
radar	Radio detection and ranging
RAR	Real Aperture Radar
RMS	Root Mean Square
SAR	Synthetic Aperture Radar
s/c	Spacecraft
SCR	Signal-to-Clutter Ratio
SLC	Single-Look Complex
SNR	Signal-to-Noise Ratio
STC	Spatio-Temporal Consistency
TU Delft	Delft University of technology

VCE	Variance Components Estimation
WDS	Water Defense Structure
cm	centimeter
km	kilometer
l	liter
m	meter
mm	millimeter
s	second
yr	year

## List of acronyms

$\cdot^*$	Pseudo observation
$a$	Integer parameters
$A$	Design Matrix (for integer parameters)
$b$	Real-valued parameters
$B$	Design Matrix (for real-valued parameters)
$B_{\perp}$	Perpendicular baseline
$B_a$	Processed azimuth (Doppler) bandwidth
$B_{\text{Dop}}$	Actual Doppler bandwidth
$B_r$	Range (chirp) bandwidth
$c$	speed of light
$D$	(Linear) deformation rate
$D_k$	Deformation at epoch $k$
$D_a$	Normalized amplitude dispersion
$d_a$	Azimuth posting
$d_{\text{gr}}$	Ground range posting
$d_{\text{sr}}$	Slant range posting
$E\{\cdot\}$	Expectancy operator
$e_{x,y}^{0k}$	Residual phase
$f_a$	Azimuth frequency
$f_{DC}$	Doppler centroid frequency
$f_{pr}$	Pulse Repetition Frequency
$f_r$	Range frequency
$f_s$	Sampling frequency
$H$	Topographic height
$H_0$	Null hypothesis
$H_A$	Alternative hypothesis
$H_{2\pi}$	Height ambiguity
$I$	Identity Matrix
$K$	Number of interferograms
$L_a$	Antenna length
$M_{xy}$	Master offset term
$Q_{\varphi}$	(co-)variance matrix of the phase observations
$r$	Redundancy (observations - unknowns)
$R$	(Slant) range
$R_{\text{Dop}}$	Doppler bandwidth ratio



---

$S$	Atmosphere
$t^0k$	Time difference between master (0) and slave ( $k$ )
$t_a$	Azimuth time
$t_r$	Range time
$T_{q=m-n}$	Overall model test quantity
$v_s/c$	Velocity of spacecraft
$w$	W-test statistic
$W$	Weighting function
$W_y$	Weights Matrix
$\alpha$	Hamming window constant
$\beta_a$	Azimuth beam width
$\gamma$	Temporal coherence threshold
$\hat{\gamma}_{x,y}$	Estimated temporal coherence
$\delta(.)$	Dirac delta function
$\Delta a$	Focused azimuth resolution
$\Delta r_{gr}$	Ground range resolution
$\Delta r_{sr}$	Slant range resolution
$\zeta$	Spatio temporal consistency
$\eta_x^k$	Ground range subpixel position at epoch $k$
$\theta$	Look angle
$\Pi(.)$	Boxcar function
$\hat{\sigma}^2$	Aposteriori variance factor
$\sigma_a$	Amplitude standard deviation
$\sigma_{\psi_q}^2$	SLC phase variance
$\sigma_{\psi_i, \psi_j}$	Spatial covariances
$\sigma_{\psi^0, \psi^k}$	Temporal covariances
$\tau$	Pulse length
$\varphi$	Interferometric phase observation
$\varphi^0k_ij$	Double difference phase observation
$\lambda$	Radar wavelength
$\mu_a$	Amplitude mean
$\phi^k$	Deformation component of the phase at epoch $k$
$\psi$	SLC phase
$\psi_{\Delta S}$	Atmosphere component of the SLC phase
$\psi_{\Delta n}$	Noise component of the SLC phase



# Chapter 1

## Introduction

Spaceborne Synthetic Aperture Radar Interferometry (InSAR) is a geodetic technique capable of detailed deformation measurements of the Earth's surface. It is based on microwave pulses (cm to dm wavelength) emitted by a Synthetic Aperture Radar (SAR) instrument, which are scattered back from the Earth's surface to the SAR antenna. The backscattered signal consists of amplitude and phase measurements, which easily covers areas of over  $100 \times 100$  km with a pixel size on the ground of potentially  $4 \times 20$  meter for ERS and Envisat. By using phase measurements of the received signal, the accuracy of the range differences between sensor and resolution cell is in the mm-range (Hanssen, 2001). Direct range measurements have an accuracy three orders of magnitude larger.

Large coverage combined with small resolution cells (pixel size) enables analysis of wide-scale displacements. Surface deformation measurement applications using this technique can be categorized into earthquakes, volcanoes, (anthropogenic) subsidence/uplift, and glacier/ice motion (Hanssen, 2001). More recent applications are detailed deformation analyses of land subsidence due to mining, gas, water, and oil withdrawal. These applications of local deformation make use of a technique called Persistent Scatterer InSAR (PSI).

PSI searches for sub-pixel sized dominant scatterers, coherent over timespans of up to several years (hundreds of interferograms). The phase information of these stable scatterers (Persistent Scatterers or PS) is valuable because it can be used over long periods of time. With this phase information PSI overcomes the three main limitations of InSAR which are (1) atmospheric phase delay because the atmospheric component is temporally uncorrelated, (2) temporal decorrelation because of the phase stability over time (coherent phase), and (3) geometrical decorrelation because the size of the targets is small (Ferretti et al., 2000a, 2001). By overcoming these limitations the analysis and interpretation of local subsidence and deformation becomes possible. The main focus of this thesis is the development of a new processing technique based primarily on PSI for Water Defense Structures (WDS) in the Netherlands.

### 1.1 Motivation

The Netherlands consists largely of reclaimed land, and is therefore dependent on dedicated WDS for its safety. According to the CIA's 2008 world factbook (CIA, 2008), the main natural hazard in the Netherlands is flooding. Two thirds of the country is protected against flooding by these water defense structures, an area in which nine million people live, and two thirds of the

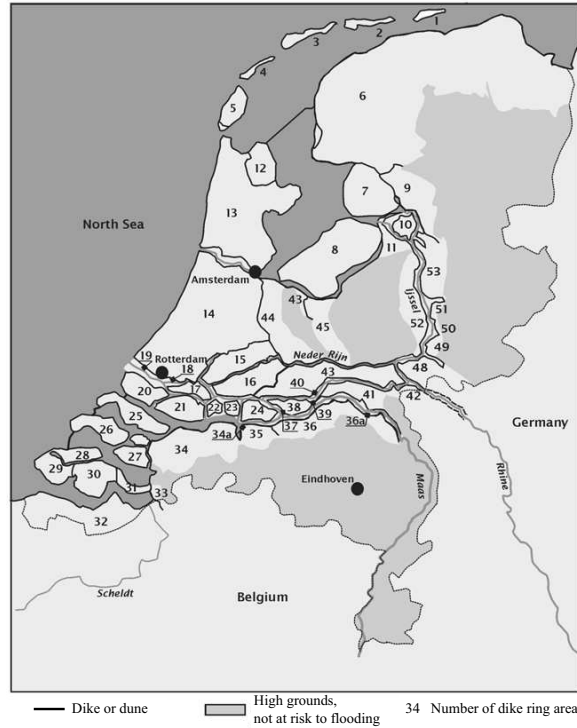


Figure 1.1: The western and northern coastal areas, and areas surrounding the large rivers, of the Netherlands are at risk to flooding.

Gross Domestic Product (GDP) is earned. The area with the largest risk of flooding is indicated in Figure 1.1, and covers most of the western part of the Netherlands and areas surrounding the larger rivers. Three recent dike failures, respectively Wilnis (26/08/2003, see figure 1.2), Terbregge (01/09/2003), and Stein (27/01/2004), showed that regular inspections failed to detect hazardous areas.

The Dutch Transport and Water Management Inspectorate published a report, which concluded that almost a quarter of the WDS fails to meet the requirements (Transport and Water Management Inspectorate, 2006). This publication, together with the most recent dike failures were the main reasons to investigate new complementary methods for dike monitoring. InSAR data is widely available at relatively low cost, making it a feasible alternative to conventional methods for investigating the structural stability of WDS.

## 1.2 Problem formulation

Delft University of Technology (TUDelft) is interested in developing methods to analyze the stability of WDS using PSI. This tool is very powerful, because of the possibility to detect deformation on a sub-millimeter level, and the availability of SAR images taken as early as 1992 (the launch of ERS-1). Analysis of recent dike failures and their accompanying signal gives insight



Figure 1.2: Aerial photograph of the dike failure in Wilnis (2003), the Netherlands. A large section of the dike was displaced due to changes in the internal dike structure as a result of a long period of drought.

into the measurable deformation mechanisms (e.g., sliding, settling, seepage, etc.), leading to possible dike failures, using PSI.

A study on the potential of radar interferometry for monitoring dikes of the Netherlands (POSEIDON) (Dentz et al., 2006) shows that it is possible to recognize a limited number of deformation mechanisms on WDS. Furthermore, it showed that the number of persistent scatterers (PS) depends on the protective cover of the dike, rather than its orientation. Even though the number of PS per kilometer seemed to be relatively constant, the distribution was not. This inhomogeneous distribution of PS is assumed to be the result of false rejections and therefore new processing techniques could improve the number of detections. False rejections of PS can be a result of changes in, for example, the protective cover of the WDS, which results in the phase of the backscatter being coherent only over shorter periods of time. Such a disturbance changes the characteristics of a target such that the coherence over the full timespan is lost.

The new approach is based primarily on supervised classification of areas of interest, mainly line-infrastructure. The classification is based on a-priori knowledge of the scattering characteristics and the potential density of coherent targets. By only considering line-infrastructure (WDS in this case), the technique reduces to a nearly one-dimensional one. Furthermore, only small lengths over which the double-difference phases (arcs) are used for analysis of the deformation are incorporated. This technique estimates the parameters of interest (e.g., topography, deformation) of pixels close to a reference point and continues this pixel-by-pixel, integrating the parameters of interest along a path, hence the name of the algorithm: *Nibbling*. For this study the area of interest is limited to a WDS in the Netherlands, the Hondsbossche zeewering. The general problem statement of this research is;

*Is there valuable information to be retrieved from line-infrastructure where no PS are found using conventional tools for PSI, by incorporating small arcs?*

This can be divided into the following subquestions;

1. Are the pixels on a WDS that are not identified as PS using conventional PSI processing coherent enough that information regarding the deformation can be evaluated reliably in terms of ensemble coherence or a posteriori variance?
2. What is the consequence of an adjoining/neighbors pixel processing technique on the estimations of the topography, deformation, and the quality measure (temporal coherence)?
3. Does incorporating small arcs, i.e. the double difference between neighboring pixels, imply that the phase differences are within the same phase cycle?

### 1.3 Methodology

In total 51 focused Single Look Complex (SLC) images are available of the scene, which contains the Hondsbossche zeewering (the area of interest). The coregistration and interferogram formation procedures are performed using the Delft Object-oriented Radar Interferometric Software (DORIS) (Kampes and Usai, 1999; Kampes et al., 2003). After this pre-processing a (single master) stack of interferograms is available, on which the Nibbling approach will be applied.

The Nibbling approach should improve the probability of successfully identifying PS on line-infrastructure. This increase will improve the density and homogeneity of the PS distribution. It is based on differences of interferometric phases with a very small spatial separation (arcs), preferably adjoining pixels. Because these arcs are short (max. 50 meters), the following assumptions can be made:

1. topographic differences are expected to be smaller than the height ambiguity of the interferometric pair,
2. differences in deformation are expected to be small (spatially correlated), such that the phase component of the deformation is smaller than half a  $2\pi$  phase cycle, and
3. atmosphere is spatially correlated and will therefore largely cancel out in the differences.

It is assumed that the phase difference between two adjoining pixels is smaller than half a phase cycle, hence the above-mentioned phase components are very small. If the phase differences are smaller than half a phase cycle ( $< \pi$ ), then the smallest phase difference between the observations is assumed to be the correct one. As a result, the ambiguities of the phase differences are solved by wrapping the phase differences again, i.e., the phase differences are bound to the range  $[-\pi, \pi)$  by adding or subtracting an integer number of  $2\pi$ . The ambiguities of the phase differences after this procedure are assumed to be corrected, removing the rank-deficiency from the system of equations.

This project will be divided in the following phases:

**Phase 1:** Derivation of the mathematical framework.

In the first phase, the functional and stochastic model of the mathematical framework are derived. Initially not all components were modeled, because of the testing procedure on synthetic data. During the development of the approach, more components were added to the models in the mathematical framework to improve the estimation procedure.

**Phase 2:** Programming and testing on synthetic data.

In the second phase the basic algorithm is programmed. Synthetic data are used for testing of the algorithm, although this may not represent reality. However, in simulations the inputs are known and the output can be validated. Furthermore, different inputs can be added in a systematical way to the simulated interferograms to check the capability and reliability of the algorithm.

**Phase 3:** Testing on datasets in the Netherlands.

This phase will be dedicated to a case study on a WDS in the Netherlands and comparison of the results with those obtained using conventional PSI tools. The study area will be a primary WDS near Petten, “De Hondsbossche Zeewering”, of which the deformation signals have been estimated before, using PSI. These results can be used for quality-, improvement assessment, and validation.

**Phase 4:** Improvements and optimization of the Nibbling approach.

This phase is required to improve the initial results and implement optimizations in the algorithm. The considered optimizations consist of ambiguity resolution for large baselines, accounting for the correlation between neighboring pixels, and optimizing the use of large quantities of data and the speed and handling of the Nibbling approach.

## 1.4 Outline

Chapter 2 starts with a background on InSAR, PSInSAR, and a brief introduction to Nibbling. The emphasis of this chapter is on PS processing, which is the basis for the development of the Nibbling approach. Throughout this chapter the advances of InSAR and its processing are discussed. Important background information, such as resolution and posting in interferograms is briefly described. Chapter 3 continues with the the Nibbling approach. The implementation of it is extensively described, together with the development of the functional and stochastic model. Two methods are proposed for removing any remaining ambiguities in the double difference phases. Chapter 4 focuses on the case study “De Hondsbossche Zeewering”, and the results with respect to conventional PS processing. The challenges with the adjoining pixel approach is shown, and improvements thereof are discussed. The final interpretable results are shown, after improving the Nibbling and conclusions are based upon this. Chapter 5 continues with the final conclusions and recommendations of this study.





## Chapter 2

# Advances in Synthetic Aperture Radar Processing

Radar (Radio detection and ranging) is a tool developed in the early 1900's, of which Synthetic Aperture Radar (SAR) is an extension. In 1978 the first satellite capable of interferometric SAR (InSAR) was launched by NASA, Seasat. The main purpose of this SAR instrument was to monitor the global ocean surface wave field and polar sea ice conditions (JPL, 2008). Following this mission, more satellites equipped with SAR instruments were launched, such as the European ERS1 (1991), ERS2 (1995), and Envisat (2002) (ESA, 2008), the Canadian Radarsat-1 (1995) and Radarsat-2 (2007) (CSA, 2008), and the German Terrasar-X (2008) (DLR, 2008). The increasing availability of InSAR capable satellites leads to the development of new geodetic applications.

The advances in processing techniques and important background information are discussed in this chapter. Section 2.1 addresses the principles of InSAR and its limitations. Thereafter the Persistent Scatterer (PS) technique, which uses interferogram stacks to overcome the main limitations of InSAR, is discussed together with its limitations in section 2.2. Finally the Nibbling approach, which is the focus of this study, will be introduced in section 2.3. This technique uses adjoining resolution cells to identify PS in specific areas.

## 2.1 Spaceborne Interferometric Synthetic Aperture Radar

SAR is a coherent active microwave imaging system with advantages over optical systems. An active system illuminates the surface with its own radiation, which makes the system independent of solar illumination. By using microwave frequencies (cm-m wavelengths), the system is able to penetrate clouds and precipitation with minimal deterioration. Finally it allows for interferometry because the emitted radiation is coherent (amplitude and phase of the response of a target are retained as the satellite moves).

SAR operates differently compared to optical imaging systems in terms of the capability to distinguish spatially separated targets on the earth surface with a specific resolution. Radar systems measure total intensity (and phase) of the backscattered pulses for which phase-sensitive processing is required to focus the image (Bamler and Hartl, 1998; Cumming and Wong, 2005). Focused SAR images are often referred to as Single-Look Complex (SLC) images. Pixels in the

SLC's are complex valued (phasors), of which the phase can be deduced. In this research it is assumed that the SLC images are focused and coregistered, and readily available for processing. The coregistration is performed using the open source software package DORIS (Delft Object-oriented Radar Interferometric Software) (Kampes and Usai, 1999; Kampes et al., 2003).

ERS1, ERS2, and Envisat acquire their data in strip-map geometry, which illuminates the Earth from an oblique angle approximately perpendicular to the flight direction. The data used in the case study of this project are acquired with these satellites, therefore the focus will be on their characteristics. A large selection of literature is available that discuss the principles and/or characteristics of SAR (strip-map geometry) (Bamler and Hartl, 1998; Cumming and Wong, 2005; Curlander and McDonough, 1991; Elachi, 1988; Ferretti et al., 2007; Hanssen, 2001; Schreier, 1993) and InSAR (Bamler and Hartl, 1998; Curlander and McDonough, 1991; Hanssen, 2001; Massonnet and Feigl, 1998; Rosen et al., 2000; Zebker et al., 1997) in detail, to which the interested reader is referred. This section will briefly address the parts that are of interest for this research.

### 2.1.1 Principles of InSAR

The principle in deformation monitoring with InSAR is measuring phase differences due to changes of the Earth's surface. These phase differences are visualized in an interferogram, created by multiplying an SLC image with the complex conjugate of another (coregistered) SLC image. The resulting phase differences in an interferogram are within the interval  $[-\pi, \pi)$ , which is referred to as wrapped phase. The deformation is measured using the phase difference in the line of sight (LOS) to the spacecraft. The phase differences have, next to the deformation, other contributions depending on the geometry, scattering characteristics of the Earth's surface, and atmospheric conditions. All these contributions are superimposed, resulting in the observed total interferometric phase per resolution cell

$$\varphi = \varphi_{\text{topo}} + \varphi_{\text{defo}} + \varphi_{\text{atmo}} + \varphi_{\text{scat}} + \varphi_{\text{orb}} + \varphi_{\text{noise}} + 2\pi a, \quad (2.1)$$

in which the  $\varphi_{\text{topo}}$  is the topographic phase component, with a functional relation via the perpendicular baseline  $B_{\perp}$ , look angle  $\theta$ , and slant range  $R$  to the height  $H$  above a reference spheroid or ellipsoid

$$\varphi_{\text{topo}} = -\frac{4\pi}{\lambda} \frac{B_{\perp}}{R \sin \theta} H, \quad (2.2)$$

with  $\lambda$  the radar wavelength. The deformation in LOS  $\varphi_{\text{defo}}$  is the phase difference due to the deformation  $D$

$$\varphi_{\text{defo}} = -\frac{4\pi}{\lambda} D. \quad (2.3)$$

Furthermore,  $\varphi_{\text{atmo}}$  is the phase change due to atmospheric delay,  $\varphi_{\text{scat}}$  is the phase due to changes in the scattering characteristics,  $\varphi_{\text{orb}}$  represents the phase shift due to the error in orbit determination, and  $\varphi_{\text{noise}}$  is the remaining phase delay because of thermal noise, coregistration, and interpolation errors. The last term contains the integer  $a \in \mathbb{Z}$ , which is the unknown integer number of phase cycles.

The topography is often the dominant signal in an interferogram and is usually approximated using an external Digital Elevation Model (DEM), this is referred to as Differential InSAR. The remaining signal is a combination of all the other terms, including the residual topographic

height  $\Delta H$ . An unwrapping procedure, to resolve the ambiguities, and estimations of the other parameters are required to obtain the relative deformation signal in LOS. It is possible that the deformation signal is large enough to ignore the other effects (Bamler and Hartl, 1998; Massonnet and Feigl, 1998; Rosen et al., 2000; Hanssen, 2001), but it is not often the case because of atmospheric influences and changes in the scattering characteristics.

### 2.1.2 Resolution and Posting

Resolution is defined as the minimal distance at which two distinct scatterers with equal brightness can be discerned (Born et al., 1959). A resolution cell in radar interferometry is defined as the illuminated area on the earth's surface mapped to a single pixel. The resolution cell size is defined by the resolution in azimuth and range, which are not necessarily equal. A pixel is infinitesimal, and therefore dimensionless, it has no physical size (Hanssen, 2001). Pixel size, however, is often used in the same context as resolution. The distance between two pixels (or two resolution cell centers), is referred to as posting.

There is an important difference between resolution cell size and posting, because the resolution cells in a focused radar image effectively overlap, see figure 2.2. The posting between the resolution cells is smaller than the size of the resolution cells, which introduces a correlation between the resolution cells. Furthermore, if a resolution contains a dominant point scatterer, then that phase observation will influence (or dominate) the observations of pixels in range or azimuth farther away than the adjoining one.

#### Range

The resolution in range is the ability to discriminate between two adjacent point targets separated by a distance  $\Delta r$ . If this is the case, the received echoes will be separated in time by  $\Delta t = 2\Delta r/c$  with  $c$  representing the speed of light. Now assume that the radar emits a pulse with a duration  $\tau$ , then in order for the two echoes to be detected as two separate point targets  $\tau < 2\Delta r/c$ . The slant range resolution ( $\Delta r_{sr}$ ) is theoretically given by

$$\Delta r_{sr} = \frac{c\tau}{2}. \quad (2.4)$$

The ground range resolution is the projection of the slant range resolution onto the ground range. To simplify, the Earth is assumed flat, in this case the look angle will equal the incidence angle ( $\theta$ ). The ground range resolution ( $\Delta r_{gr}$ ), shown in figure 2.1, becomes

$$\Delta r_{gr} = \frac{c\tau}{2 \sin \theta}. \quad (2.5)$$

A high resolution is obtained with a short pulse length, however, this will reduce the signal energy and equivalently the signal-to-noise ratio (SNR). There is a physical limit to the pulse power, because of the radar hardware and therefore the pulse length cannot be shortened (Elachi, 1988). To solve this, pulse modulation (pulse compression) is applied. A common type of modulation is the "chirp", which is a linear frequency modulation. Phase-coding of the transmitted pulse changes the dependency of range resolution from pulse length to the inverse of its bandwidth  $B_r$  (the frequency range of the chirp). The resolution in slant range and ground range improve to

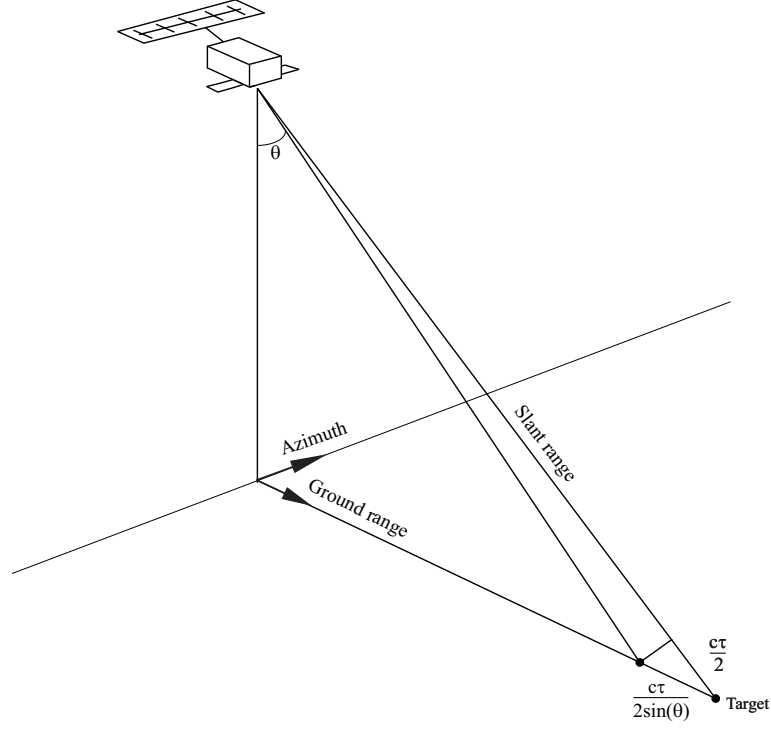


Figure 2.1: The backscattered signal requires the two targets to have a minimum spatial separation in slant range of  $c\tau/2$  and projected in (ground) range of  $c\tau/(2\sin\theta)$  for a pulse of duration  $\tau$ .

$$\Delta r_{\text{sr}} = \frac{c}{2B_r}, \text{ and} \quad (2.6)$$

$$\Delta r_{\text{gr}} = \frac{c}{2B_r \sin \theta},$$

respectively.

To distinguish different backscattering objects in a single range echo, the backscatter is convolved with a replica of the transmitted pulse (a matched filter). This is equivalent to the multiplication with a matched filter in frequency domain, where the matched filter is the Fourier transform of the transmitted pulse. The convolution of chirps results in a sinc function, of which the sidelobes can disturb the image. By weighting the spectrum of the return echo with a Hamming window, the sidelobes are reduced while retaining an improved range resolution (Swart, 2000).

The sampling frequency,  $f_s$ , must be chosen at least equal to the chirp bandwidth to prevent aliasing, assuming a bandlimited signal. It is common that the sampling frequency is larger than the bandwidth, in order to fully sample the spectrum, which is referred to as oversampling. The complex multiplication of two coregistered SLC images effectively doubles the spectrum length, because the equivalent of a multiplication in space is a convolution in the frequency domain. This is the reason for oversampling the SLC images with a factor of two before the computation

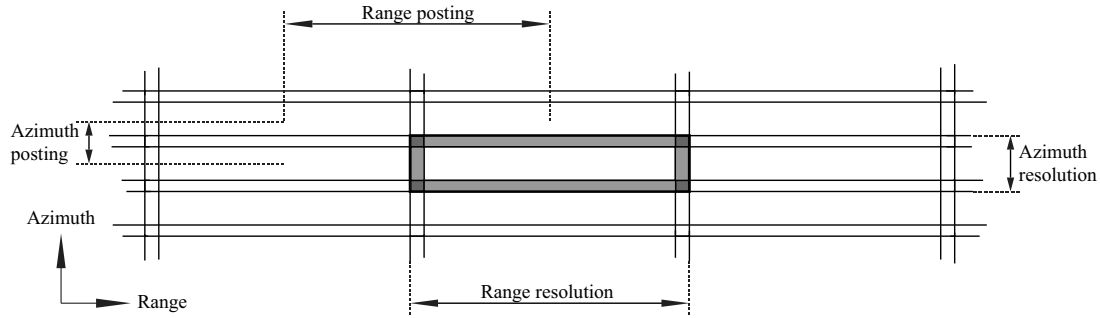


Figure 2.2: Illustration of the resolution in a focused radar image. The areas shown in gray are the parts that overlap with neighboring resolution cells. The resolution and posting in range is approximately two times greater than in azimuth for ERS and Envisat.

of the interferogram. A higher sampling frequency than the chirp bandwidth physically causes resolution cells to overlap. In other words, the posting of the resolution cells is smaller than the resolution cell size, see figure 2.2.

Similarly to the resolution, the equations for the posting (sampling distance) can be written for slant range ( $d_{r_{sr}}$ ) and ground range ( $d_{r_{gr}}$ ) as

$$\begin{aligned} d_{r_{sr}} &= \frac{c}{2f_s} \\ d_{r_{gr}} &= \frac{c}{2f_s \sin \theta}. \end{aligned} \quad (2.7)$$

### Azimuth

The resolution in azimuth is the ability to discriminate between two adjacent point targets at equal slant range  $R$  separated by a distance  $\Delta a$ . Suppose the radar antenna has length  $L_a$ , then the azimuth beam width (two-way) is defined as  $\beta_a = 0.886\lambda/L_a$ , with  $\lambda$  the wavelength. For a Real Aperture Radar (RAR) these targets can only be resolved if they are not both in the same radar beam at the same time, hence

$$\Delta a = R\beta_a = 0.443 \frac{R\lambda}{L_a}. \quad (2.8)$$

For a spaceborne platform this will yield an azimuth resolution of several kilometers, which is very undesirable for scientific applications (Curlander and McDonough, 1991). Wiley (1954) was able to improve this by observing that different point targets, at slightly different angles with respect to the radar velocity vector, have different distances at any instant relative to the radar platform. Therefore, the backscatter of each target will have a different Doppler frequency shift (phase history). This shift is used to separate different targets which are in the same radar beam at the same range. This technique to improve the azimuth resolution is known as the synthetic aperture technique and has the capability to improve the azimuth resolution to

$$\Delta a = \frac{v_s/c}{B_a}. \quad (2.9)$$

where  $B_a$  is the processed Doppler (azimuth) bandwidth, and  $v_{s/c}$  is the satellite velocity. The processed Doppler bandwidth is sometimes referred to as the Doppler bandwidth, but here a discrimination is made between the Doppler bandwidth ( $B_{\text{Dop}}$ ) and the processed Doppler bandwidth. The variation of Doppler frequency during the passage of a scatterer through the beam is expressed by the processed Doppler bandwidth. The Doppler bandwidth is a parameter related to the beam angle of the antenna pattern (Geudtner, 1995). The difference between Doppler bandwidth and processed Doppler bandwidth depends on the definition of the beamwidth. Equation (2.9) is simplified by using the two-way 4-dB beamwidth  $\beta_a = \lambda/L_a$  (Stimson, 1998). This improves the azimuth resolution to a theoretical value of

$$\Delta a \approx \frac{L_a}{2}. \quad (2.10)$$

This result states that smaller antennas will produce a higher resolution. However, there is a physical limit to the minimum size of the antenna, which is that the received power decreases with decreasing antenna size (Henderson and Lewis, 1998). Furthermore, the radar must transmit a pulse each time the platform moves a distance equal to half the antenna length, this is implied because the bandwidth of the Doppler signal relates to the swath width and must be smaller than the Pulse Repetition Frequency (PRF) (Curlander and McDonough, 1991).

The antenna pattern in azimuth causes the return signal strength of a point target to resemble the antenna pattern (a sinc-squared function), see figure 2.3. The largest strength is acquired when the target is in the center of the beam. The Doppler frequency history of the target is proportional to the targets radial velocity with respect to the radar platform. The frequency decreases as the platform passes by with zero Doppler frequency when the target is in the center of the beam (assuming a squint angle of zero). The sinc-squared signal return together with the targets Doppler frequency history is called the azimuth chirp. The backscatter is again convolved with a replica of the estimated azimuth chirp (a matched filter), and is a sinc function. The azimuth spectrum is filtered with a Hamming window to reduce the sidelobes, centered at the Doppler centroid frequency.

The posting between the resolution cells in azimuth direction depends on the Pulse Repetition Frequency (PRF or  $f_{\text{pr}}$ ). This is the rate at which consecutive chirps are generated, and is at least equal but often higher than the processed azimuth bandwidth. The azimuth posting is related to the PRF by

$$d_a = \frac{v_{s/c}}{f_{\text{pr}}}. \quad (2.11)$$

### 2.1.3 Limitations of InSAR

InSAR proved very effective in measuring deformation in regions of good coherence (Massonnet and Vadon, 1995; Amelung et al., 2000), however, almost in any interferogram there will be regions present with low coherence. There are two mechanisms which cause decorrelation in a scene, temporal decorrelation and spatial (or geometrical) decorrelation. These decorrelation sources reduce the capability of precisely determining the deformation in LOS. Furthermore, the spatially and temporally varying atmospheric signal reduces the quality of the deformation estimation.

Temporal decorrelation follows from physical surface changes (scatterer positions and electromagnetic characteristics) during the time difference of two SLC images within a resolution cell.

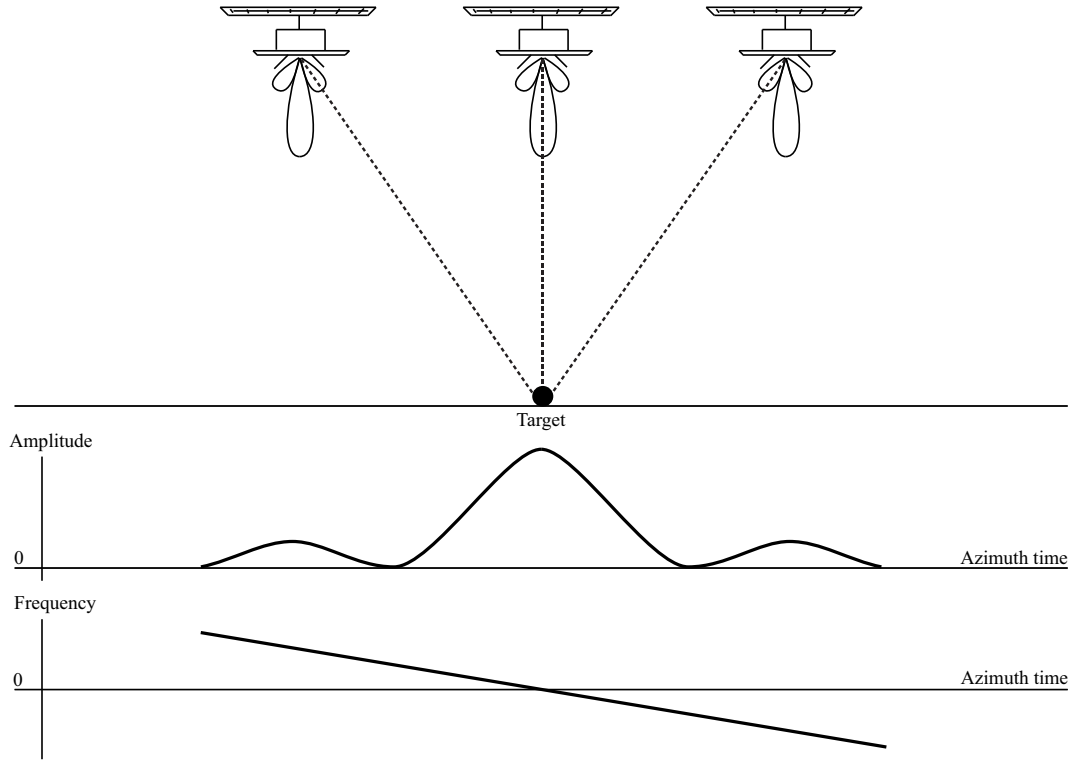


Figure 2.3: The beam pattern and its effect on the signal strength and Doppler frequency, which has a negatively sloped relationship with respect to the azimuth time. Adapted from Cumming and Wong (2005).

Radar images are taken in repeating cycles of the satellite orbit, with a minimum time difference of 35 days for ERS and Envisat to image the same scene. This time difference allows the surface to change (e.g. snow accumulation, vegetation growth) introducing decorrelation in the interferogram. Although the area may look completely decorrelated, this does not imply that there are no coherent scatterers in this area. The stable scatterers, if identified, can still be used to accurately measure surface deformation of the area. Zebker and Villasenor (1992) provide a method to estimate the temporal decorrelation based on the changes in position of a scatterer and show that the extent of temporal decorrelation is dependent on the direction the scatterer changes. Surfaces with significant volume scattering, such as forests, may decorrelate most rapidly depending on the radar wavelength.

Geometrical decorrelation follows from the difference in viewing angle of the antenna including a variation in the incidence angle, as well as in the squint angle, the off-perpendicular angle to the velocity vector. This causes the measured interference results to differ and consequently introduces a loss of coherence, assuming there is no misregistration of the SLC images. Spectral filtering of the non-coherent parts of the images eliminates this effect. Li and Goldstein (1990) also conclude that even though a large separation in perpendicular baseline increases the height measurement accuracy, it should not be larger than the critical baseline. The critical baseline expresses the maximum horizontal separation of two orbits in order to perform interferometry. This baseline causes a spectral shift equivalent to the chirp bandwidth ( $B_r$ ).

The atmosphere causes a phase delay in the radar pulse. On each radar image an Atmospheric Phase Screen is superimposed, as a consequence to the atmospheric inhomogeneities. Hanssen (2001) shows that the atmospheric phase variation is dominantly dependent on the local distribution of water vapor in the atmosphere. The temporal correlation is in the order of hours, therefore the atmosphere of two different radar images, with a temporal baseline of at least 35 days for ERS, is effectively decorrelated.

## 2.2 Persistent scatterer technique

Persistent Scatterer Interferometry (PSI) is the latest advancement in the field of radar remote sensing. It was recognized only in the late 1990's, that some-artificial or natural-features have stable scattering characteristics over long periods of time (Usai and Hanssen, 1997; Usai, 1997). This means that the scattering phase contribution  $\phi_{\text{scat}}$  of equation (2.1) is close to zero. PSI (Ferretti et al., 2000b, 2001) descends directly from this observation, and is a technique which overcomes the main limitations of conventional InSAR, by using these coherent point scatterers to accurately determine the deformation in LOS over long periods of time.

Interferograms that visually seem to be dominated by noise can still contain valuable information of the surface deformation. Single resolution cells may be time-coherent but surrounded by noise, and therefore visually uninterpretable. PSI searches for these pixels in order to obtain the information contained in the phase measurements of a stack of coregistered interferograms. Those resolution cells which are coherent over long periods of time are referred to as Persistent Scatterers (PS).

A resolution cell can either contain one dominant scatterer (point scatterer), which will be mostly observed in urban areas, or many smaller targets (distributed scatterer) such as roads. Both coherent point-like scatterers and coherent distributed scatterers are referred to as a PS. In reality a resolution cell will contain any combination of point-like and distributed scatterers. Scatterers with a coherent phase do not necessarily require a (dominant) point scatterer, which is usually attributed to a single-often man-made-object much smaller than the resolution cell size. However, a dominant point scatterer is less sensitive to any geometrical decorrelation in contrast to coherent distributed scatterers. Furthermore, a coherent point scatterer behaves uniformly in the frequency domain which is not affected by the decorrelation effect due to the spectral shift (Gatelli et al., 1994).

PSI proves to be a useful geodetic tool in many applications, acquiring reliable deformation rates in the order of mm/year. The deformation measurements using this technique are shown to be successful in a wide variety of applications (Ferretti et al., 2001; Colesanti et al., 2003; Hooper et al., 2004; Kampes, 2005; Bovenga, 2005; Dentz et al., 2006; Humme, 2007; Esfahany, 2008; Ketelaar, 2008). The deformation measurements for these applications are based on the same method, however, different processing techniques have been developed for estimating the deformation from PS observations (Ferretti et al., 2001; Berardino et al., 2002; Kampes, 2005). The PS technique as summarized here is developed at Delft University of Technology.

### 2.2.1 PSI processing

The Delft implementation of PSI (DePSI) processing is extensively described (Kampes and Hanssen, 2004; Kampes, 2005; Humme, 2007; Esfahany, 2008; Ketelaar, 2008). In this sec-



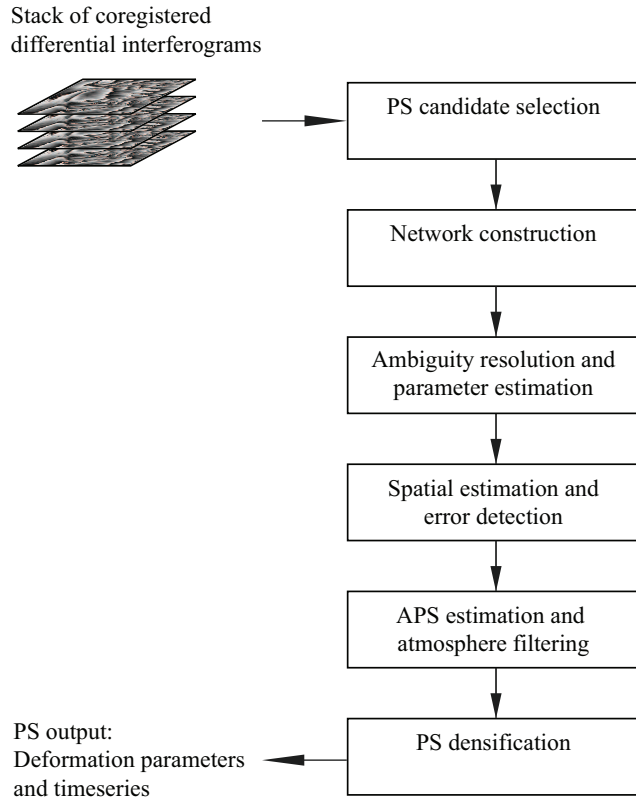


Figure 2.4: PSI processing chain

tion a summary of the processing steps and the philosophy behind it are presented. Figure 2.4 gives an overview of the processing chain. It is assumed that a stack of pre-processed differential interferograms is available, coregistered to a single master chosen based on the stack coherence (Kampes, 2005).

### PS Candidates Selection and Parameter Estimation

The resolution cells that are expected to be time-coherent, and therefor contain the surface deformation information, need to be selected with confidence. The initially selected pixels are the PS candidates (PSC) and can be selected based on criteria such as (1) Signal-to-Clutter Ratio (SCR) (SCR, 1993), (2) normalized amplitude dispersion (Ferretti et al., 2001) or (3) supervised classification (Humme, 2007). The SCR method estimates the phase stability of the pixel based on the assumption that the PS is surrounded by circular, Gaussian distributed clutter. The assumption of surrounding clutter is not strictly valid, especially in urban areas, therefore the normalized amplitude dispersion is used. A direct relation exists between the normalized amplitude dispersion and the SCR,  $D_A = 1/\sqrt{2SCR}$  (SCR, 1993). A third option is to manually

classify and select PS candidates, but this is only done if the position of the PSC is crucial. For example in order to correctly model a deformation bowl a PS close to the center of the bowl must be identified to constrain the deformation model.

Ferretti et al. (2001) shows that the normalized dispersion of the amplitude ( $D_A$ ) is a measure for the stability of the phase ( $\sigma_\nu$ ) of the point scatterer in the resolution cell

$$D_A = \frac{\sigma_A}{\mu_A} \quad (2.12)$$

in which  $\mu_A$  and  $\sigma_A$  are respectively the mean and standard deviation of the amplitude values of the same resolution cell over all the coregistered SLC images.

The PSC are used to form a sparse network of relative phase observations (double-differences or arcs). The double differences are in a temporal (interferometric phase) and spatial (relative phase difference) sense. The relative observations reduce the influence of error sources such as atmospheric signal delay and orbit errors. In the first step the temporal estimation of each PSC is performed, which consists of simultaneously estimating the ambiguities and the parameters of interest. However, there is no direct inversion for solving the ambiguities (Teunissen, 1995). It is only by utilizing the fact that ambiguities are integer numbers a solution can be provided. There are three implemented algorithms to solve this, namely (1) the periodogram technique (Counselman and Gourevitch, 1981; Ferretti et al., 2001), (2) integer bootstrapping (Teunissen, 2001a; Kampes and Hanssen, 2004), and (3) integer least-squares (Teunissen, 1993; Kampes and Hanssen, 2004). Simultaneously the parameters of interest, e.g. residual height and relative deformation rate (assuming a model, e.g. linear) are estimated.

The second step is the spatial estimation, which consists of referencing the temporally estimated PS with respect to a reference PS. The reference PS is assumed stable to improve interpretation (e.g., older buildings, city centers, etc.). Not all ambiguities are correctly estimated, but in this step these errors can be detected and corrected. Minimization of the number of errors is done by removing arcs with very low temporal coherence (large residuals) and leaving only PS without residues with at least three arcs. The remaining PS are assumed to be estimated correctly.

### PS Densification and Final Parameter Estimation

The atmospheric signal is correlated spatially and not temporally, whereas the deformation is assumed correlated both spatially and temporally. The atmospheric signal, orbital errors, and noise are separated from the unmodeled deformation, by identifying the correlations in space and time. To separate the atmospheric phase screen (APS) from the noise and deformation spatial Kriging interpolation is used after subtracting the estimated deformation. This essentially determines the spatially correlated component of the residuals, which is assumed to be the atmospheric signal. The predicted atmospheric phase for every resolution cell is then subtracted from the original interferometric phase and a new network is created. With respect to the network, the second order PSC are unwrapped relative to at least the two closest first order PSC in the network. The check is required to reliably evaluate the ambiguity estimation. Finally the PS are selected on a quality criterion, such as the estimated temporal coherence (Ferretti et al., 2001)

$$\hat{\gamma}_{x,y} = \left| \frac{1}{K} \sum_{k=1}^K \exp(i\varphi_{x,y}^{0k}) \right|, \quad (2.13)$$

where  $K$  is the number of interferograms,  $\underline{e}_{x,y}^{0k}$  the residuals of the original observations and the modeled double difference phase between resolution cells  $x$  and  $y$  in interferogram  $k$  (with respect to a single master), and  $i$  represents the imaginary unit. The temporal coherence is thus based on the noise and model imperfections of the residuals, which if not present, will result in a higher value. The coherence is a value within the range  $[0, 1]$  and a value higher than a certain threshold corresponds to qualitatively good PS.

Another method, suggested by Kampes (2005), is to estimate an a-posteriori variance factor per arc

$$\hat{\sigma}^2 = \frac{\underline{e}^T Q_\varphi^{-1} \underline{e}}{r}, \quad (2.14)$$

in which  $\underline{e}$  is the temporal least-squares residual phase difference vector,  $Q_\varphi$  is the covariance matrix of the phase observations, and  $r = m - q$  the is the redundancy between observations  $m$  and estimated unknown parameters  $q$ . The a-posteriori variance factor is thus based on the residuals, the stochasticity of the residuals, and the redundancy of the system. If a well defined stochastic model is used (e.g., using Variance Components Estimation), then this factor will be a good measure for the quality of the PS. An estimated a-posteriori variance smaller than a certain threshold corresponds to a qualitatively good PS. This does not hold for small stacks ( $K \lesssim 15$ ), because the least-squares residuals will always be small even when the phase is completely decorrelated (Kampes, 2005). A value higher than one suggests that the stochastic model is optimistic, a lower value suggests that the stochastic model is pessimistic.

### 2.2.2 PS Estimation

The PS estimation considers both the estimation of the initial (first order) network, and the final estimation (densification). There is no difference in the estimation method, except that for the input phase of the final estimation the APS is removed. The estimation is based on adjustment and testing theory. Assuming the ambiguities are deterministic after Integer Least-Squares (ILS), the parameters of interest can be calculated with a standard least-squares estimator. The dispersion of the observations follows from their statistical characteristics.

#### Functional Model

The functional model describes the relationship of the phase with respect to the deformation, height with respect to a reference body, master APS, and the ambiguities. The mathematical model is written as a Gauss-Markov model

$$\begin{aligned} E\{\underline{y}\} &= Aa + Bb \\ D\{\underline{y}\} &= Q_y, \end{aligned} \quad (2.15)$$

where  $A$  and  $B$  are the design matrices which describe the functional relationship between the phase and the integer- and real-valued unknown parameter vectors  $a$  and  $b$  respectively. The phase observations are denoted by  $\underline{y}$  with the underline indicating stochastic variables and  $E\{\cdot\}$  is the expectation operator.

Each observation is subject to an ambiguity, because only the fractional phase is measured. These ambiguities make this initially an underdetermined system, i.e., the system of equations

has a rank deficiency. This is solved by adding pseudo observations (denoted with  $\cdot^*$ ) to the system of equations (Kampes and Hanssen, 2004)

$$E\left\{\begin{bmatrix} \underline{\varphi}^{0k} \\ \underline{\Delta H}^* \\ \underline{D}_k^* \\ \underline{S}^* \end{bmatrix}\right\} = \begin{bmatrix} -2\pi I_K \\ 0 \\ 0 \\ 0 \end{bmatrix} a_k + \begin{bmatrix} -\frac{4\pi}{\lambda} \frac{B^{0k}}{R \sin(\theta)} & -\frac{4\pi}{\lambda} & -\frac{4\pi}{\lambda} \\ 1 & 0 & 0 \\ 0 & 1 & 0 \\ 0 & 0 & 1 \end{bmatrix} \begin{bmatrix} \Delta H \\ D_k \\ S \end{bmatrix}. \quad (2.16)$$

Here  $\underline{\varphi}^{0k}$  are the phase double-differences,  $I_K$  denotes the identity matrix of size  $K$ ,  $a^k$  is the integer ambiguity vector,  $\Delta H$  is the height above the reference body,  $D_k$  is the deformation vector, and  $S$  the master atmospheric phase delay. The pseudo-observables are set to a value of zero (if there is no a-priori knowledge of the observables) and initially cause a bias in the solution.

### Integer Least-Squares Estimation

A system of equations, such as (2.15), can be solved using Integer Least-Squares (ILS) Estimation (Teunissen, 2001b) and is for PSI written explicitly as (2.16). The solution of the estimates  $\check{a}$  and  $\check{b}$  is obtained by a three-step procedure:

1. computation of the float solution, neglecting the integer property of the ambiguities, obtaining the estimates  $\hat{a} \in \mathbb{R}$  and  $\hat{b} \in \mathbb{R}$ , with corresponding variance covariance matrix  $Q_{\hat{a}\hat{b}}$ .
2. the real-valued estimates  $\hat{a}$  are mapped to the integer space, with a mapping function  $\mathcal{S}: \check{a} = \mathcal{S}(\hat{a}); (\check{a} \in \mathbb{Z})$
3. updating the float solution of  $\hat{b}$ , once the integer ambiguities are fixed:  $\check{b} = \hat{b} - Q_{\hat{b}\hat{a}} Q_{\hat{a}}^{-1} (\hat{a} - \check{a})$

There are several methodologies to obtain the estimate of the integer ambiguities (Teunissen, 1999). ILS accounts for all the correlation between the float ambiguities, by minimizing equation (2.15). The minimization optimizes the success rate of correctly estimating the ambiguities, i.e.,  $P(\check{a} = a)$ .

### Stochastic Model

Measurement noise is stochastically modeled and is contained in the dispersion  $D\{\cdot\}$  of the observations

$$D\left\{\begin{bmatrix} \underline{\varphi}_k \\ \underline{\Delta H}^* \\ \underline{D}_k^* \\ \underline{S}^* \end{bmatrix}\right\} = \begin{bmatrix} Q_\varphi & & & \\ & \sigma_{\Delta H^*}^2 & & \\ & & Q_{D^*} & \\ & & & \sigma_{S^*}^2 \end{bmatrix}, \quad (2.17)$$

with  $\sigma_{\Delta H^*}^2$  and  $\sigma_{S^*}^2$  the variance of the pseudo-observations, namely the height error and atmospheric signal delay respectively and the variance matrices of the phase observations  $Q_\varphi$  and pseudo deformation parameters  $Q_{D^*}$ .

The variance matrix of the phase observations contains the total variance of the interferometric phase observations  $\sigma_{\psi_p^a}^2$  (noise, atmospheric signal, and and orbital errors), the spatial covariances  $\sigma_{\psi_i \psi_j}$  (atmospheric signal and orbital errors), and the temporal covariances  $\sigma_{\psi^0 \psi^k}$  (temporal

coherence). This variance matrix is constructed by propagating the (co-)variances from SLC phases (Hanssen, 2004) and can be simplified using assumptions on equal temporal coherence, equal atmospheric variance and comparable arc lengths to

$$Q_\varphi = \left( \sigma_{\psi_p^q}^2 - \sigma_{\psi_i \psi_j} - \sigma_{\psi^0 \psi^k} \right) \begin{bmatrix} 4 & 2 & \dots & 2 \\ 2 & 4 & & \vdots \\ \vdots & & \ddots & \\ 2 & \dots & & 4 \end{bmatrix}. \quad (2.18)$$

The variances and covariances of the pseudo-observations are based on a-priori knowledge of the deformation model, atmospheric variability, and the DEM. These are initially for scaling the variances with respect to the estimation parameters.

### 2.2.3 Advantages and Limitations of PSI

PSI overcomes the main limitations of InSAR, i.e., geometrical decorrelation, temporal decorrelation and atmosphere. The temporal decorrelation is resolved by only considering those points where the phase is coherent over long periods of time. It is not strictly necessary that PS are point scatterers, however, point-like PS with a size much smaller than the resolution cell size are not subject to geometrical decorrelation. The coherence for those point-like scatterers is acceptable, even for perpendicular baselines larger than the critical one (Prati and Rocca, 1994). PS with a more distributed nature can still have a dependency on the perpendicular baseline (i.e. the geometry).

The PS technique incorporates stacks of coregistered interferograms in order to search for coherent scatterers. The atmospheric signal is effectively decorrelated in time which makes it possible to filter out this signal using a high-pass filter (Sandwell and Price, 1998; Sandwell and Sichoix, 2000). The disadvantage is that the variance of the spatial and temporal nature of the deformation is lost, in other words the signal is smoothed.

PSI is subject to limitations, mainly due to the rank deficiency in the mathematical model. The wrapped nature of the fractional phase measurements requires the ambiguity to be solved for every observation, together with the parameters of interest. A value for the deformation model (e.g. linear, breakpoint, seasonal model, etc.) is initially assumed as a pseudo-observable, introducing a bias in the float solution. A wrong assumption of the deformation model decreases the number of obtained PS due to the large residuals with respect to the timeseries. However, this does not imply that the scatterer is not a PS, hence increases the false rejections.

## 2.3 Nibbling in PSI

An algorithm is developed to incorporate short-arc PSI as a sequential procedure, which is referred to as Nibbling. Nibbling descends directly from the combination of PSI, region growing, and supervised identification of PS. This approach is expected to obtain results in areas with a high PS density. The dense network and short-arc parameter estimation in a one-dimensional sense are expected to increase the PS density with respect to conventional techniques, without loss of quality. A sequential pixel-by-pixel approach is incorporated in order to determine the parameters of interest for each arc.

This processing is tested on WDS along the coast of the Netherlands. Initial PS results or a-priori knowledge of the scatterer behavior in an area are required, to ensure that the area of interest contains a high density of the PS. For a detailed description of the algorithm and mathematical framework of the parameter estimation, see chapter 3. The case-study and results will be discussed in chapter 4

### 2.3.1 Expected Advantages and Limitations

There are some advantages of the Nibbling approach with respect to conventional PS processing. The short arcs connecting the adjoining resolution cells should imply that there are no ambiguities in the double difference phases. This means that the ambiguities are fixed to zero because the double difference phase stays within the same phase cycle. This removes the rank-deficiency of the system and simplifies the PS-processing to a straight-forward least-squares estimation. Furthermore, a-priori knowledge of the scattering behavior and position of the scatterers is known. Therefore those pixels which are currently not identified as PS actually are expected to be false rejections. Finally the topographic variation along and across the WDS is known.

The sequential pixel-by-pixel approach the processing will be slower, because all the pixels in an area of interest will be estimated. This increases the number of iterations of the approach, and makes it infeasible in larger areas. Furthermore, the approach requires a high PS density such that all PS in the area have an adjoining PS, in order to generate an interpretable result. Line-like (near one-dimensional) areas are expected to be optimal for this approach, where the characteristics of the area minimally change spatially.

The PS on WDS are expected not to be dominant point scatterers, but distributed coherent scatterers. This distributed scattering mechanism is the result of rocks, rubble, and asphalt concrete which are used as reinforcement of the outer wall on WDS. If the size of the coherent scatterer (all of the smaller scatterers together) is in the order of the size of the resolution cell, then this could introduce a dependency on baseline and therefore may be subject to partial geometrical decorrelation. This may be important for the validity of the assumption that no ambiguities occur in phase differences between neighboring pixels.

## Chapter 3

# Nibbling approach

The Nibbling approach is a new method for short-arc processing to identify and estimate PS on line infrastructure. It uses a pixel-by-pixel approach to estimate the parameters of interest and integrate along a WDS (in this case). Because of the narrow areas, for which this approach is designed, and the sequential pixel estimation and integration, the method is considered to be one-dimensional. The method starts at a single pixel (seed pixel) and estimates pixels surrounding this seed pixel, identifying a pixel as a PS based on an acceptance criterion. The approach described here has similarities with region growing algorithms in image segmentation methods, however, it is not an implementation of such an algorithm. In Nibbling the parameters of interest (estimated from the double difference phases) are estimated sequentially, then integrated along the area of interest, and merged with respect to one region. The result is a single region with a single reference point, whereas in image segmentation different regions with specific characteristics are separated.

Existing region growing algorithms in InSAR are developed for unwrapping of interferograms, to increase the confidence of the unwrapping procedure (Lim et al., 1995; Xu and Cumming, 1999). Currently no short-arc approaches are available for PSI. This chapter will discuss the implementation of the Nibbling approach in detail, starting in section 3.1. Thereafter the specific aspects of Nibbling are addressed, which are the correlation between neighboring resolution cells, discussed in section 3.2, and ambiguities related to short arcs, discussed in section 3.3. The functional model and stochastic model are finally discussed in section 3.4.

### 3.1 Implementation and methodology

The Nibbling approach is designed as a short-arc processing technique. The implementation is shown in figure 3.1, where the flow of the approach and the flagging (tracking) of the pixels is shown. In appendix C the construction of algorithm together with the developed pseudo code is given.

The pixels are tracked throughout the process, by flagging them as

1. *seed* pixels of which the parameters of interest are given a reference value of zero,
2. *undetermined* pixels that are not estimated,
3. *expanded* pixels that have at least one neighboring pixel that is undetermined,

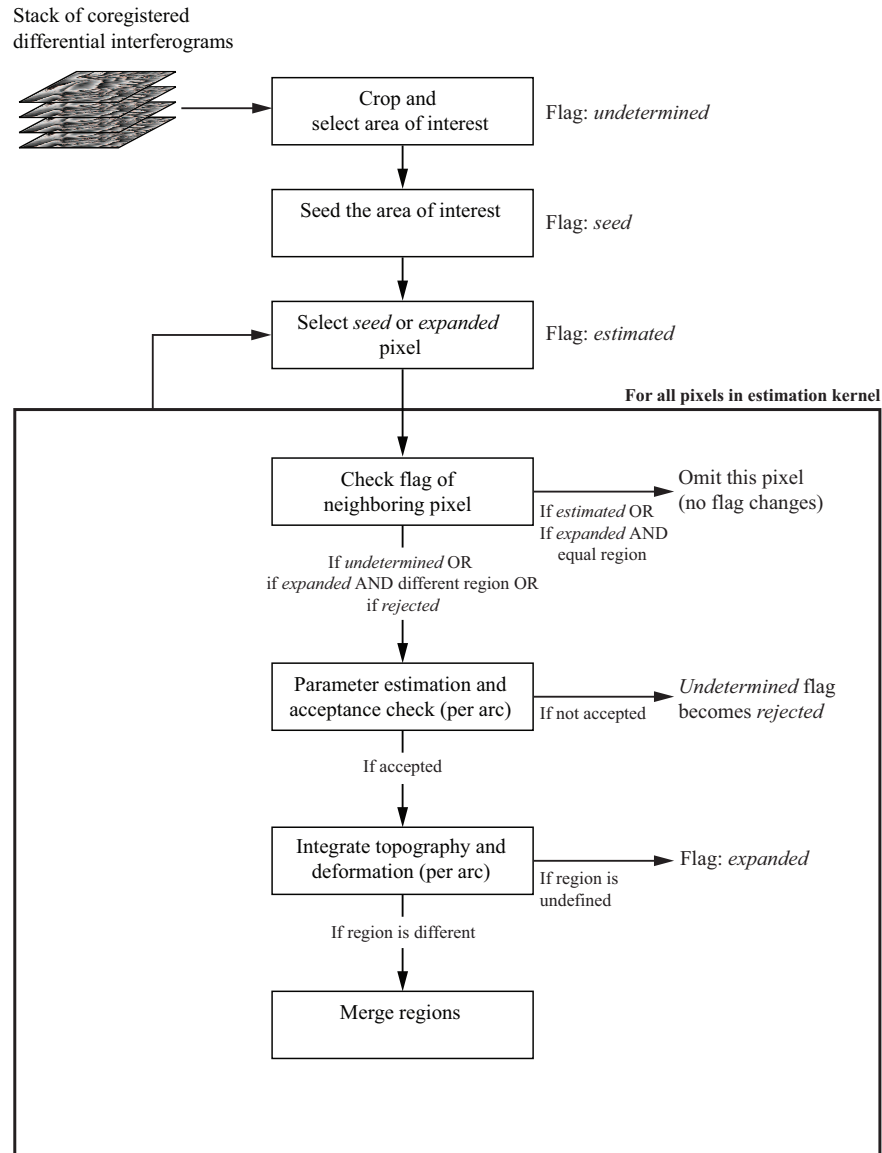


Figure 3.1: The processing and decision chain of the Nibbling approach, including the pixel flags.

4. *estimated* pixels with only expanded pixels as neighbors,
5. *rejected* pixels that are estimated (from an expanded pixel), but not accepted.

Initially, all pixels are undetermined except for the seed pixels. The seed pixels are the same as expanded pixels, only a discrimination is made because these are reference pixels. During the processing a seed or expanded pixel is selected, on which an estimation kernel is centered. The flag of the selected pixel is changed to estimated and all pixels within the estimation kernel are estimated except for estimated pixels and expanded pixels with respect to the same region,



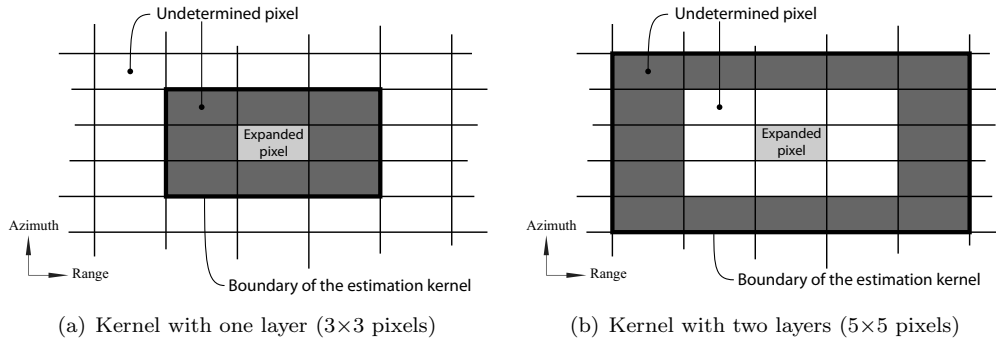


Figure 3.2: Illustration of estimation kernels for Nibbling. The kernel size is defined by the number of layers surrounding the expanded pixel. The darker pixels illustrate those pixels contained in the estimation kernel which will be estimated with respect to the expanded pixel. In (b) a pixel separation of one is included, i.e., the pixels adjoining the expanded pixel are not estimated from the expanded pixel. This may be necessary reduce the correlation between pixels.

because these are assumed to be estimated and spatially integrated correctly. The pixels that are estimated will be flagged as expanded, if the pixel is accepted, or as rejected, if it is not accepted. If an expanded pixel from a different region is estimated and accepted, the regions are merged. If no pixels neighboring a seed pixel are accepted, then the seed pixel is flagged as rejected.

Neighboring pixels are defined as those pixels that are within the estimation kernel, and are not necessarily adjoining. The estimation kernel is a set of neighboring pixels centered on an expanded pixel. Two such kernels are shown in figure 3.2, for a pixel separation zero and one. A kernel is built up in layers, where layer one is the adjoining eight pixels, layer two are the sixteen pixels with a separation of one pixel from the expanded pixel, and so forth. This feature is optional to exclude neighboring pixels or to increase the size of the estimation kernel, because of the correlation.

### 3.1.1 Area of interest

The first step in the Nibbling is the selection of a suitable area. The area of interest is chosen manually using the Multi-image Reflectivity Map (MRM), which is the incoherent pixel average magnitude of a stack of coregistered SLC images. Averaging of a stack of interferograms reduces the speckle significantly and improves the interpretation and identification of objects in the scene. The selection of an area is performed based on the assumption that the density of PS is significant, this requires knowledge of the area. An area containing a high PS density increases the probability that neighboring pixels are coherent such that the algorithm will perform well in the area of interest.

The next step is cropping the data around the area of interest, which in fact is a data reduction method to improve data handling. It is assumed that in the preprocessing no cropping is applied, because the dataset is used for more applications. The (rectangular) crop can contain parts that are not of interest, therefore a mask is applied such that the algorithm will stay within the boundaries of the mask. The area contained in the mask is referred to as the area of interest.

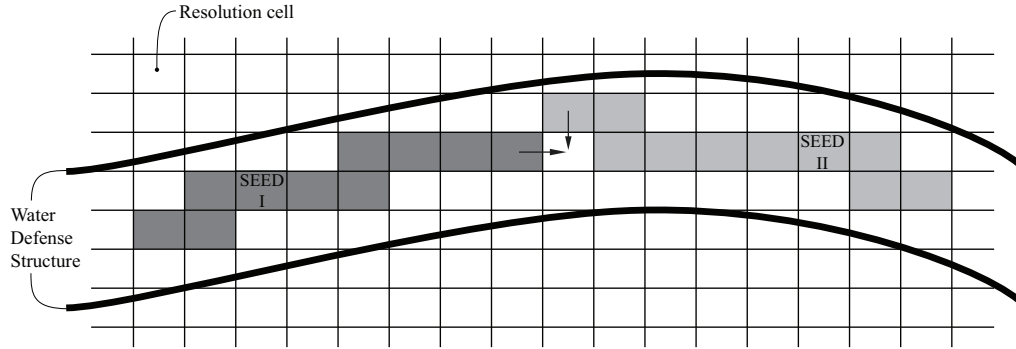


Figure 3.3: Illustration of the Nibbling approach on a WDS. Pixel-by-pixel the regions are expanded until one pixel is estimated with respect to the seed pixels of both regions, indicated by the two arrows in the center. This is further referred to as common pixel  $i$ .

### 3.1.2 Selection of seed pixels

The Nibbling approach initially starts from one or more seed pixels and iteratively estimates its neighboring pixels within the area of interest. If more seed pixels are used, then multiple regions can be grown at the same time. The seed pixels are given a reference value of zero for topography and deformation (parameters of interest). The area of interest is expected to have a high quantity of PS (section 2.2), so that the algorithm is able to expand the regions. The seed pixels are chosen either (1) at random, (2) based on a priori knowledge of the scene, or (3) based on the data (amplitude dispersion).

Random selection of seed pixels is straightforward. The confidence of the seed pixel to actually be a PS varies, however, an incoherent *seed* pixel (e.g., water or vegetated areas) should not be able to expand the region any further because of the noise contained within the seed pixel. This implies that only regions with a PS as a seed pixel are able to expand. If no pixels surrounding a seed pixel are accepted, then the seed pixels are assumed to be incoherent, and it is flagged rejected. An accepted estimated neighboring pixel is added to the region of the seed pixel, based on the acceptance criterion (see section 3.1.4).

Seed pixels chosen based on a priori knowledge, can improve the confidence of the seed pixels. This a priori knowledge is the (limited) knowledge about the position of the PS within the area of interest, based on conventional processing. If the algorithm is to be developed as a stand alone system, this knowledge may not be available, and therefore it is not considered here.

Seed pixels can be chosen based on the data itself, by determining criteria such as the normalized amplitude dispersion. This is the method that is incorporated in conventional PSI, in order to select the PSC for the initial network. This is a feasible approach to consider in the Nibbling algorithm, however, if the assumption is correct that the density of PS in the area of interest is high, then many pixels will have a low amplitude dispersion. A lower threshold can compensate for this.

Considering the three aforementioned methods, random seeding is chosen. This method is com-

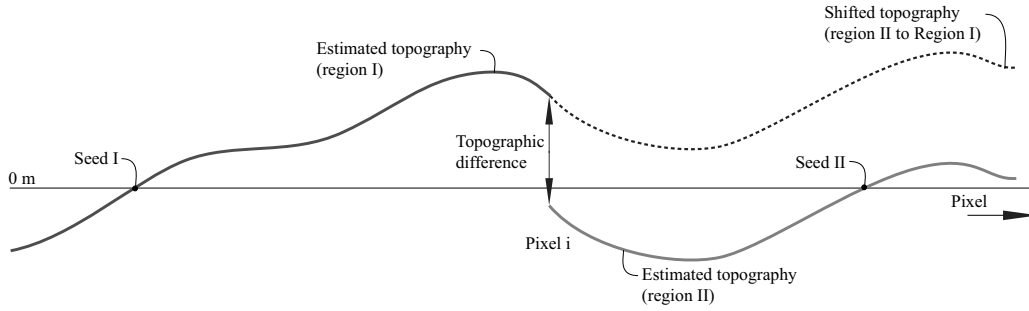


Figure 3.4: Illustration to adjust the topography of region II with respect to region I. The indicated topographic difference is added to every pixel contained by region II.

putationally efficient, it is easy to incorporate, and the density of PS is assumed to be very high within the area of interest.

### 3.1.3 Expanding and merging of regions

Every iteration in the Nibbling algorithm will expand a region from an expanded pixel, until the parameters of all neighboring pixels within the estimation kernel are estimated. The expanded pixel from which the region is grown, then becomes an estimated pixel. The estimation procedure (of topography and deformation) is performed, based on the flags of the neighboring pixels, i.e., if a pixel in the kernel is flagged as expanded, it will be omitted if the region number is the same. The newly expanded pixels in the estimation kernel can either be accepted or not and are flagged expanded or rejected, respectively.

Regions are expected to expand until two different regions are adjoining, meaning that an expanded pixel of a different region is identified within the estimation kernel. Figure 3.3 illustrates two regions that are adjoining, of which one pixel (indicated with the arrows) will be estimated from both regions. It is necessary to connect the regions and reference all the pixels to a single seed pixel, to get an interpretable result. The integrated topography and deformation from both regions will not be the same, because of the different reference pixels. The difference in topography and deformation (time series) for the common pixel is used to shift one of the regions with respect to the other. This procedure is referred to as merging.

#### Topography

Merging of the topography is the straightforward addition of the topographic difference of a pixel that is estimated (accepted) with respect to the seed pixels of two regions. An estimation referenced to the seed pixel of region  $w$  becomes referenced to the seed pixel in region  $v$  by

$$H_v^x = H_w^x + \Delta H_{vw}^i, \quad (3.1)$$

with  $H_v^x$  and  $H_w^x$  containing the topography of a pixel  $x$  referenced to seed pixels of regions  $v$  and  $w$  respectively, and  $\Delta H_{vw}^i$  the difference of the estimated topography of pixel  $i$  between

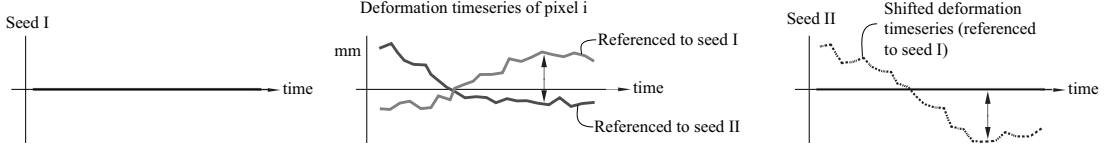


Figure 3.5: Illustration to adjust the deformation time series of region II with respect to region I. Left and right are the seed pixels of both regions with a deformation set to zero. The difference in deformation at common pixel  $i$  (center) is determined for each epoch and is added to that epoch for each pixel contained in region II.

the estimations referenced to regions  $v$  and  $w$ , see figure 3.4. The pixel at location  $x$ , which is initially referenced to region  $w$ , is now referenced to region  $v$ .

### Deformation

Deformation relative to different regions is merged similarly as the topography, only now each parameters contain the deformation timeseries  $D$ ; a vector of  $K$  (the number of interferograms) deformation parameters with respect to the master SLC and referenced to a seed pixel. In order to merge the deformation of a pixel at location  $x$  referenced to region  $w$ , to a region  $v$ , the difference vector of the deformation timeseries between these regions at the commonly estimated (accepted) pixel  $i$  (with respect to two regions) is added to the deformation vector in region  $w$  of a pixel  $x$ , or

$$D_v^x = D_w^x + \Delta D_{vw}^i, \quad (3.2)$$

with  $D_v^x$  and  $D_w^x$  the deformation timeseries of a pixel  $x$  referenced to the seed pixel in region  $v$  and  $w$  respectively, and  $\Delta D_{vw}^i$  is the difference in deformation at common pixel  $i$  between regions referenced to pixels  $w$  and  $v$ , see figure 3.5.

#### 3.1.4 Acceptance criteria

The Nibbling algorithm requires a criterion to accept a pixel, based on the characteristics of the residuals after the parameter estimation step. For this either the temporal coherence, see equation (2.13), or the a posteriori variance factor can be used, see equation (2.14).

The advantage of using the a posteriori variance factor is that the stochasticity of the system is taken into account. However, in Nibbling the variances are not estimated with Variance Components Estimation (VCE), because no PS candidates are selected on which this estimate can be based. The seed pixels are randomly selected, therefore it is uncertain if the selected pixel is actually a PS and the stochastic model may be erroneous. Consequently the assumptions for the variances may be too optimistic/pessimistic and that results in a too optimistic/pessimistic covariance matrix. This will change the range of values of the a posteriori variance factor, and therefore also the number of PS that are accepted.

Alternatively the estimated temporal coherence can be determined as a criterion for accepting the pixel as a PS. This is only based on the residual phases and physical characteristics of the

signal and does not take into account the redundancy or the covariances. In case of stochastically modeled deformation (see section 3.4) this method may underestimate the actual temporal coherence, because the deformation signal is still contained in the residuals. However, if the deformation difference is small, as is expected with neighboring pixels, then this measure may still be valid.

The a posteriori variance factor should be chosen as a more suitable quality measure if the deformation is stochastically modeled, because the residuals still contain the signal of the deformation. If the deformation is functionally modeled, then the temporal coherence will be a better measure. In the case of Nibbling the stochastic model is not defined well enough, because no VCE is performed, therefore the temporal coherence will be used in either case. This is a valid approach in case of neighboring pixels, because the difference in deformation between these pixels will be very small, hence the difference in temporal coherence with or without stochastic modeling of the deformation will be approximately equivalent.

The accepting of a pixel as a PS depends on the threshold for the temporal or a posteriori coherence. Initially the threshold of the acceptance criterion is set high, so that only those very coherent pixels are estimated. Once the regions stops expanding, because no undetermined pixels are left, the algorithm relaxes the acceptance criteria and estimates all unestimated and rejected pixels again. The acceptance criterion is gradually lowered to a minimum, which creates routes through the area where the confidence in correctly estimating the topography and deformation is high (high temporal coherence).

## 3.2 Spatial correlation of neighboring pixels

Adjacent pixels in an SLC image are correlated due to the fact that the resolution cells overlap, see figure 2.2 in section 2.1.2. In conventional PSI, only the correlation between two resolution cells due to point scatterers are taken into account, because of the sidelobes. With adjoining or neighboring pixel processing the correlation between resolution cells containing distributed scatterers must also be analyzed. If this correlation is significant, it must be taken into account in the processing.

The oversampling factor (OSF), indicating the fraction that the resolution cells overlap, can be computed for range and azimuth by

$$\begin{aligned} \text{OSF}_r &= \frac{f_s}{B_r} \\ \text{OSF}_a &= \frac{f_{pr}}{B_a} \end{aligned} \tag{3.3}$$

with  $f_s$  the sampling frequency,  $f_{pr}$  the pulse repetition frequency,  $B_r$  the range (or chirp) bandwidth, and  $B_a$  the processed azimuth (Doppler) bandwidth. However, this value is not linearly related to the percentage of correlation of the overlapping resolution cells, because the spectrum is weighted.

The frequency spectrum of the chirp, can be approximated by a boxcar function ( $\Pi(\cdot)$ ). Such a spectrum is spatially characterized by a normalized sinc function ( $\text{sinc} = \sin(\pi x)/(\pi x)$ ) (Woodward, 1953)). The autocorrelation length of the chirp is very short (narrow main lobe of the

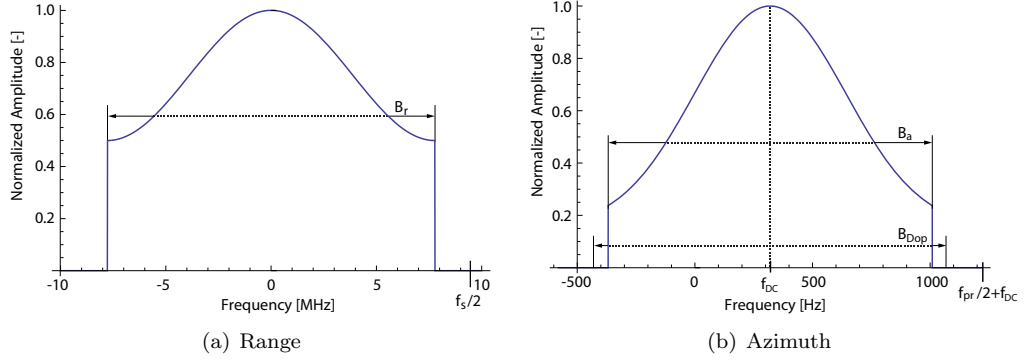


Figure 3.6: The hamming windows in range and azimuth, for ERS-1. The hamming window in azimuth is centered around the Doppler centroid frequency.

sinc pattern), which results in a high resolution (Swart, 2000). The disadvantage, however, is that the autocorrelation contains sidelobes, and causes objects to appear as ghost images. The frequency spectrum is therefore weighted with a hamming window to reduce this effect, while retaining a high resolution. The frequency spectrum is thus shaped like the weighting function (the hamming window).

Suppose that there are two resolution cells in an SLC image with a fixed size, that are separated by a variable distance  $d$  (posting). Each resolution cell backscatters a return signal, which is measured by the SAR instrument. If the posting is zero, then the resolution cells will cover the same area, and consequently the correlation will be one. If the posting is not zero, the correlation between these two resolution cells can be described by the convolution of these return signals, assuming distributed scatterers. If the shape of the frequency spectrum is assumed to be the same as the weighting function, then the (normalized) Inverse Fourier Transform (IFT) of the squared weighting function will describe the correlation ( $r(d)$ ) of the two signals as a function of posting

$$r(d) = \mathcal{F}^{-1} [W^2(f)] (d). \quad (3.4)$$

The range spectrum is weighted with a Hamming window over  $|f_r| \leq f_s/2$ , which leads to the weighting function

$$W(f_r) = \left( \alpha + (1 - \alpha) \cos \left( \frac{2\pi f_r}{B_r} \right) \right) \Pi \left( \frac{f_r}{B_r} \right), \quad (3.5)$$

where  $\alpha$  is the hamming window constant (0.75 for ERS and Envisat), and is a function of the range frequency  $f_r$ , see figure 3.6(a) (Geudtner, 1995). The range frequency is proportional to the posting in range of two adjoining resolution cells.

In azimuth the spectrum is weighted with a Hamming window  $\times$  sinc<sup>2</sup>-function, related to the the antenna pattern, over  $|f_a| \leq f_{pr}/2$  (Geudtner, 1995). The weighting function in azimuth is

$$W(f_a) = \left( \alpha + (1 - \alpha) \cos \left( \frac{2\pi (f_a - f_{DC})}{B_a} \right) \right) \text{sinc}^2 \left( \frac{f_a - f_{DC}}{B_{Dop}} \right) \Pi \left( \frac{f_a - f_{DC}}{B_a} \right), \quad (3.6)$$

which is a function of the azimuth frequency,  $f_a$ , and therefore proportional to the azimuth posting. Here  $f_{DC}$  is the Doppler centroid frequency and  $B_{\text{Dop}}$  is the Doppler bandwidth. The hamming window in azimuth is illustrated in 3.6(b)

### 3.2.1 Correlation in range

For the correlation in range, the spectrum is squared prior to computing the IFT, because a convolution in the space domain is equivalent to the multiplication in the frequency domain. The squared spectrum becomes

$$\begin{aligned} W^2(f_r) &= \left[ \left( \alpha + (1 - \alpha) \cos \left( \frac{2\pi f_r}{B_r} \right) \right) \Pi \left( \frac{f_r}{B_r} \right) \right]^2 \\ &= \sum_{i=0}^2 K_i \cos \left( \frac{2\pi i f_r}{B_r} \right) \Pi \left( \frac{f_r}{B_r} \right) \end{aligned} \quad (3.7)$$

with

$$K_i = \begin{cases} \alpha^2 + \frac{1}{2}(1 - \alpha)^2 & \text{if } i = 0 \\ 2\alpha(1 - \alpha) & \text{if } i = 1 \\ \frac{1}{2}(1 - \alpha)^2 & \text{if } i = 2. \end{cases} \quad (3.8)$$

To make the correlation function independent of any platform, therefore relating the correlation with respect to the sampling distance (slant range resolution), these equations are reformulated. This is a coordinate transformation in order to make the equations dimensionless. The new variables are dimensionless range frequency  $\tilde{f}_r$  and dimensionless range time  $\tilde{t}_r$ . The dimensionless frequency is a variable in the frequency domain, whereas dimensionless time is a variable in the spatial domain. The dimensionless time is related to the posting, which is considered a variable here. The new variables are related to frequency and time as

$$\tilde{f}_r = \frac{f_r}{B_r} \quad (3.9)$$

$$\tilde{t}_r = B_r t_r = B_r \frac{2d_{sr}}{c} = \frac{d_{sr}}{\Delta r} = \frac{1}{OSF_r}, \quad (3.10)$$

with range time proportional to the variable slant range posting

$$t_r = \frac{2d_{sr}}{c}, \quad (3.11)$$

and (constant) range resolution

$$\Delta r = \frac{c}{2B_r}. \quad (3.12)$$

Here  $c$  is lightspeed, and  $d_{sr}$  is the slant range posting (considered variable). The dimensionless range time is actually posting per resolution of the system and is inversely related to the over-sampling factor in range. The posting per resolution cell is referred to as sampling distance. A sampling distance of one relates to the pixels being adjoining. Substituting equation (3.10) into equation (3.7), results in

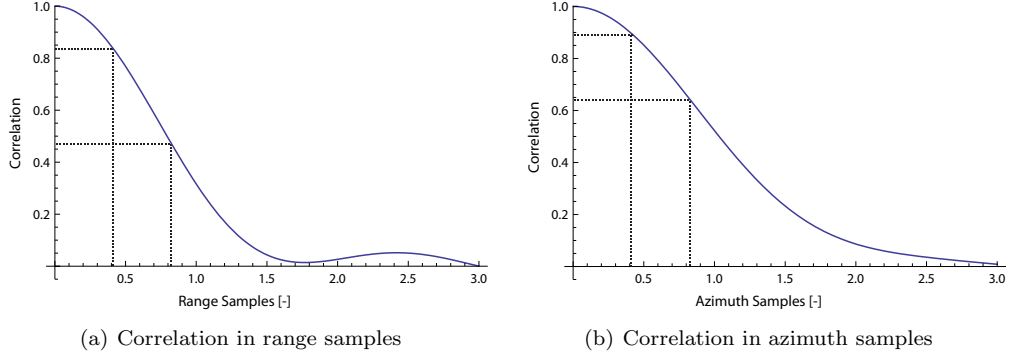


Figure 3.7: The correlation as function of samples (1/OSF). The dashed lines indicate the correlation for ERS with  $1/\text{OSF} = 0.82$  for both range and azimuth, and oversampled by a factor of 2 ( $1/(2 \cdot \text{OSF}) = 0.41$ ). Oversampling reduces the posting and consequently increases the correlation.

$$W^2(f_r) = \sum_{i=0}^2 K_i \cos(2\pi i \tilde{f}_r) \Pi(\tilde{f}_r). \quad (3.13)$$

Now the continuous IFT of the two terms are computed separately, knowing that the IFT of the sum of cosine terms is a summation of Dirac Delta functions  $\delta(\cdot)$ , and that the IFT of the rectangular function is the normalized sinc function. Both solutions are then easily convolved, resulting in

$$\begin{aligned} w(\tilde{t}_r) &= \sum_{i=-2}^2 C_i \delta(\tilde{t}_r - i) \otimes \text{sinc}(\tilde{t}_r) \\ &= \sum_{i=-2}^2 C_i \text{sinc}(\tilde{t}_r - i), \end{aligned} \quad (3.14)$$

with

$$C_i = \begin{cases} K_0 & \text{if } i = 0 \\ \frac{1}{2}K_{|i|} & \text{if } i \neq 0 \end{cases} \quad (3.15)$$

and normalized using  $w(0) = C_0$  to

$$r(\tilde{t}_r) = \sum_{i=-2}^2 \frac{C_i}{C_0} \text{sinc}(\tilde{t}_r - i), \quad (3.16)$$

in which  $r(\tilde{t}_r)$  represents the correlation in range as a function of the inverse oversampling factor in range. The resulting figure is independent of any platform, because it is no longer related to the frequencies directly. For a given oversampling factor, the correlation can be determined, which is shown in figure 3.7(a).



### 3.2.2 Correlation in azimuth

The shape of the spectrum in azimuth is equivalent to that of range multiplied by a sinc-squared term due to the antenna pattern. The sinc-squared term is therefore related to the Doppler bandwidth, and not to the processed Doppler bandwidth. Furthermore, the spectrum is shifted around the Doppler centroid frequency. The squared amplitude response in azimuth is simplified to

$$\begin{aligned} W^2(f_a) &= \left[ \left( \alpha + (1 - \alpha) \cos \left( \frac{2\pi(f_a - f_{DC})}{B_a} \right) \right) \text{sinc}^2 \left( \frac{f_a - f_{DC}}{B_{Dop}} \right) \Pi \left( \frac{f_a - f_{DC}}{B_a} \right) \right]^2 \\ &= \sum_{i=0}^2 K_i \cos \left( \frac{2\pi i(f_a - f_{DC})}{B_a} \right) \text{sinc}^4 \left( \frac{f_a - f_{DC}}{B_{Dop}} \right) \Pi \left( \frac{f_a - f_{DC}}{B_a} \right), \end{aligned} \quad (3.17)$$

where  $K_i$  was defined in equation (3.8). To make the correlation function in azimuth independent of any platform, two new variables are introduced consequently relating the correlation with respect to the sampling distance (azimuth posting). Similarly as in range, a coordinate transformation is performed in order to make the equations dimensionless. The new variables are dimensionless azimuth frequency  $\tilde{f}_a$  and dimensionless azimuth time  $\tilde{t}_a$ . The dimensionless frequency is a variable in the frequency domain, whereas dimensionless time is a variable in the spatial domain. The dimensionless time is related to the posting, which is considered a variable here. The new variables are related to azimuth frequency and azimuth time as

$$\tilde{f}_a = \frac{f_a - f_{DC}}{B_a} \quad (3.18)$$

$$\tilde{t}_a = B_a t_a = B_a \frac{d_a}{v_{s/c}} = \frac{d_a}{\Delta a} = \frac{1}{\text{OSF}_a}, \quad (3.19)$$

with azimuth time proportional to the (variable) azimuth posting  $d_a$

$$t_a = \frac{d_a}{v_{s/c}}, \quad (3.20)$$

and (constant) azimuth resolution

$$\Delta a = \frac{v_{s/c}}{B_a}. \quad (3.21)$$

Here  $v_{s/c}$  is the satellite velocity relative to the earth surface. The dimensionless time is actually posting per resolution of the system and is inversely related to the oversampling factor in azimuth. Substituting this into equation (3.17) results in

$$W^2(f_a) = \sum_{i=0}^2 K_i \cos(2\pi i \tilde{f}_a) \text{sinc}^4 \left( \frac{B_a}{B_{Dop}} \tilde{f}_a \right) \Pi(\tilde{f}_a). \quad (3.22)$$

The squared amplitude response is now similar to that of range, with the extension of a  $\text{sinc}^4$  term. Within the  $\text{sinc}^4$  term, there is a constant factor which represents the ratio between the Doppler bandwidth (related to the antenna pattern) and the processed Doppler bandwidth. To simplify, the Doppler bandwidth ratio is written as

$$R_{Dop} = \frac{B_a}{B_{Dop}}. \quad (3.23)$$

The correlation in azimuth can be computed by using the solution in range, convolved with the continuous IFT of the  $\text{sinc}^4$  term, which is a piecewise polynomial.

$$\begin{aligned}
 g(\tilde{f}_a) &= \text{sinc}^4(\tilde{f}_a R_{\text{Dop}}) \\
 P(\tilde{t}) &= \mathcal{F}^{-1}[g(\tilde{f}_a)](\tilde{t}_a)
 \end{aligned}$$

$$P(\tilde{t}_a) = \begin{cases} P_1(\tilde{t}_a) = \frac{1}{6R_{\text{Dop}}^4} (2R_{\text{Dop}} + \tilde{t}_a)^3 & \text{for } -2R_{\text{Dop}} < \tilde{t}_a \leq -R_{\text{Dop}} \\
 P_2(\tilde{t}_a) = \frac{1}{6R_{\text{Dop}}^4} (4R_{\text{Dop}}^3 - 6R_{\text{Dop}}\tilde{t}_a^2 - 3\tilde{t}_a^3) & \text{for } -R_{\text{Dop}} < \tilde{t}_a \leq 0 \\
 P_3(\tilde{t}_a) = P_2(-\tilde{t}_a) & \text{for } 0 < \tilde{t}_a \leq R_{\text{Dop}} \\
 P_4(\tilde{t}_a) = P_1(-\tilde{t}_a) & \text{for } R_{\text{Dop}} < \tilde{t}_a \leq 2R_{\text{Dop}} \\
 0 & \text{otherwise.} \end{cases} \quad (3.24)$$

Convolving this with the IFT of the other terms, similarly obtained as in range, gives

$$\begin{aligned}
 w(\tilde{t}_a) &= \sum_{i=-2}^2 C_i \text{sinc}(\tilde{t}_a - i) * P(\tilde{t}_a) \\
 &= \int_{\mathbb{R}} \sum_{i=-2}^2 C_i \text{sinc}((\tilde{t}_a - \tau) - i) P(\tau) d\tau \\
 &= \sum_{i=-2}^2 C_i \sum_{j=1}^4 \int_{R_{\text{Dop}}(-3+j)}^{R_{\text{Dop}}(-2+j)} \text{sinc}((\tilde{t}_a - \tau) - i) P_j(\tau) d\tau. \quad (3.25)
 \end{aligned}$$

In this form, a mathematical software package (e.g., Mathematica) is able to normalize this and give an analytical solution for the correlation function, shown in figure 3.7(b). Because the solution is complex an approximation of the correlation function  $r(\tilde{t})$  is constructed by fitting a LS polynomial, which minimizes the  $L^2$ -norm. The  $L^2$ -norm (Gradshteyn et al., 1994) is defined for a continuous function  $g(x)$  as

$$\|g(x)\|_2 = \left( \int |g(x)|^2 dx \right)^{\frac{1}{2}}. \quad (3.26)$$

The best fitting polynomial in this case uses the symmetry of the solution, and therefore only contains the even coefficients. This assumption can be made, because the correlation function ( $r(\tilde{t}_a)$ ) is the convolution of two identical symmetric functions and therefore will also be symmetric. Furthermore, the domain of the approximation is limited to  $\tilde{t}_a \in [0, 3]$  samples. The approximate correlation function for azimuth, assuming  $R_{\text{Dop}} = 0.915$  (ERS and Envisat), becomes

$$r(\tilde{t}) \approx \begin{bmatrix} 1 & \tilde{t}^2 & \tilde{t}^4 & \tilde{t}^6 & \tilde{t}^8 & \tilde{t}^{10} \end{bmatrix} \begin{bmatrix} 1 \\ 6.8198 \cdot 10^{-1} \\ 2.0713 \cdot 10^{-1} \\ -3.2819 \cdot 10^{-2} \\ 2.6417 \cdot 10^{-3} \\ -8.5422 \cdot 10^{-5} \end{bmatrix}. \quad (3.27)$$

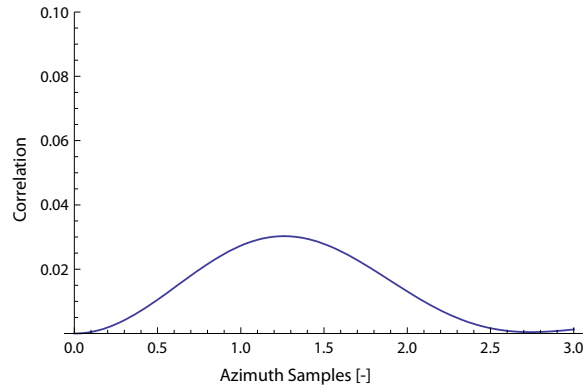


Figure 3.8: The difference between azimuth correlation with  $R_{\text{Dop}} = 1$  and  $R_{\text{Dop}} = 1377/1505$  (ERS). The difference in correlation does not exceed 0.04, thus this is an adequate approximation of the theoretical correlation within the domain  $\tilde{t}_a \in r(0, 3)$ .

Here a total of five coefficients (tenth order) are necessary in order to approximate the correlation function accurately. When fewer coefficients are used, then the shape of the correlation function is not well described when the posting approaches three samples. With the given amount of coefficients a maximum accuracy of the approximation of  $5 \cdot 10^{-3}$  is achieved (also known as the  $L^\infty$ -norm).

There is one dependent term that is platform and processing dependent, which is referred to here as the Doppler bandwidth ratio  $R_{\text{Dop}}$ . If this ratio is assumed to be one, which is not true in reality, the correlation will increase. In systems such as ERS and Envisat,  $R_{\text{Dop}} \leq 1$ , which means that the processed Doppler bandwidth is smaller than the Doppler bandwidth. For ERS the Doppler bandwidth ratio is approximately 0.915. If the actual Doppler Bandwidth is assumed to be equal to the processed bandwidth, i.e.,  $R_{\text{Dop}} = 1$ , the correlation function simplifies. However, this produces a maximum absolute error in the theoretical correlation of approximately  $4 \cdot 10^{-2}$ , making this an adequate approximation of the correlation in azimuth. If this assumption is made, then the correlation function again becomes platform independent, assuming this ratio is relatively high for any platform. The difference between the theoretical correlation between resolution cells for  $R_{\text{Dop}} = 1$  and  $R_{\text{Dop}} = 0.915$  (ERS and Envisat) is shown in figure 3.8.

### 3.2.3 Differences in range and azimuth correlation

Figure 3.7 shows both the azimuth and range correlation with respect to the sampling distance. There is a distinct difference in the correlation in both directions as a function of the inverse OSF. The correlation in range, for a sampling distance smaller than one, shows a lower correlation with respect to azimuth. The frequencies of specific platforms (e.g., Envisat or ERS) are irrelevant, because all of the equations are derived as function of the inverse OSF (i.e., dimensionless). For ERS and Envisat the oversampling factor in range and azimuth is the same, which implies that the overlapping surface area is equal. Therefore the only difference that remains is in the weighting functions. The difference between the weighting functions of azimuth and range, respectively equations (3.5) and (3.6), is the added sinc-squared term to the azimuth weighting function due to the antenna pattern. This extra term removes the sidelobes, as can be seen in

the correlation in range, but increases the width of the main lobe, which effectively increases the correlation in azimuth for equivalent OSF.

The correlation is significant between two pixels, and should be taken into account in the processing. The correlation in azimuth is higher for a given posting than in range, which is due to the additional sinc term related to the antenna pattern. An interesting observation, however, is that the correlation in range and azimuth are not zero when the pixels are adjoining ( $1/\text{OSF} = 1$ ). This means that the correlation between the two pixels is not only due to the overlap of the resolution cells. If the spectrum would not be weighted, then the autocorrelation of the spectrum (assumed a rectangular function) will be a normalized sinc function, which crosses zero correlation at a posting equal to an integer number of samples. By weighting the spectrum, the autocorrelation length is increased and consequently increases the correlation between adjoining resolution cells. The correlation is therefore dependent on the weighting of the spectrum, which is used to reduce sidelobes. In azimuth, the antenna pattern also increases the correlation, next to the hamming window.

### 3.3 Ambiguities for neighboring resolution cells

An ambiguity is a phase difference larger than  $\pi$ , which is indistinguishable from phase differences shifted by  $2\pi a$  (with  $a \in \mathbb{Z}$ ), because of the limited range of the phase. Although we assume that there are no ambiguities in the phase difference between neighboring pixels, it should be investigated if this is completely valid. In conventional processing ILS provides the ambiguity resolution for a stack of interferograms. This is essential, because the arcs span larger distances such that the atmospheric signal, orbital errors, topography, and deformation start to play a significant role in the double difference phase observations. In Nibbling, the arcs span only small distances, hence it is assumed that these contributions are small. The phase differences are therefore dominantly related to the topography and the range subpixel position (for point scatterers), and consequently related to the perpendicular baseline of the interferograms.

#### 3.3.1 Baseline dependent causes for ambiguities

When the spatial separation between resolution cells is extremely small, e.g., no more than 40 meter apart, then the influences of atmosphere, orbital errors, and deformation, is small. These sources are spatially correlated, and cancel out in the double differences mostly. The effect of topography and (in case of point scatterers) range subpixel position, are not necessarily small. The topography is spatially correlated extent, but can still be in the order of 5 meters for adjoining pixels in the Netherlands. The range subpixel position is not spatially correlated and is, similarly to the topography, dependent on the perpendicular baseline.

Ambiguities can occur at larger baselines, because the topography and range subpixel position are expected to contribute most the phase for neighboring pixels. The topographic error is indistinguishable from the range subpixel position, because the phase component due to both these sources are superimposed onto each other. The combined topography and range sub-pixel position may cause the double difference phase observations to become ambiguous. The smallest perpendicular baseline at which an ambiguity can occur is estimated with the functional relationships between topography, range subpixel position, and perpendicular baseline.

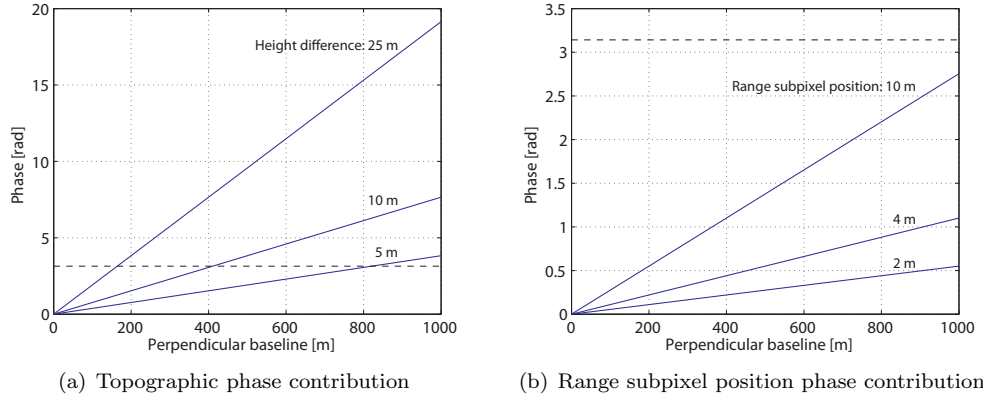


Figure 3.9: The phase contributions as a function of perpendicular baseline, because of topographic errors and range subpixel position of the target. The maximum ground range subpixel position is 10 m, because data oversampled by a factor of two is assumed. The dashed line indicates the phase at which ambiguities occur in the double difference phases.

### Topography

The topographic height that relates to one fringe (a  $2\pi$  phase cycle), is directly computed from equation (2.2). The relative topographic difference at which an ambiguity occurs is calculated by fixing the phase to  $2\pi$  and varying the perpendicular baseline. The height difference with corresponding to a  $2\pi$  phase shift is

$$H_{2\pi} = -\frac{\lambda}{2} \frac{R \sin \theta}{B_{\perp}}. \quad (3.28)$$

For Envisat, this effect produces one fringe in the interferogram for a perpendicular baseline of 800 m, if the topographic differences between two resolution cells is approximately 10 m.

The relation of the phase with respect to the perpendicular baseline for specific topographic differences is shown in figure 3.9(a). This figure uses equation (2.2) to relate the phase and the perpendicular baseline, for specific height differences. The relation is linear and can therefore be easily modeled to adapt the ambiguities. A phase can become wrapped

### Range subpixel position

The range subpixel position is the position of the actual phase center with respect to the leading edge of the resolution cell, for which the reference phase is computed (Kampes, 2005; Marinkovic et al., 2008). The topographic component related to this effect only occurs when dominant point scatterers are present within the resolution cell. Initially it was not expected that there were dominant targets in the area of interest (see chapter 4), however, this should not be neglected.

The sensitivity of the interferometric phase to a subpixel position is dependent on the perpendicular baseline. Figure 3.10 illustrates the geometry of a subpixel position in range. The range subpixel position cannot be distinguished from the topographic error, which may result in a geolocalization error. Such a geolocalization error can be in the order of 10 m, for Envisat (Ketelaar, 2008). In cross-interferometry (interferometric combinations between two different sensors), where different frequencies are used, the range subpixel position can and should be accounted

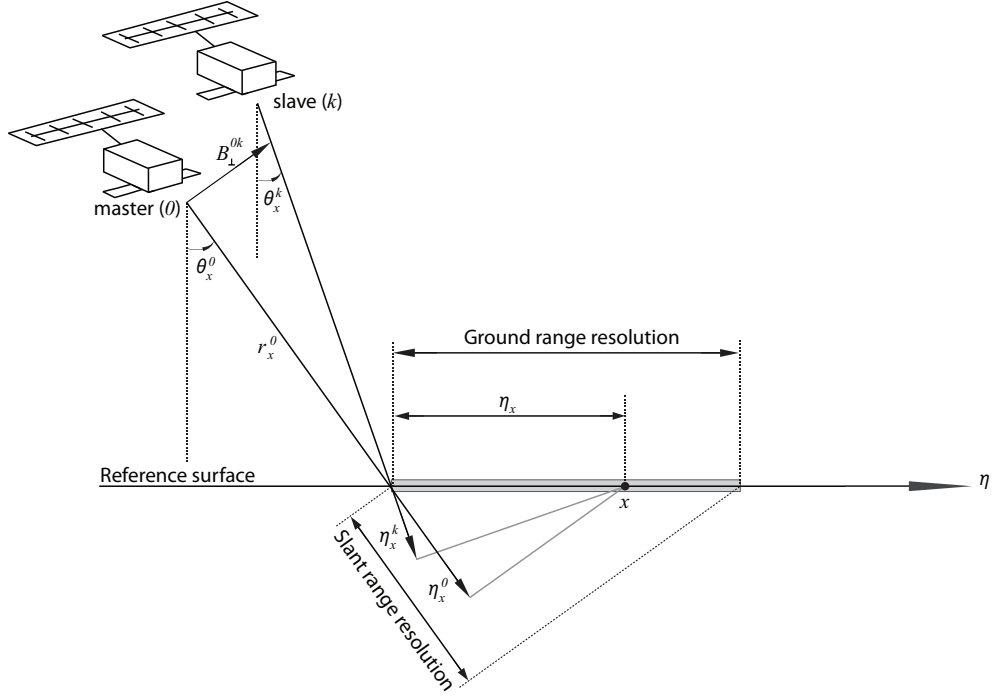


Figure 3.10: Illustration of the geometry including a subpixel position in range of  $\eta_x$ . Adapted from Kampes (2005) and Marinkovic et al. (2008)

for separately from the topographic error (Adam et al., 2004; Kampes, 2005). Although here the influence of range subpixel position cannot be accounted for separately, there can still be a phase component induced by this phenomenon. Consequently this could lead to a smaller perpendicular baseline at which an ambiguity can occur.

The additional range (and phase component) to the actual phase center induced by a subpixel position (in range) with respect to its leading edge can be derived from the geometry shown in figure 3.10 (Kampes, 2005; Marinkovic et al., 2008). The ground range distance from the leading edge for epoch  $k$  is referred to as the range subpixel position ( $\eta_x^k$ ) and its equivalent phase are

$$\begin{aligned}\eta_x^k &= \eta_x \sin \theta_x^k \\ \varphi_{\eta_x}^k &= \frac{-4\pi}{\lambda} \eta_x \sin \theta_x^k.\end{aligned}\tag{3.29}$$

Assuming the same frequencies for both master and slave acquisitions, the interferometric phase for a point target at a range subpixel position  $\eta_x$  can be written as

$$\varphi_{\eta_x}^{0k} = \frac{-4\pi}{\lambda} \eta_x (\sin \theta_x^0 - \sin \theta_x^k).\tag{3.30}$$

Finally substitution of the approximation  $\theta_x^0 - \theta_x^k \approx B_{\perp} / r_x^0$  in equation (3.30) results in

$$\varphi_{\eta_x}^{0k} = \frac{-4\pi}{\lambda} \eta_x \left( \sin \theta_x^0 - \sin \left( \theta_x^0 + \frac{B_{\perp}}{r_x^0} \right) \right).\tag{3.31}$$

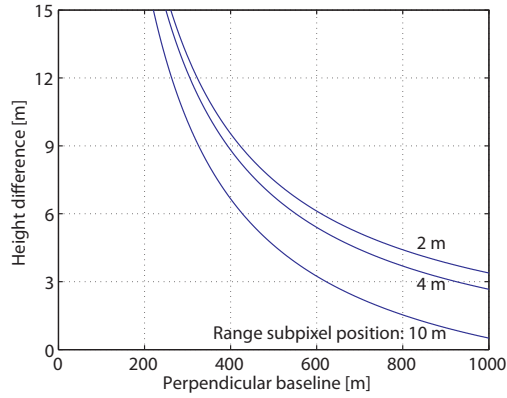


Figure 3.11: The perpendicular baseline at which an ambiguity occurs due to the combined influence of the height difference and the range subpixel position. Here it is shown that the double difference phase of a point scatterer at a range subpixel position of 4 meter, with height difference between the resolution cells of only 4 meter can be ambiguous at perpendicular baselines of over 800 meter.

Esfahany (2008) applied trigonometric relations (sine of the sum of two angles) and the assumption that the perpendicular baseline is much smaller than the range ( $B_{\perp}^{0k} \ll r_x^0$ ), to simplify equation (3.31) to

$$\varphi_{\eta_x}^{0k} = \frac{4\pi}{\lambda} \frac{B_{\perp}}{r_x^0} \eta_x \cos \theta_x^0. \quad (3.32)$$

Figure 3.9(b) shows that the phase again linearly increases with respect to the perpendicular baseline. A maximum range subpixel position is shown, assuming oversampled SLC images. The range subpixel position on its own does not induce any ambiguities, however, the additional phase component is not negligible.

### Ambiguity expectancy

The perpendicular baseline at which an ambiguity is expected, is related to the height difference and range subpixel position (in case of (dominant) point scatterers). If the total phase contribution of both aforementioned is  $\pi$  (or more), an ambiguous observations is likely. In figure 3.11 the possibility of an ambiguity for specific combinations of height difference, range subpixel position, and perpendicular baseline, is shown. Here the influence of noise is not taken into account, which can reduce the perpendicular baseline even more at which ambiguities are likely to occur.

### 3.3.2 Ambiguity detection and adaption

One of the differences between conventional PS processing and Nibbling is the fact that there is redundancy in the functional model, which makes observational testing and adjustment possible. Adaption of an ambiguous phase is straightforward addition or subtraction of an integer number of  $2\pi$  to an expected ambiguous phase observation. This is commonly referred to as phase unwrapping. It is reasonable to assume that a phase can be ambiguous at larger baselines, with height differences of only 5 meter. Therefore these phases should be unwrapped, to correctly estimate the topography from these observations. To unwrap these observations, use is made of the fact that there is redundancy in the functional model, when the deformation is estimated

stochastically (see section 3.4). But also that the topography is linearly related to the perpendicular baseline and that the ambiguities only occur at large baselines. For this specific case, two methods for the unwrapping are presented.

The Overall Model Test (OMT) is a test of the validity of the model and can be used to initially test selected pixels to identify double difference phase observations that may require ambiguity adjustment. Data snooping can then be used in an adaptive form, such that outliers are adjusted for their ambiguities. A decrease of the OMT test statistic shows that the model has improved, and can be used as an indicator for correcting ambiguities. We refer to this method as adaptive ambiguity adjustment.

Another method, recursive residual re-estimation, to adapt ambiguities uses the wrapped phases to correctly update the estimated components. This method works recursively, updating the estimated parameters (topography and master-offset) by re-wrapping (confining the phases to the range  $[-\pi, \pi)$  again) the residuals and re-estimating the parameters from the residuals.

### Adaptive ambiguity adjustment

In adaptive ambiguity adjustment, the ambiguities are detected using datasnooping and then adapted per arc. Here an introduction to testing theory (data snooping) is considered, including the basic equations that are required. For more information, the interested reader is referred to the literature on this subject Teunissen (2000). For testing the model, the Overall Model Test (OMT) is used as a preliminary test of significance of the estimated linear model. Assume a null hypothesis  $H_0$  and an alternative hypotheses  $H_A$ , such as

$$\begin{aligned} H_0 : \quad E\{\underline{y}\} &= A\underline{x} \\ H_A : \quad E\{\underline{y}\} &= A\underline{x} + c_{y_i} \nabla_i, \end{aligned} \quad (3.33)$$

where  $c_{y_i} \nabla_i$  models an anomaly at the  $i^{th}$  position, with  $c_{y_i} = (0, \dots, 0, 1, 0, \dots, 0)^T$ . Then the OMT statistic for the null hypothesis is defined as

$$T_{q=m-n} = \hat{\underline{e}}^T Q_y^{-1} \hat{\underline{e}}, \quad (3.34)$$

with  $T_{q=m-n}$  the OMT statistic for redundancy  $q$ ,  $\hat{\underline{e}}$  are the estimated residuals, and  $Q_y$  is the covariance matrix of the observables. Commonly if  $T_{q=m-n} > \chi_\alpha^2(m-n, 0)$ , the null hypothesis is rejected and an alternative hypothesis can be tested.

The alternative hypothesis is a test for anomalies (outliers) in the observations. These outliers are detected using the w-test, a test quantity with a standard normal distribution  $N(0, 1)$ ,

$$\underline{w}_i = \frac{c_{y_i}^T Q_y^{-1} \hat{\underline{e}}}{\sqrt{c_{y_i}^T Q_y^{-1} Q_{\hat{\underline{e}}} Q_y^{-1} c_{y_i}}}, \quad (3.35)$$

with  $Q_{\hat{\underline{e}}} = Q_y - Q_{\hat{\underline{y}}}$  the covariance function of the estimated residuals and  $Q_{\hat{\underline{y}}}$  the covariance matrix of the Best Linear Unbiased Estimator of  $\underline{y}$

$$Q_{\hat{\underline{y}}} = A (A^T Q_y^{-1} A)^{-1} A^T. \quad (3.36)$$



In this case, the OMT is used as an improvement indicator. Assuming that the largest outliers in the residuals are those interferometric phases that require adaptation, then after adaption the OMT quantity should decrease (the model is improved with respect to the adapted observation).

One of the challenges with this method is the correct use of the covariance matrices for the model, the w-test, and the OMT. The phase due to topography and range subpixel position should be linear with perpendicular baseline. However, if interferometric phase observations are ambiguous, the linear relationship for the topography changes to a sawtooth shape. For this reason the linear model is fitted with a weighting function that assigns larger weights to the observed phases at smaller perpendicular baselines. The probability of an ambiguity increases with increasing perpendicular baseline, therefore the weights must be inversely dependent on the perpendicular baseline. A Gaussian weighting function with zero mean decreases the weights with increasing perpendicular baseline,

$$\text{Diag}\{W_y\} = \frac{1}{\sigma_{B_\perp} \sqrt{2\pi}} \exp\left(\frac{-B_\perp^{0k}}{2\sigma_{B_\perp}^2}\right). \quad (3.37)$$

Here  $\text{Diag}\{\cdot\}$  indicates the diagonal of a matrix,  $W_y$  is the weights matrix,  $\sigma_{B_\perp}$  is the distribution of the perpendicular baselines assumed to be in the same (correct) ambiguity cycle. This weighting matrix is both used to determine the best linear model with respect to the interferometric phases at smaller baselines, as well as for the OMT. The best linear model is fitted to the observations with ordinary least-squares,

$$\hat{\underline{x}} = (A^T W_y A)^{-1} A^T W_y \underline{y}, \quad (3.38)$$

where  $\hat{\underline{x}}$  is the estimate of  $\underline{x}$  and  $\underline{y}$  are the observables of equation (3.33), and the matrix  $A$  contains the model parameters to convert height to phase, see equation (2.2).

For the w-test a different covariance matrix is used. If the weights of the largest baselines would be lower than those at smaller baselines, the w-test statistic will reduce for those phases at larger baselines, and increase for phases at smaller baselines. Consequently the observables at small baselines have a higher chance to be adapted (incorrectly), resulting in a higher probability that the approach fails. In the case of using the inverse of the weighting function for the w-test (higher w-test for larger baselines), some phases at smaller baseline are not adapted. For these reasons an identity matrix is used for the w-test.

Finally, if the adaptation correctly adjusted the interferometric phase, then the residuals should decrease. In other words, the OMT statistic of the estimated residuals based on the adjusted input phases should decrease. Based on this result the algorithm adaptively updates the input phases until all phases are adjusted to the correct ambiguity.

### Recursive residual re-estimation

An alternative method to solve the ambiguities is by recursive re-wrapping and updating the topography and master offset estimation of the residuals. The topography is linearly related to the perpendicular baseline, however, this relationship can be disturbed if ambiguities occur. Consequently, the determination of the topography is not straightforward and phase unwrapping is necessary.

	$\Delta H = 10m,$ $\sigma_n \sim N(0.35, 0.09)$	$\Delta H = 10m,$ $\sigma_n \sim N(0.70, 0.09)$	$\Delta H = 15m,$ $\sigma_n \sim N(0.35, 0.09)$
Adaptive Ambiguity Adjustment	99.20%	98.20%	97.84%
Recursive Residual Re-estimation	99.96%	99.96%	99.84%

Table 3.1: Table showing the confidence in both unwrapping algorithms with increasing noise and topographic error. The recursive residual re-estimation technique proves to be slightly more robust. From 2500 iterations the RMS values are compared of both methods and the simulated unwrapped phases.

The phases that have ambiguities are generally at large baselines, hence the topography is underestimated (in absolute sense). The weights in the estimation of the initial topography are—similar to the previously discussed method—a function of perpendicular baseline, see equation (3.37). The residuals after subtracting the phase components of the (under-)estimated topography are not bound to the same range as the interferometric input phases. On the contrary, those phases with ambiguities are expected to have opposite sign of the under-estimated phase components and will increase (again in absolute sense), sometimes over the range of the interferometric phases. If the residual phases are then re-wrapped, those phases out of the range  $[-\pi, \pi)$  will be adjusted with an integer number of  $2\pi$ . The residuals may therefore still contain a trend with respect to the perpendicular baseline. A recursive estimation of the trend in the residuals (the remaining topographic component) is used, after which all the partial topographic components are summed together.

The final estimation should converge to the actual topographic component of the measurement. Because the topography estimation is based on weights, and not the covariance function as described in section 3.4, the unwrapped phases have to be reconstructed. This is achieved by adding the residual phases to the final estimates (sum of the estimates of each iteration) of the topography and offset due to the master SLC noise and atmosphere.

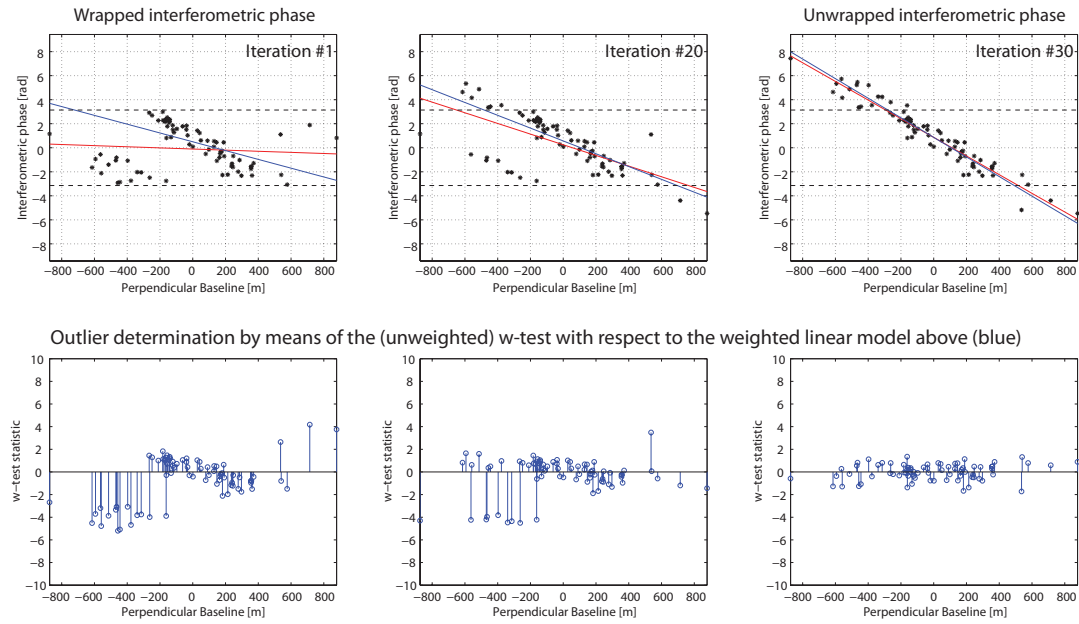
### 3.3.3 Ambiguity adaptation results

By simulating the interferometric phases, the methods two for ambiguity resolution can be validated. The phases are based on topography, range subpixel position and, master- and slave noise. The topographic phase is computed using (2.2), where a topography of 10 m is assumed. The perpendicular baselines are simulated as a normal distribution with a standard deviation of 350 m and a mean of 0 m. The range subpixel position is uniformly distributed. The atmosphere is simulated as a normal distribution with zero mean and  $\sigma_{\text{atmo}}^2 = 0.1 \text{ rad}^2$ . Finally the master noise is distributed as  $N(0, 0.26)$  rad, and slave noise  $N(0, \sigma_n)$ , with  $\sigma_n$  the slave noise standard deviation distributed as  $N(0.35, 0.09)$  rad. The variance of the slaves is set slightly higher to account for coregistration errors (Kampes, 2005). In total 75 interferometric phases are simulated.

Figure 3.12 shows the two methods together, with the top six figures showing the adaptive ambiguity adjustment method, and the bottom six figures the recursive residual re-estimation method. The weighting matrix has been optimized for the best weighting ratio with respect to the perpendicular baseline.

— Weighted linear model  
— Unweighted linear model

### Adaptive Ambiguity Adjustment



### Recursive Residual Re-estimation

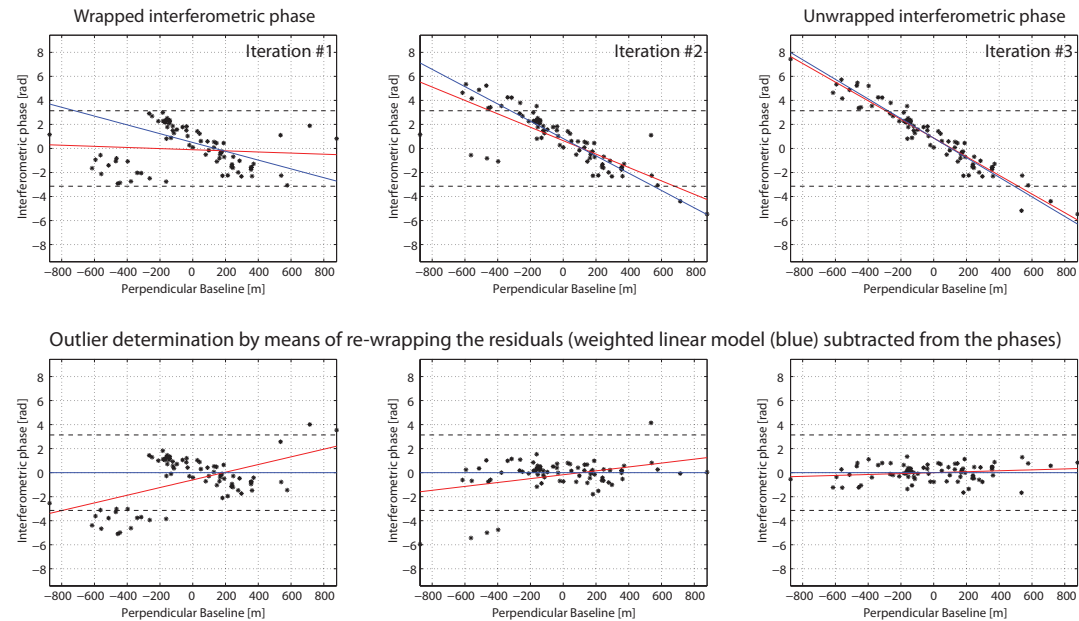


Figure 3.12: The two recursive ambiguity resolution methods for the unwrapping of the ambiguities at larger perpendicular baselines. Both give the same result in the shown simulated case, however the number of iterations is significantly different. The top six images belong to the Adaptive Ambiguity Adjustment technique, whereof the top three images show the (semi-)unwrapped phases. These are updated every iteration by identifying the outlier in the unweighted w-test. The w-test statistic is shown below the phases and give an indication where the outliers are. The lower six images belong to the recursive residual re-estimation, whereof the top three images again show the (semi-)unwrapped phase. The outliers are detected by subtracting the weighted linear model from the (semi-)unwrapped phases and adapting only those phases that are over  $2\pi$  (in absolute sense).

The methods are validated by comparing the RMS values of the estimated residuals of the wrapped phases, with the residuals of the (known) unwrapped phases. If this is a non-zero value then the approach failed. This test is performed 2500 times for three different settings of the slave noise and simulated topography, and the results are shown in table 3.1. From this table, it can be concluded that both methods work equally well, although the amount of failures for increasing topography and slave noise increases more rapidly for the adaptive ambiguity adjustment. However, only one weighting function for this approach is tested, and can improve the success rate of the algorithm. From figure 3.12 it can be seen that the number of iterations for the recursive residual estimation is smaller, hence this method is computationally more efficient. Mainly because of this reason the recursive residual re-estimation procedure is incorporated in the Nibbling approach.

### 3.4 Mathematical framework

The functional model for Nibbling is different from conventional PS processing, because it is assumed that the phase difference between the neighboring pixels is within the same ambiguity cycle. This removes the rank-deficiency and improves the functional model such that there is redundancy. Hence, the pseudo-observations are removed from the functional model and consequently changes the stochastic model. Here two models are proposed, firstly where the deformation is modeled functionally and secondly where it is modeled stochastically. Here we omit the indications of stochasticity to decrease the complexity of the equations.

#### 3.4.1 Functional model

A dataset contains  $k_{\text{SLC}} = 0 \dots K$  SLC images, with the master  $k_{\text{SLC}} = 0$  and slaves  $k = 1 \dots K$  giving a total of  $K$  interferograms. The processing is performed with a single master and the interferometric phases of the master-slave interferograms are written as  $\varphi^{0k}$ . Recall the contributions to the phase observations, equation (2.1), then the double-difference phase (an arc) between neighboring pixels  $x$  and  $y$  (where  $x$  and  $y$  each contain the pixel coordinates in range and azimuth) is

$$\varphi_y^{0k} - \varphi_x^{0k} = \varphi_{xy}^{0k} = \varphi_{H_{xy}}^{0k} + \varphi_{D_{xy}}^{0k} + \varphi_{S_{xy}}^{0k} + \varphi_{n_{xy}}^{0k}, \quad (3.39)$$

where  $H_{xy}$  denotes the topographic difference,  $D_{xy}$  is the deformation difference,  $S_{xy}$  the atmospheric difference, and  $n_{xy}$  is the noise difference between pixels  $x$  and  $y$ . Here the phase components of the orbital errors are assumed to be corrected for, with the precise orbits supplied by the TUDelft (Scharroo and Visser, 1998). The phase components induced by the scattering characteristics are neglected (i.e. these are now part of the noise component and are expected to be small), and finally the phase differences are assumed to have no ambiguities. The master and slave components can be separated into

$$\begin{aligned} \varphi_{xy}^{0k} = (\varphi_{H_y}^{0k} - \varphi_{H_x}^{0k}) &+ \left( (\psi_{D_y} - \psi_{D_x})^k - (\psi_{D_y} - \psi_{D_x})^0 \right) \\ &+ \left( (\psi_{S_y} - \psi_{S_x})^k - (\psi_{S_y} - \psi_{S_x})^0 \right) \\ &+ \left( (\psi_{n_y} - \psi_{n_x})^k - (\psi_{n_y} - \psi_{n_x})^0 \right). \end{aligned} \quad (3.40)$$

Pixel  $x$  will be used as a spatial reference pixel with respect to its neighbors, i.e., the phases of the reference pixel are assumed zero and the parameters of the neighboring pixel is estimated

relative to the reference. In other words  $\varphi_{H_x}^{0k} = 0$ ,  $\varphi_{D_x}^{0k} = 0$ ,  $\psi_{S_x} = 0$ , and  $\psi_{n_x} = 0$ . Furthermore, the master will be the temporal reference and implies that  $\psi_{D_x}^0 = \psi_{D_y}^0 = 0$ . The differences will now be indicated by a  $\Delta$ , to make it clear that the estimated parameter is related to the reference pixel  $x$ . This is substituted in equation (3.40) and simplified to

$$\varphi_{xy}^{0k} = \varphi_{\Delta H}^{0k} + \varphi_{\Delta D}^{0k} + \varphi_{\Delta S}^{0k} + \varphi_{\Delta n}^{0k}, \quad (3.41)$$

which can be re-written, using equations (2.2) and (2.3), to

$$\begin{bmatrix} \varphi_{xy}^{01} \\ \vdots \\ \varphi_{xy}^{0K} \end{bmatrix} = \begin{bmatrix} -\frac{4\pi}{\lambda} \frac{B_{\perp}^{01}}{R \sin(\theta)} & -\frac{4\pi}{\lambda} t^{01} & 1 \\ \vdots & \vdots & \vdots \\ -\frac{4\pi}{\lambda} \frac{B_{\perp}^{0K}}{R \sin(\theta)} & -\frac{4\pi}{\lambda} t^{0K} & 1 \end{bmatrix} \begin{bmatrix} \Delta H \\ \Delta D \\ M_{xy} \end{bmatrix} + \begin{bmatrix} \psi_{\Delta S}^1 \\ \vdots \\ \psi_{\Delta S}^K \end{bmatrix} + \begin{bmatrix} \psi_{\Delta n}^1 \\ \vdots \\ \psi_{\Delta n}^K \end{bmatrix}, \quad (3.42)$$

in which  $M_{xy} = \psi_{\Delta S}^0 + \psi_{\Delta n}^0$  is the master dependent term, equally present in each interferogram but not constant for all arcs. This equation shows all contributions to the observed phase. The terms including the slave atmosphere and slave noise are modeled stochastically. Essentially this master dependent term causes an offset of the interferometric phase observations. The system of equations requires a time-dependent model, e.g. linear, of the deformation at  $t^{01} \dots t^{0K}$  (the time with respect to the master). Estimating the deformation time-series, i.e. without a deformation model, will make the system rank-deficient (more unknowns than observations), hence unsolvable. For this reason a model for the deformation is assumed in order to parameterize the deformation and keeping the system of full rank.

To avoid the use of a strict deformation model, the deformation can be modeled stochastically. The residuals would then contain three independent random variables, hence the variance of the residuals is the sum of the variances of each of the random variables. The atmosphere is spatially very correlated within short distances, therefore the variance of the atmosphere between neighboring pixels in the same SLC should be very small ( $\sigma_{\psi_{\Delta S}}^2 < 0.1 \text{ rad}^2$  (Williams et al., 1998)). Furthermore, for coherent scatterers the noise variance is low, however, the noise is not spatially nor temporally correlated. Finally the variance of the deformation is expected to dominate the total variance and is both spatially and temporally correlated. The system of equations now excluding the deformation from the functional part is

$$\begin{bmatrix} \varphi_{xy}^{01} \\ \vdots \\ \varphi_{xy}^{0K} \end{bmatrix} = \begin{bmatrix} -\frac{4\pi}{\lambda} \frac{B_{\perp}^{01}}{R \sin(\theta)} & 1 \\ \vdots & \vdots \\ -\frac{4\pi}{\lambda} \frac{B_{\perp}^{0K}}{R \sin(\theta)} & 1 \end{bmatrix} \begin{bmatrix} \Delta H \\ M_{xy} \end{bmatrix} + \begin{bmatrix} \psi_{\Delta S}^1 \\ \vdots \\ \psi_{\Delta S}^K \end{bmatrix} + \begin{bmatrix} \psi_{\Delta n}^1 \\ \vdots \\ \psi_{\Delta n}^K \end{bmatrix} + \begin{bmatrix} \psi_{\Delta D}^1 \\ \vdots \\ \psi_{\Delta D}^K \end{bmatrix}. \quad (3.43)$$

### 3.4.2 Stochastic model

The stochastic model contains the superposition of all model imperfections, noise components, and parameters that are not modeled in the functional model. In the previous section, the deformation is initially modeled functionally assuming a certain type of deformation, e.g. linear. Functionally modeling the deformation leads to the same covariance matrix as is used in conventional methods for PSI. The covariance matrix will be diagonal symmetric and with assumptions on similarity of arc length and coherence will be equivalent to equation (2.18).

To investigate the components responsible for the variance of the derived variates  $\varphi_{xy}^{0k}$  the influence of the constituting variates is propagated. This is proposed by Hanssen (2004), where the derived variates are the double differences. The variances of the double-difference phases are

$$\sigma_{\varphi^{0k}}^2 = \sum_{p=x,y} \sum_{q=0,k} \sigma_{\psi_p^q}^2 - 2 \left( \sigma_{\psi_x^0, \psi_y^0} + \sigma_{\psi_x^k, \psi_y^k} + \sigma_{\psi_x^0, \psi_x^k} + \sigma_{\psi_y^0, \psi_y^k} \right) \quad (3.44)$$

and the covariances

$$\sigma_{\varphi^{0k}, \varphi^{0n}} = \sum_{p=x,y} \sigma_{\psi_p^0}^2 - 2\sigma_{\psi_x^0, \psi_y^0} - \sigma_{\psi_x^0, \psi_x^k} - \sigma_{\psi_y^0, \psi_y^k} - \sigma_{\psi_x^0, \psi_x^n} - \sigma_{\psi_y^0, \psi_y^n} + \sigma_{\psi_x^k, \psi_x^n} + \sigma_{\psi_y^k, \psi_y^n}, \quad (3.45)$$

with

- $\sigma_{\psi^k}^2$  the total variance of the SLC phase observations consisting of thermal-, scattering noise, remained atmospheric-, and orbital signal for pixel  $x$  in SLC  $k$ .
- $\sigma_{\psi_x^k, \psi_y^k}$  the spatial covariance between two pixels  $x$  and  $y$  within the  $k^{\text{th}}$  SLC dominated by the atmospheric- and orbital signal and spatial component of the deformation.
- $\sigma_{\psi_x^k, \psi_x^n}$  the temporal covariance of a single pixel  $x$  between two coregistered SLC images  $k$  and  $n$  dominated by the effects of temporal coherence and temporal component of the deformation.

The difference between the stochastic model of conventional PSI processing and Nibbling is within the simplification of the covariances. The variances of the SLC phase observations are assumed to be constant, however, to account for coregistration errors the variances of pixels in the slave images are assumed to be higher than the variances in the master image. Furthermore, the covariances of neighboring pixels in an SLC are expected to be constant as well, because of the large spatial correlation of the atmosphere and deformation with respect to the distances between the neighboring pixels. Finally, the temporal covariances are estimated using a covariance model to account for the (functionally unmodeled) correlation of the deformation. These assumptions lead to the following simplified variances

$$\sigma_{\varphi^{0k}}^2 = 2\sigma_{\psi^0}^2 + 2\sigma_{\psi^k}^2 - 2 \left( 2\sigma_{\psi_x, \psi_y} + 2\sigma_{\psi^0, \psi^k} \right) \quad (3.46)$$

and the covariances

$$\sigma_{\varphi^{0k}, \varphi^{0n}} = 2\sigma_{\psi^0}^2 - 2\sigma_{\psi_x^0, \psi_y^0} - 2\sigma_{\psi^0, \psi^k} - 2\sigma_{\psi^0, \psi^n} + 2\sigma_{\psi^k, \psi^n}. \quad (3.47)$$

Ketelaar (2008) shows an example of a stochastic model for the estimation of subsidence due to hydrocarbon production. In this model, the temporal behavior of the deformation is modeled with an exponential function. For WDS the behavior of the deformation will be similar, assuming that the deformation rate will decrease with time because of settling. In addition the choice of the temporal covariance model for the deformation does not restrict the deformation behavior to only this model. It is expected that an exponential covariance model, e.g.,

$$\sigma_{\psi^n, \psi^k} = \sigma_{\text{defo}}^2 e^{\left( -\frac{t^{nk}}{T_{\text{defo}}} \right)^2} \quad (3.48)$$

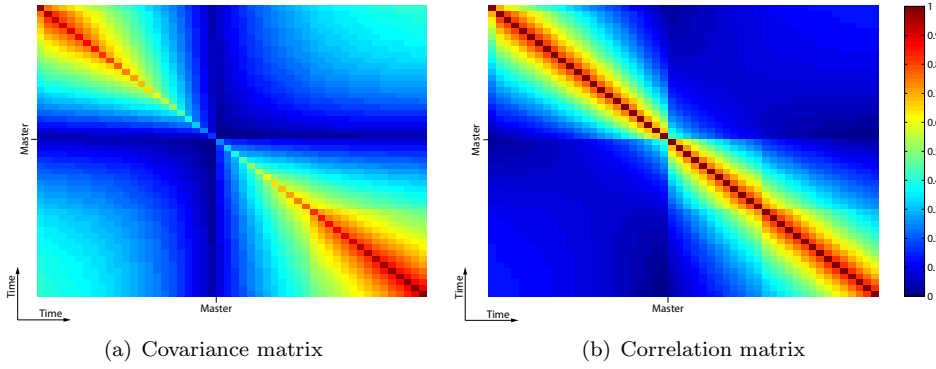


Figure 3.13: The shapes of the covariance and correlation matrices based on the described stochastic model, including the stochastically modeled deformation. The correlation decreases for interferograms with a larger relative temporal baseline. A larger temporal baseline between consecutive interferograms is the cause for the artefacts, clearly seen in the correlation matrix.

would represent the deformation well, due to settling. Here  $\sigma_{\text{defo}}$  is the variance of the deformation,  $t^{nk}$  is the temporal baseline between the SLC images  $n$  and  $k$ , and  $T_{\text{defo}}$  is the temporal correlation length of the deformation. The temporal decorrelation length in the order of one year would be appropriate, but it remains case dependent. There are alternative models that may be appropriate for deformation on water defense structures. A linear model linear, if the deformation within the timeframe is continuous without decrease, this is possible if the WDS is old. A linear model including a breakpoint can be used when a sudden change in the deformation rate is considered. Finally a periodic model may be valid in case the fluctuations of an external force (weather or groundwater level) are correlated with the deformation rate.

To incorporate the spatial correlation of two adjoining pixels in the mathematical model, the covariances ( $\sigma_{\psi_x \psi_y}$ ) should be estimated based on the theoretical correlation, discussed in section 3.2. This is not necessarily a straightforward procedure, because the variances are not well determined. Furthermore, the theoretical correlation only includes distributed scatterers, which may not be completely valid. Therefore, the correlation is not taken into account in the mathematical model.

Figure 3.13(a) shows the shape of the covariance matrix based on the described stochastic model with an exponentially modeled stochastic deformation. The diagonal of the matrix shows a decrease of variances for the interferograms with the smallest temporal baselines (close to the center of the matrix). The covariances are related to the variances and show similar behavior, i.e., a lower variance results in a lower covariance. The smallest covariances (with respect to the variances) are found for the interferograms with the largest respective baseline (the upper-right and lower-left corners). This implies that the correlation and covariance decreases if the time between two acquisitions is very large.





## Chapter 4

# Results and Discussion

To investigate the capabilities of the Nibbling approach on empirical data, a test area is selected which should have coherent scattering along the line infrastructure. The acquired deformation from Nibbling can then be validated with respect to conventional processing (DePSI). The area of interest is a WDS in the Netherlands known as the Hondsbossche en Pettemer zeewering. Here conventional PS results are available for validation.

Characteristics of the area are given in section 4.1, followed by the results of conventional PS processing in section 4.2. Section 4.3 discusses the preliminary test results based on the mathematical framework of section 3.4. Here only neighboring (adjacent) pixels are used for the estimation of the parameters of interest (topographic error and deformation time series). To improve the results, further investigation in processing on non-adjacent neighboring pixels is conducted in section 4.4. Finally these results are discussed in section 4.5, where more improvements are made. The methodological differences between Nibbling and DePSI are described in section 4.6 in which the specifics of Nibbling are discussed and future improvements are suggested.



Figure 4.1: The Hondsbossche Zeewering (left and center) and its location in the Netherlands (right).  
[Satellite images: Google Earth]

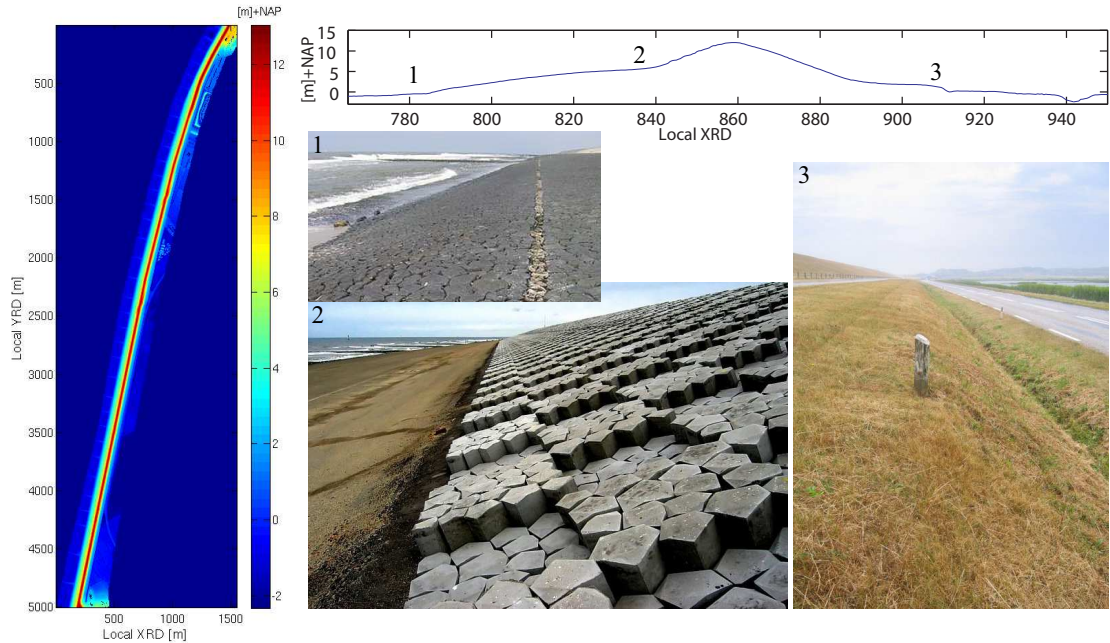


Figure 4.2: The DEM and profile of the Hondsbossche Zeewering with images of the respective areas indicated with a number. Images taken during fieldwork in 2008. [Elevation data: Hoogheemraadschap Hollands Noorderkwartier]

## 4.1 De Hondsbossche zeewering

The Hondsbossche en Pettemer zeewering (now referred to as the Hondsbossche zeewering) is located on the western coast of the Netherlands in the province of North-Holland, indicated in figure 4.1. It stretches approximately six kilometers between the cities of Petten and Groet. This dike is considered to be a weak link in the Dutch defense against flooding (Hoogheemraadschap Hollands Noorderkwartier, 2008). In this report the weakness is tested based on the transfer rate of water per meter of the WDS (in liter/second/meter). They conclude that the wave exceedance frequency is not within the norm of 1/10.000 per year (average), and therefore the wave exceedance probability is too high.

### 4.1.1 Characteristics of the area

The WDS under consideration is an interesting area which may be subject to different types of deformation. Suggestions include the compaction due to reinforcements, and hydrocarbon production in Groet (1974-2004) (Barends, 2008a). The compaction mainly results in a deformation at the top of the WDS, reducing towards its base (Barends, 2008b). Its non-homogeneous nature along the WDS is the result of reinforcing it in stages (Zuidweg, 1997). Another (currently still debated) type of deformation is the hydrocarbon production near Groet. The influence of hydrocarbon extraction near Groet possibly stretches underneath the southern part of the Hondsbossche zeewering, hence it is expected that the southern part will subside more than the north. In 2004 the hydrocarbon production was stopped, which should reduce the subsidence in the future, if there indeed was an influence because of this.

In 2004 and 2005 the outer wall of the Hondsbossche zeewering was strengthened, by adding reinforcements, which included the addition of basalt-blocks on the outer wall, see picture two in figure 4.2. The addition of these blocks during the acquisition time span of the data causes the signal of this area to decorrelate. Before 2004 this area consisted of vegetation, which is one of the limitations of PSI, because of its quick-changing reflective characteristics resulting in loss of coherence. Since the finish of this reinforcement in 2005, approximately 25 radar images have been captured which should be enough for PSI to identify PS on the area containing these basalt-blocks. The deformation that is captured in this timespan will include the compaction due to the addition of these blocks and can be vital to the understanding of the dynamics of the top of the WDS and therefore its stability. Furthermore, the hydrocarbon production in Groet stopped in 2004 and the results of this dataset can reveal information on the influence of the hydrocarbon production on the stability of the Hondsbossche zeewering.

#### 4.1.2 Available dataset

The dataset used for the study of this area consists of 51 coregistered SLC images acquired by Envisat. The images are acquired with almost homogeneous time sampling, where the shortest sampling interval is 35 days. The time span of the acquisitions is more than five years, with the first image acquired in 2003. The images of this set are taken in the descending orbit, which implies that the satellite travels to the south looking from the east to the west. A table with the available images and important parameters are given in appendix B.

The SLC images are processed with DORIS and are oversampled with a factor 2 before the coregistration and interferogram formation. Oversampling is performed to avoid aliasing after the complex multiplication of the SLC images to form the interferograms. Since a multiplication in space domain is equivalent to a convolution in the frequency domain, the frequency spectrum will be doubled in the interferogram formation step. Oversampling is the addition of zero valued rows and columns to the frequency spectrum of the SLC images, also known as zeropadding (Curlander and McDonough, 1991).

In this case study only the descending tracks are used, in which coincidentally the flight direction of the satellite is approximately parallel to the Hondsbossche zeewering. Because of this coincidence the assumption can be made that the measured deformation will only occur in the direction perpendicular to the longitudinal direction of the WDS. The LOS deformation is a projection of the actual direction of the deformation in the scene. A vector decomposition may be important for interpreting the direction and magnitude of the deformation, because there is a fundamental difference between shear deformation along the surface and vertical deformation in relation to the stability of the WDS. Such a vector decomposition is illustrated in figure 4.3, which is the actual cross section of the Hondsbossche zeewering from data acquired with airborne laserscanning. In this figure the black arrow illustrates the LOS (measured) deformation, the two red arrows show the shear and vertical deformation related to the same LOS deformation. This figure shows that the magnitude of the actual deformation will always be larger, if the actual deformation is not in LOS of the satellite look direction. The magnitude of the deformation is related to the angle of the actual deformation with respect to the look angle of the satellite. The only method to resolve the actual direction and magnitude of the deformation is by incorporating data acquired from the ascending orbit.

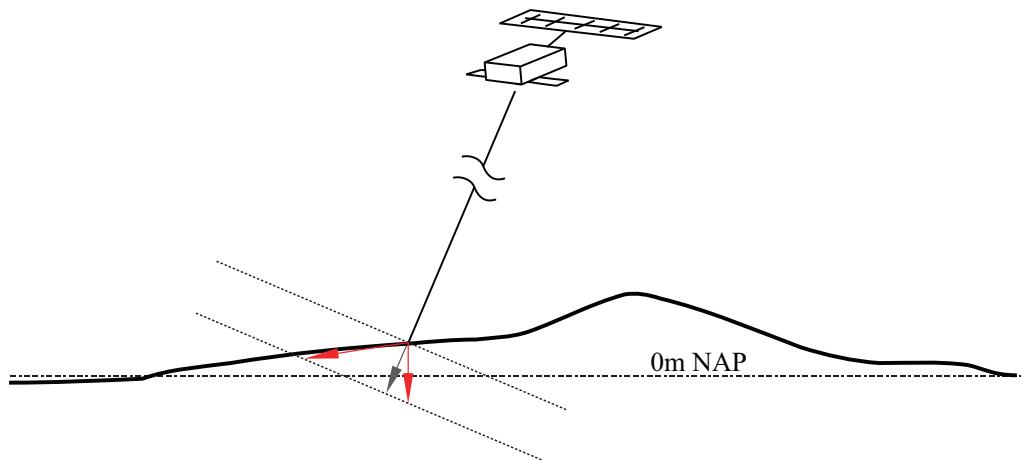


Figure 4.3: A vector decomposition for the descending track. The actual deformation, which in this case can be either of the red arrows, is a projection on to the LOS deformation (black arrow). The size and direction of the actual deformation can only be obtained by including the deformation of ascending track.

## 4.2 Conventional PS processing

The results for this area with conventional PSI (Delft implementation of PSI, or DePSI for short) are presented by van Leijen et al. (2008). In this section, a more detailed setup of the processing and the results of the deformation and topography of the WDS are shown. These results will act as a benchmark to which the Nibbling results will be compared and validated. Here it is assumed that the results acquired from DePSI are correct.

### 4.2.1 Processing setup

The pre-processing steps comprising of cropping, coregistration, interferogram computation, and reference phase subtraction, are performed using DORIS. As a reference Digital Elevation Model (DEM), a flat plane is used, because of the small variations in topography in the Netherlands. In this case the residual topography is therefore equal to the topographic height in the scene. The master image is acquired on August 10, 2005 (orbit number 18012) and is centrally (spatially and temporally) located, such that the predicted coherence of the interferogram stack is maximum (Kampes, 2005). The baseline plot of the dataset is shown in figure 4.4, a more detailed table of the dataset is shown in appendix B.

The first order PS candidates in the PSI processing are selected based on the normalized amplitude dispersion, using empirically calibrated images (Ketelaar et al., 2005). From the selected pixels a network is created, connecting the eight closest first order candidate PS with each other. Because of the high density of PS over the WDS, the network becomes dense which improves the prediction of the atmosphere in that area performed with kriging interpolation.

In this case an area of interest is selected which only includes the Hondsbossche zeewering. Because no tests are performed to identify and correct any ambiguities of the phases within the

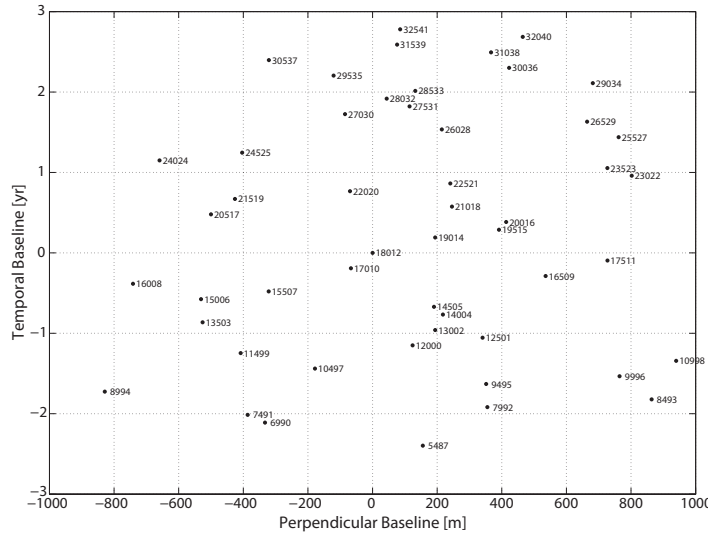


Figure 4.4: Baseline plot of the Envisat ASAR SLC images used for the processing of the Hondsbossche zeewering. The numbers in the figure indicate the orbit numbers.

area of interest, all pixels in this area (even those located in the water and on vegetated areas) are selected and estimated. Therefore the resulting deformation seems very noisy and filtering of the results is required.

For the filtering of the data the estimated ensemble coherence 2.2 is used together with the spatio-temporal consistency (STC) (Hanssen et al., 2008; Esfahany et al., 2008). Furthermore, there is a filter based on extreme topographic heights and deformation rates. All the filters are based on the distributions of the attributes, and are specifically chosen for this dataset. The temporal coherence threshold is set to 0.6, excluding any estimated observation below that threshold. The topography is filtered on the extreme values of  $\pm 20$  meter from the mean. With the deformation, rates of  $\pm 6$  mm/yr from the mean are excluded from the set.

The STC is a relation which describes the spatial and temporal behavior of PS with respect to nearby PS. When comparing a group of PS, no temporal model assumptions are required, and the dispersion between the observations would reflect measurement quality. The neighboring PS are in this case neglected to eliminate consistent values of the STC based on the sidelobes of dominant point-like scatterers, therefore a minimum and maximum range is defined between which all PS are considered. The double-difference phases with respect to the PS in consideration are calculated. The relation that describes the behavior of the PS is the minimum root-mean-squared (RMS) error of the nearby PS,

$$\xi = \min_{\forall y} \frac{\lambda}{4\pi} \sqrt{\frac{1}{K-1} \sum_{k=1}^{K-1} \left( (\phi_x^k - \phi_y^k)(\phi_x^{(k+1)} - \phi_y^{(k+1)}) \right)^2}. \quad (4.1)$$

denoted as the STC ( $\xi$ ). Here  $x$  is the PS under consideration,  $y$  is the neighboring PS,  $K$  is the number of interferograms, and  $\phi^k$  is the unwrapped phase at epoch  $k$  in the deformation

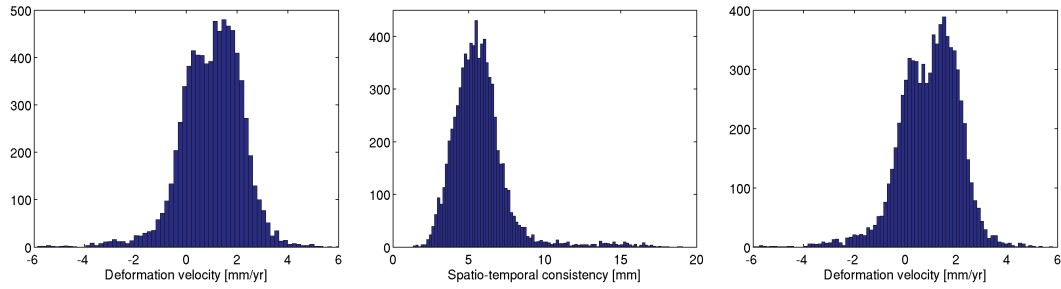


Figure 4.5: The left and right side figures show the distributions of the estimated deformation velocities before and after STC filtering, respectively. In the center the distribution of the STC values is shown, on which the threshold of 10 mm is based.

time series. The double differences are thus computed between neighboring PS in space and time. The minimum RMS best represents the measurement noise, because the spatial behavior of the deformation is assumed to be minimized. Consequently a large value for the STC relates to arcs with large measurement noise and will not show consistent behavior with respect to its surrounding PS. The STC cannot be calculated for isolated PS, for which no PS are within its minimum and maximum range. The STC is an alternative quality indicator, complementary to the temporal coherence, and independent to the processing chain. The STC distribution is shown in the center histogram of figure 4.5, with on the left and right side the deformation rates before and after STC filtering. Observations with a STC over 10 mm are removed.

#### 4.2.2 Results

The processed and filtered results with conventional PSI are presented in figure 4.6. These results will be used as a benchmark for validating the Nibbling algorithm. Here it is assumed that the results of DePSI are correct, based on previous validations (Marinkovic et al., 2008; van Leijen et al., 2008; Esfahany et al., 2008; Ketelaar, 2008).

The resulting deformation of the Hondsbossche zeewering shows a significant tilt to the south of approximately 2.2 mm/yr with respect to the north. Currently it is heavily debated if this tilt is an influence from the hydrocarbon production in Groet until 2004. In case this tilt is caused by non-anthropogenic mechanisms, then this effect could possibly be extrapolated to a deformation tilt of 22 cm/century. This is in the same order as the sea-level rise of approximately 20 cm/yr and therefore significant (van Leijen et al., 2008). Another hypothesis for the tilt is asymmetrical compaction (geomechanical mechanisms).

Another deformation effect that is visible, is a wave pattern with differences of approximately 3 mm/yr respectively. It is not exactly clear why this wave pattern of deformation is found on the WDS. Van Leijen et al. (2008) discusses natural sand replacement near the groyne<sup>1</sup> along the coast, which could explain deformation that is part of this pattern. However, the groynes and the wave pattern of the deformation are not completely correlated. An alternative hypothesis for this pattern as a relation with respect to the internal dike structure changes along the WDS. The consistency of the material (mainly clay and sand) used to construct the dike internally or the

<sup>1</sup>Groyne definition: a low wall built out from the coast into the sea, to prevent the continual movement of the waves from removing parts of the land. [*Cambridge dictionary*]



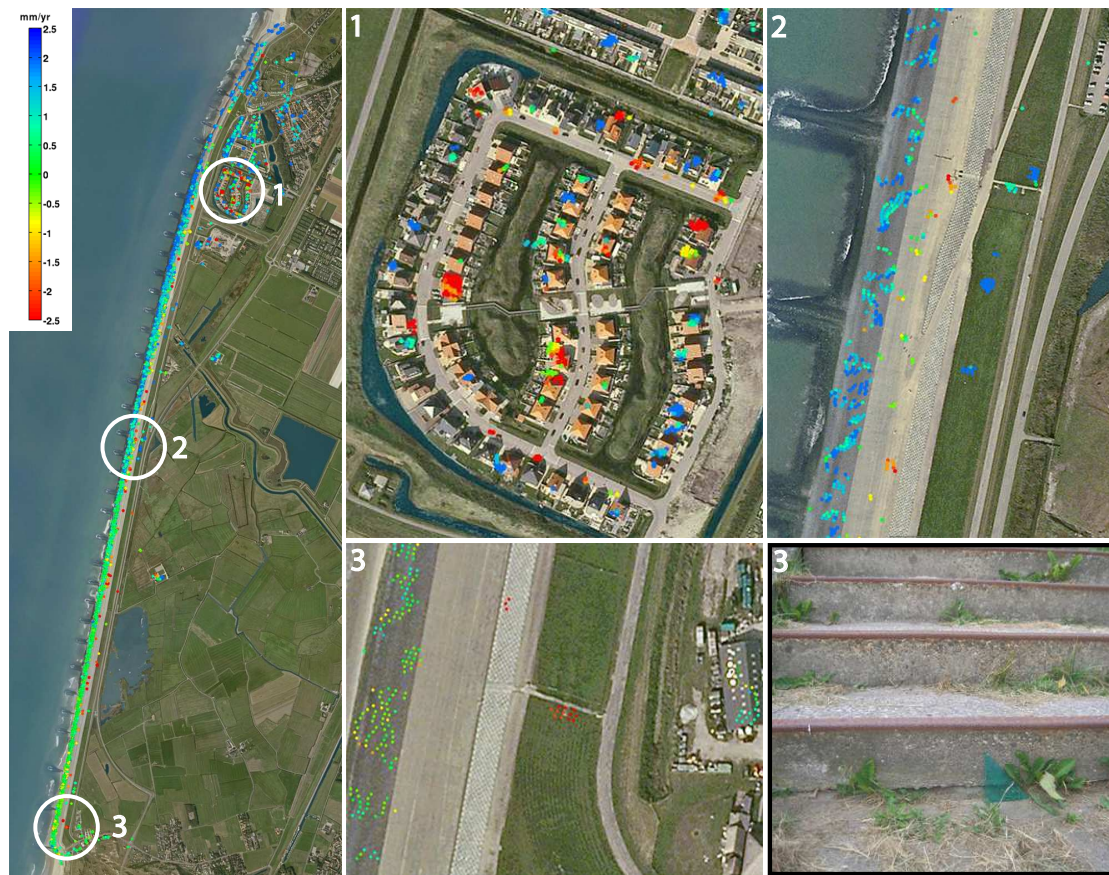


Figure 4.6: The result using DePSI processing. All PS are relative to a reference point in the city of Groet. This shows a trend in the deformation, where the magnitude of the LOS deformation is approximately 2.2 mm/yr larger in the south with respect to the north. Three close-up images are shown, 1 shows the city of Petten with very large local deformation of several houses, 2 shows the WDS halfway in which it becomes clear that not all pixels are identified as PS on the WDS, and 3 shows a very large local deformation which was verified during field-work in 2008. [Satellite images: Google Earth]

deeper lying material on which the dike is constructed can change spatially, causing differences in the deformation.

Interesting observations of very local deformation with a large magnitude with respect to its surroundings are identified. Local deformation rates of over 2.5 mm/y are observed in the city of Petten, located on houses within a relatively new part of the city. Another observation of extremely local deformation is in the south, which is located on some stairs on the WDS. The picture taken there (in 2008) confirms the deformation, see figure 4.6.

Finally the number of identified PS does not completely cover the WDS. There are open areas where no PS are identified with the filtering as described in section 4.2.1. This can either be a result of too rigorous filtering of the area of interest, e.g., values for the temporal coherence threshold or STC threshold. Other assumptions can be that the noise of those pixels is only slightly too high that the PS is rejected, or the atmosphere is not correctly or completely filtered in

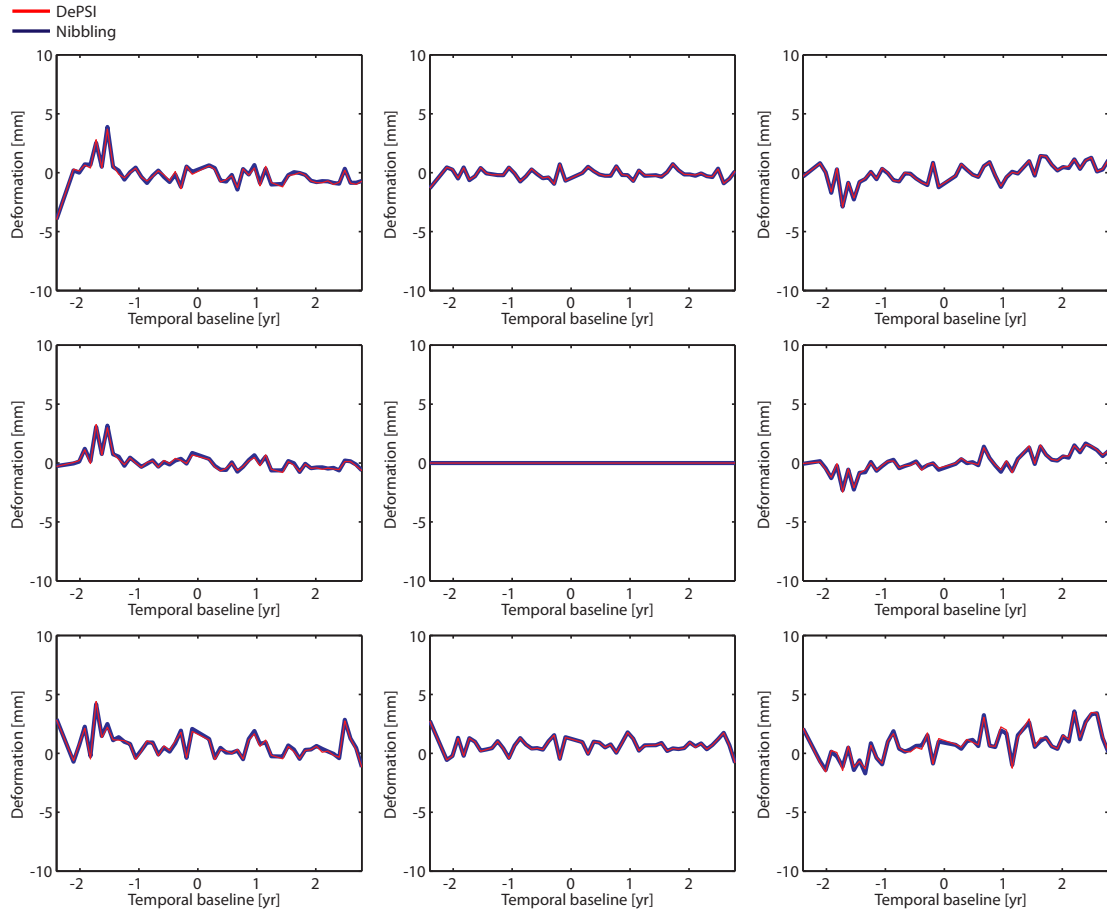


Figure 4.7: These nine plots represent a block of  $3 \times 3$  adjacent pixels, showing the time series and the trend of the deformation. Conventional processing results are shown in red, and Nibbling is shown in blue. The differences of the time series for each epoch between the two methods is in the sub-mm range.

these areas. It could also be physically related, implying that these pixels actually are incoherent (e.g., flooding at the base of the WDS, or surface changes due to maintenance).

### 4.3 Nibbling

The Nibbling method has been discussed in chapter 3. In this case study, the deformation is estimated stochastically by including it in the covariance matrix. To resolve any ambiguities, the recursive residual re-estimation procedure (3.3.2) is used. In the following sections the results of the implemented Nibbling algorithm are discussed.

#### 4.3.1 Validation of the parameter estimation

The first step in the implementation of the Nibbling approach is to evaluate whether an equivalent deformation time-series can be determined with respect to conventional processing. For



Topography [m]								
DePSI			Nibbling			Difference		
3.2263	0.0934	-3.0528	3.1635	0.0189	-3.1754	0.0628	0.0745	0.1226
3.1849	0	-3.2089	3.2078	0	-3.2459	-0.0230	0	0.0371
3.0830	-0.1647	-3.5024	3.1393	-0.1028	-3.4187	-0.0563	-0.0619	-0.0837

Deformation [mm/yr]								
DePSI			Nibbling			Difference		
-0.1996	-0.2418	-0.2357	-0.1873	-0.2340	-0.2284	-0.0123	-0.0079	-0.0072
0.0045	0	-0.0014	0.0078	0	-0.0033	0.0033	0	0.0019
0.3305	0.3860	0.4898	0.3302	0.3793	0.4750	0.0003	0.0067	0.0148

Table 4.1: The values of the estimated topography and deformation of figure 4.7 and the differences between the two methods.

this a test setup was designed to specifically select those adjacent pixel sets that are coherent in DePSI. This will visualize the results of the deformation time series together with the results from Nibbling. The differences between the two methods are then analyzed to investigate whether the differences are dependent on time or perpendicular baseline. This gives insight to the errors in deformation and topography, but is also used to improve the implementation of the estimation procedure.

Figure 4.7 shows nine plots of the deformation time series for all eight neighboring pixels in the 1-layer kernel, see figure 3.2(a). The deformation time series of both DePSI and Nibbling are shown with respect to each other, referenced to the center pixel. The differences of the difference in estimated topography and deformation rate are given in table 4.1. The estimated temporal coherence of all neighbors is larger than 0.95. The Nibbling approach is able to estimate the topography and deformation close to the estimated deformation of conventional processing. The differences between the two estimations may be caused by

1. the stochastic model and estimation of the variance covariance model is different. In DePSI the variance component estimation is used for supplying the (co-)variances, whereas in Nibbling it is defined on a-priori knowledge of the physical behavior of coherent scatterers.
2. atmospheric signal is modeled and removed in conventional processing, whereas in Nibbling the atmosphere is expected to cancel out mostly due to the spatial correlation and temporal decorrelation. However, the residual atmosphere in the deformation time series is assumed to be smaller than the noise.

### 4.3.2 Nibbling results

The initial setup for the Nibbling approach is to estimate the eight neighboring pixels and to identify PS based on their temporal coherence. To accomplish this, the coherence threshold is set to 0.99 ( $\gamma_{\max}$ ) and relaxed gradually to a minimum of 0.7 ( $\gamma_{\min}$ ). The start value of the coherence threshold is set extremely high, because of the correlation between adjoining resolution cells and to initially select only very good PS. During a processing iteration with a single coherence threshold, all pixels surrounding the 100 selected seed pixels are tested. A higher coherence threshold implies that the noise in the residual deformation time series is small. By relaxing

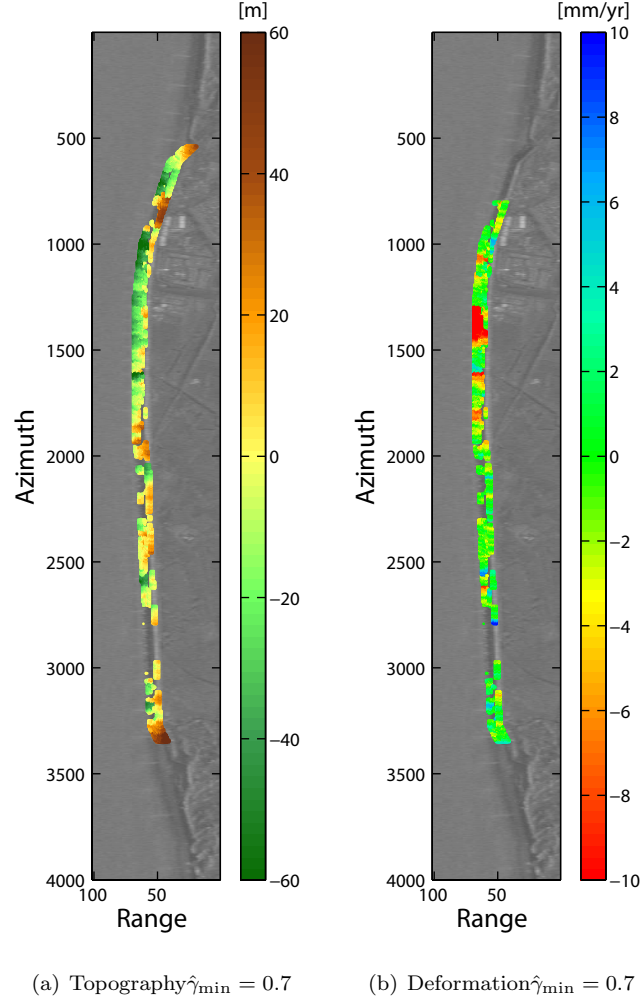


Figure 4.8: The topography and deformation results of processing only adjoining pixels, with the minimum coherence threshold was set to 0.7. Not all identified PS have the same reference point, in other words there are regions that are not merged still present in the result.

the threshold gradually to a minimum the integration paths will be directed along the WDS through PS that are estimated with high confidence first. Pixels with high confidence generally have smaller errors (high temporal coherence) and reduce the propagation of errors throughout the WDS.

Figure 4.8 show the initial results of the topography and deformation of Nibbling. Although many pixels are selected as PS with a high coherence threshold, the topography shows a variation of more than 60 meter, whereas the actual WDS does not vary more than 15 meters (see figure 4.2). Furthermore pixels which are certainly water or vegetation are identified as PS and consequently introduce errors in the estimations performed relative to those pixels. This results in a strange deformation pattern, which shows very large fluctuations and is obviously incorrect, with respect to the results of DePSI.

### 4.3.3 Analysis of adjoining pixels

To investigate the consequences of adjoining pixel processing an analysis is performed. Although it is clear that there is correlation between adjoining pixels, it is still unknown how this propagates to the estimated temporal coherence, the deformation, and the topography. Furthermore, an estimate of the complex correlation of adjoining pixels is made, to evaluate the theoretically estimated correlation of section 3.2. This analysis aids the development of the Nibbling approach and shows how these parameters are effected by the correlation of adjoining pixels.

For the empirical analysis described here, 1000 pixel pairs are used located on water within the used dataset. Water contains only random phases, and the pixel pairs should therefore not be temporally coherent, contain any topography, or deformation. Furthermore, the analysis is performed in three directions which are azimuth, range, and diagonal<sup>2</sup>. Finally the distance between the pixels is increased from zero, to one, and to nine, where the correlation between pixels with a separation of nine is expected to be completely uncorrelated. This is performed, to investigate the changes of these parameters with increasing spatial distances.

#### Complex correlation

The complex correlation coefficient (Bamler and Hartl, 1998) is calculated empirically for 1000 different sets of adjoining pixels in water. The complex correlation ( $\rho$ ) for any given set of adjoining resolution cells is expressed as

$$\rho = \frac{E\{xy^*\}}{\sqrt{E\{|x|^2\}E\{|y|^2\}}} \quad (4.2)$$

where  $x$  and  $y$  are the vectors of phasors (complex) of two different, but adjoining, pixels in all SLC images, and  $\cdot^*$  here denotes the complex conjugate. If the observations of both are random, then the correlation coefficient is expected to be low, in the region of 0.3.

In section 3.2, the correlation between adjoining resolution cells in oversampled SLC images was theoretically 0.89 for azimuth, and 0.84 for range. The distribution of the empirically estimated complex correlation coefficient is shown in figure 4.9, for range, azimuth and diagonal. Here also the correlation with a pixel separation of one and nine are shown, to investigate the changes with increasing spatial distance between the observations. The empirically estimated complex correlation matches the theoretically estimated correlation, i.e., the center of the peaks of the distributions are equivalent (to within 0.1) to the theoretically determined values.

#### Temporal coherence

The temporal coherence is used as a quality measure to identify and select PS, and is used here to estimate the temporal coherence of resolution cells with random phases. The temporal coherence is estimated from the residual phases, thus after subtracting an estimation for the topography and deformation. The estimated temporal coherence for pixels with random phases should be very low, however, because the correlation between adjoining pixels is high the behavior of the temporal coherence should be analyzed as well. Furthermore, the empirically estimated temporal coherence with increasing spatial distance (decreasing correlation) gives information about its behavior for random phases.

---

<sup>2</sup>Diagonally separated resolution cells are two resolution cells separated both in azimuth and range by the same amount.

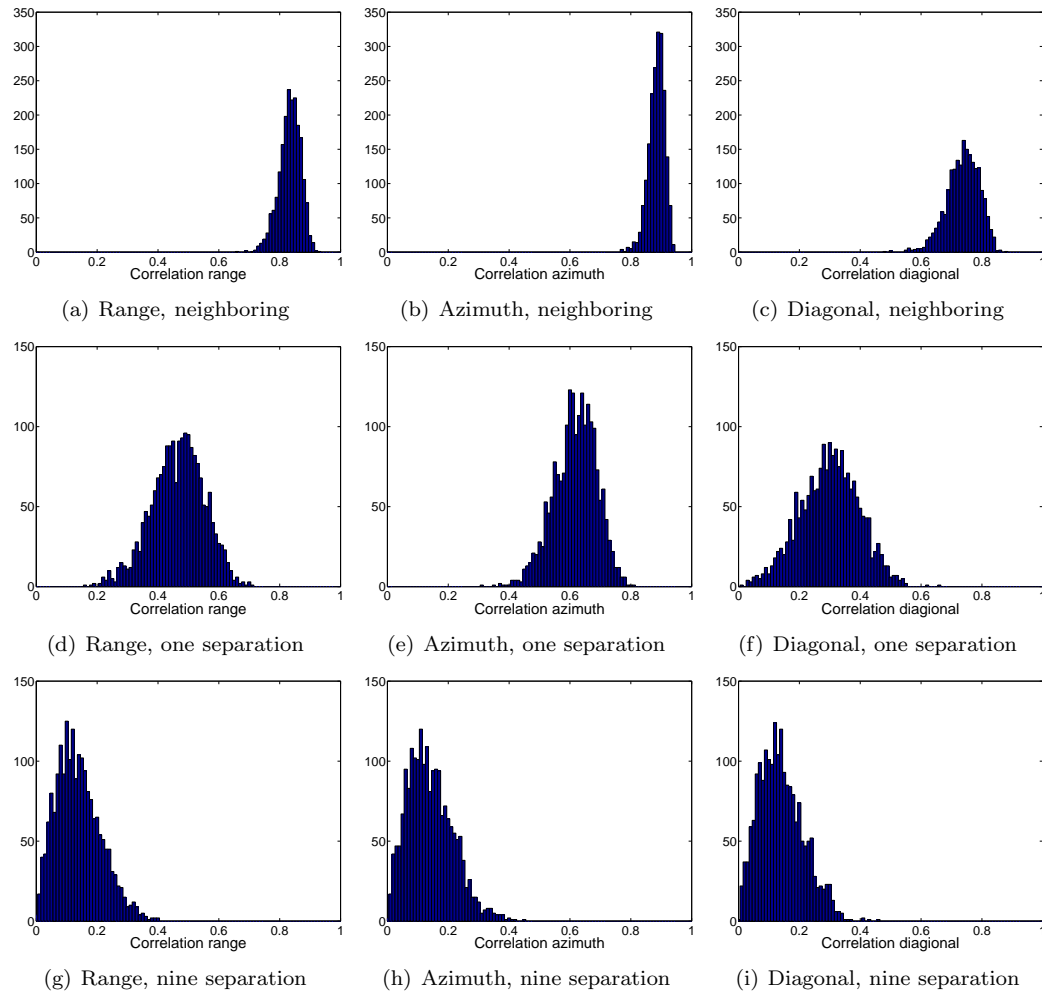


Figure 4.9: The empirically estimated correlation for 1000 pixel sets in water with a separation of zero, one, and nine in the three directions range, azimuth and diagonal. The correlation in azimuth is higher than in range, and in all directions the correlation decreases with increasing spatial separation of the pixel sets.

In figure 4.10 the distribution of the temporal coherence values are shown. In these figures it is clearly seen that the distribution of the temporal coherence values for range and azimuth are extremely high for zero separation, with temporal coherence values up to 0.95. The diagonally spaced resolution cells show a lower temporal coherence, which is expected because the overlap between these resolution cells is smaller. The consequence of the overlap of adjoining resolution cells results in a high temporal coherence, regardless of the signal contained within the measured phases. In other words, it is difficult to discriminate between random phases and PS, if for both types of scatterers the temporal coherence is within the same domain. The temporal coherence of any random residual phase will be a non-zero value, but this does not imply that there is correlation between the pixels. This estimation can be improved by using a larger dataset, in which more pixel sets can be used. The distribution of the temporal coherence values, gives information on the expected temporal coherence of random adjoining phases. When the

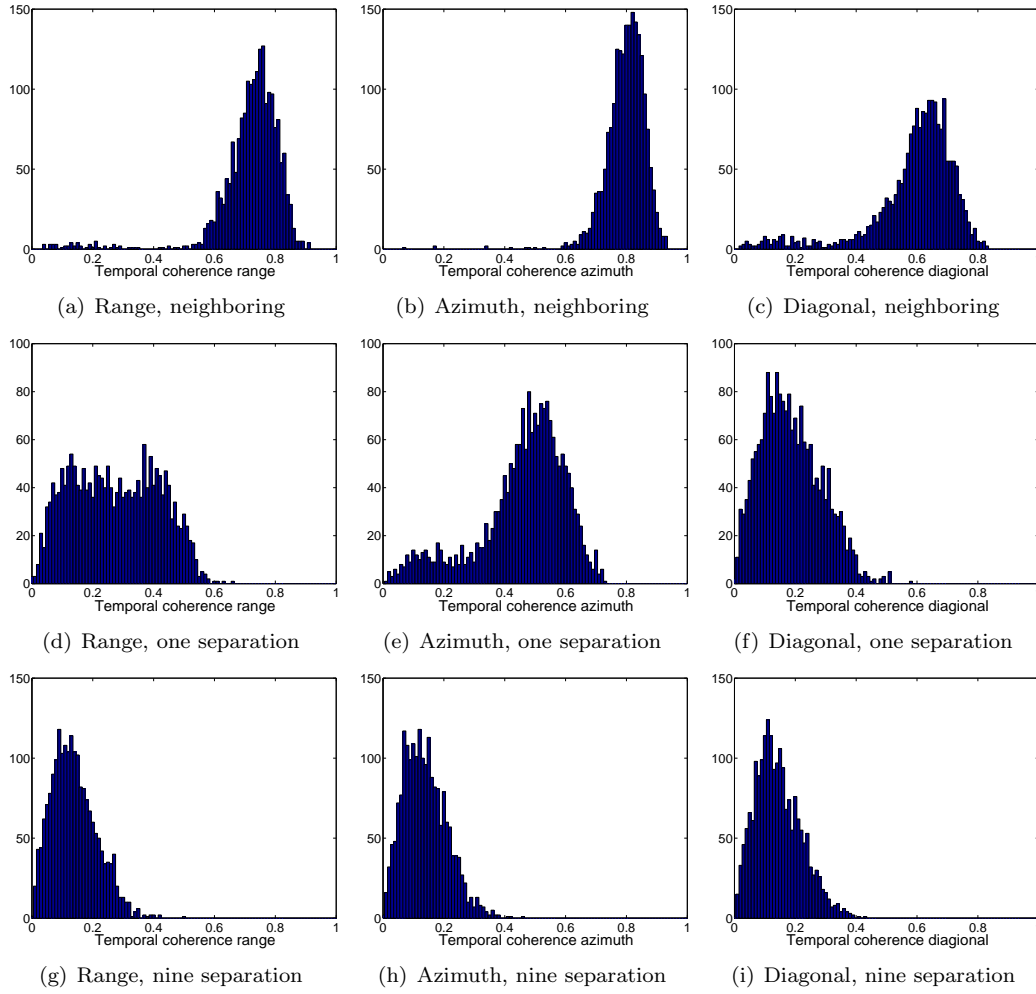


Figure 4.10: The empirically estimated temporal coherence for 1000 pixel sets in water with a separation of zero, one, and nine in the three directions range, azimuth and diagonal. The temporal coherence in azimuth is higher than in range, and in all directions the correlation decreases with increasing spatial separation of the pixel sets. For a separation of one pixel, the distributions in azimuth and range change.

distance between the resolution increases, then the temporal coherence reduces similarly as the correlation. A separation of nine, is expected to be completely uncorrelated and is an indication for the minimum temporal coherence that should be used in any processing technique.

### Topography

The parameters of interest (topography and deformation) are also influenced by the correlation between adjoining pixels. However, it is unclear what the behavior is of these parameters for adjoining pixels. In water, the topography between two resolution cells should be estimated close to zero (no relation to the perpendicular baseline), because the phases in water are completely random. By estimating the topography between adjoining pixels in water, the effect of the cor-

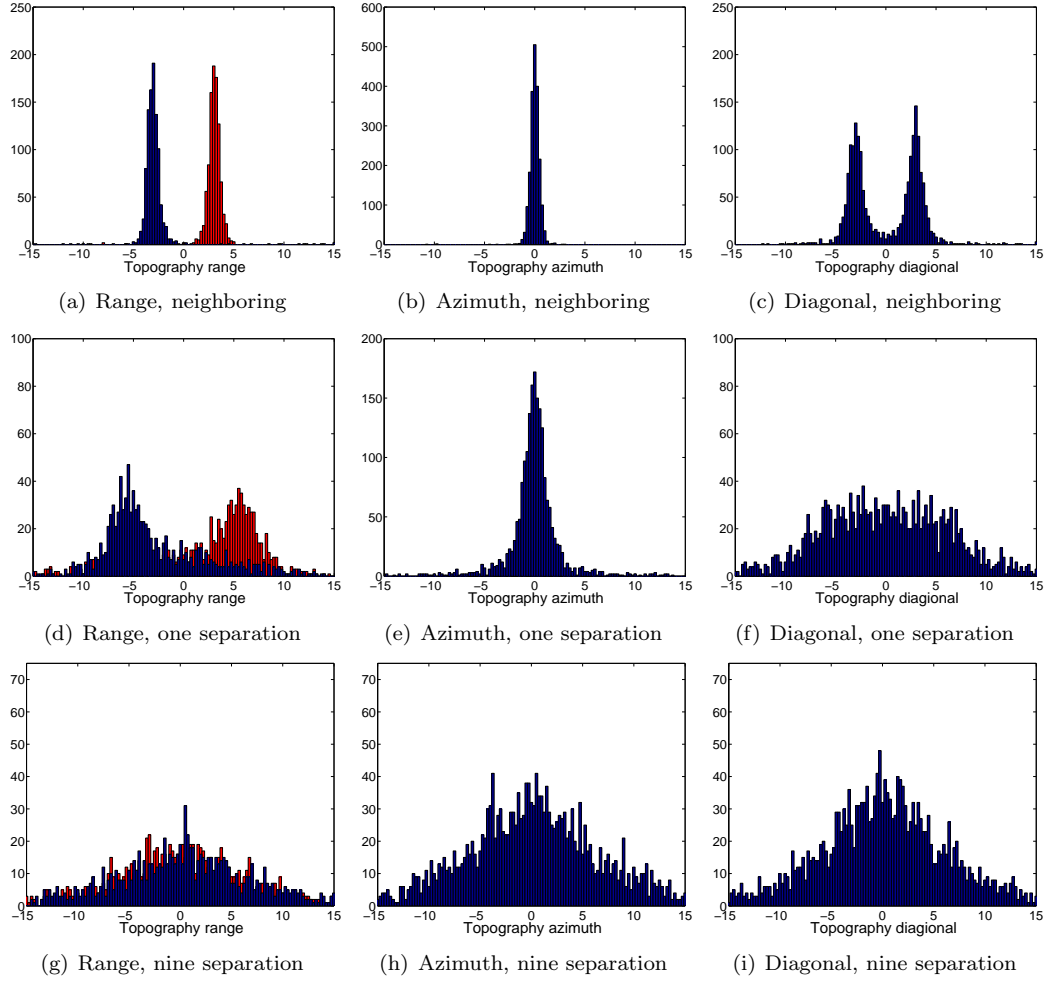


Figure 4.11: The estimated topography for 1000 pixel sets in water with a separation of zero, one, and nine in the three directions range, azimuth and diagonal. In range the topography shows two peaks, which are direction dependent, where red indicated the difference from far to near range, and blue from near to far range. A separation of nine pixels is enough to remove this effect, which seems to be related to the reference phase difference between these pixels.

relation can be identified.

Figure 4.11 shows the distribution of the topography. An interesting observation is the two peaks in the distribution for the topography in range direction. The two peaks are colored differently, which is related to the direction in which the topography is estimated. The blue color indicates topography from near to far range, and red indicates the other way around. The topography for adjoining pixels is thus related to the direction in which the topography is estimated.

The center of the peaks lies approximately at  $\pm 3$  meter, and with a separation distance of one this increases to approximately 6 meter. This can be related to the reference phase difference between these pixels, although the values do not match exactly. This is the same effect as a range

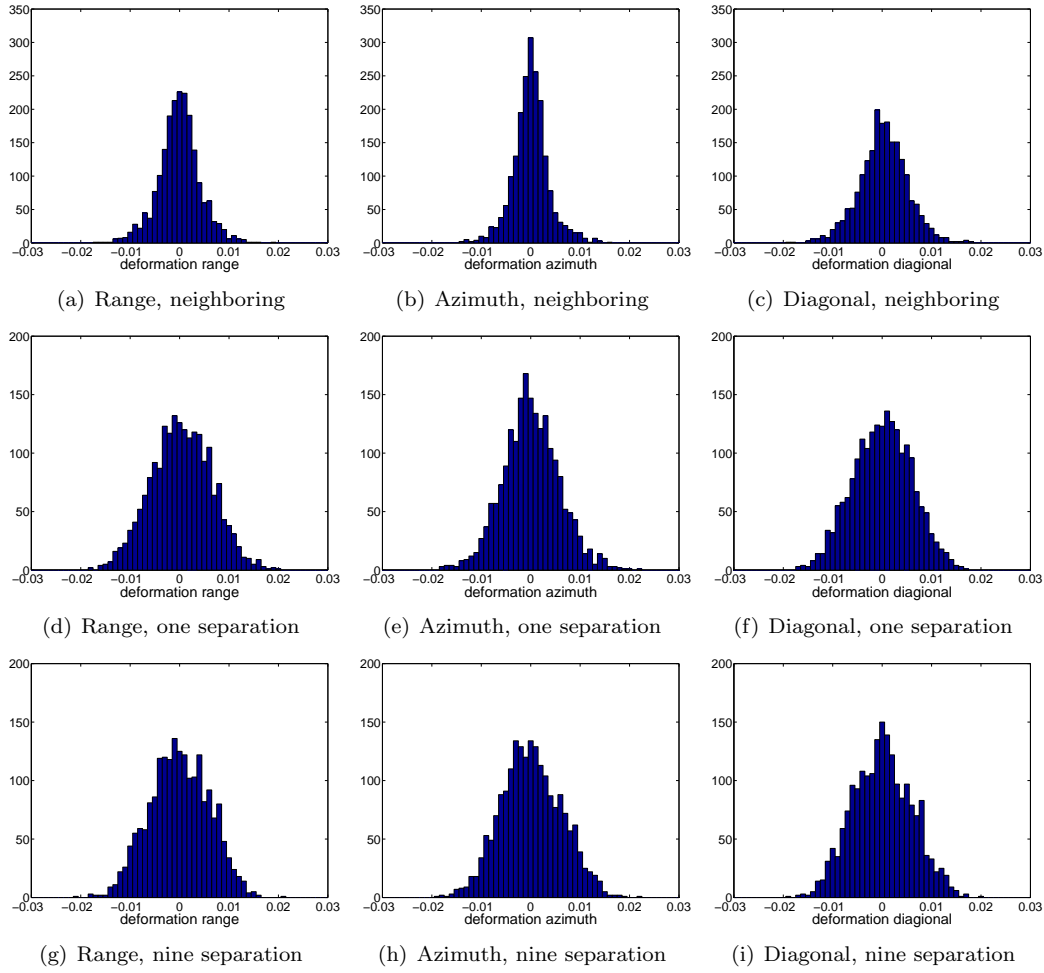


Figure 4.12: The estimated deformation for 1000 pixel sets in water with a separation of zero, one, and nine in the three directions range, azimuth and diagonal. The deformation distribution widens slightly with increasing spatial distance, which means that the effect of the correlation between adjoining pixels on the deformation parameter is only limited.

subpixel position within a resolution cell, extended to the slant range resolution of the system. The phase component related to the topography was described by equation 2.2, and the phase component due to a range subpixel position was described by equation 3.32. By combining these equations (and setting the (ground) range subpixel position equal to the ground range resolution), the ground range resolution is related to the topographic height

$$H = -\Delta r_{\text{gr}} \sin \theta_x \cos \theta_x. \quad (4.3)$$

Here  $\theta_x$  is the look angle with respect to the coordinates of pixel  $x$ . This can be easily related to the slant range resolution using equation 2.6

$$H = -\Delta r_{\text{sr}} \cos \theta_x. \quad (4.4)$$

In this case study oversampled Envisat data with a slant range resolution of approximately 3.85

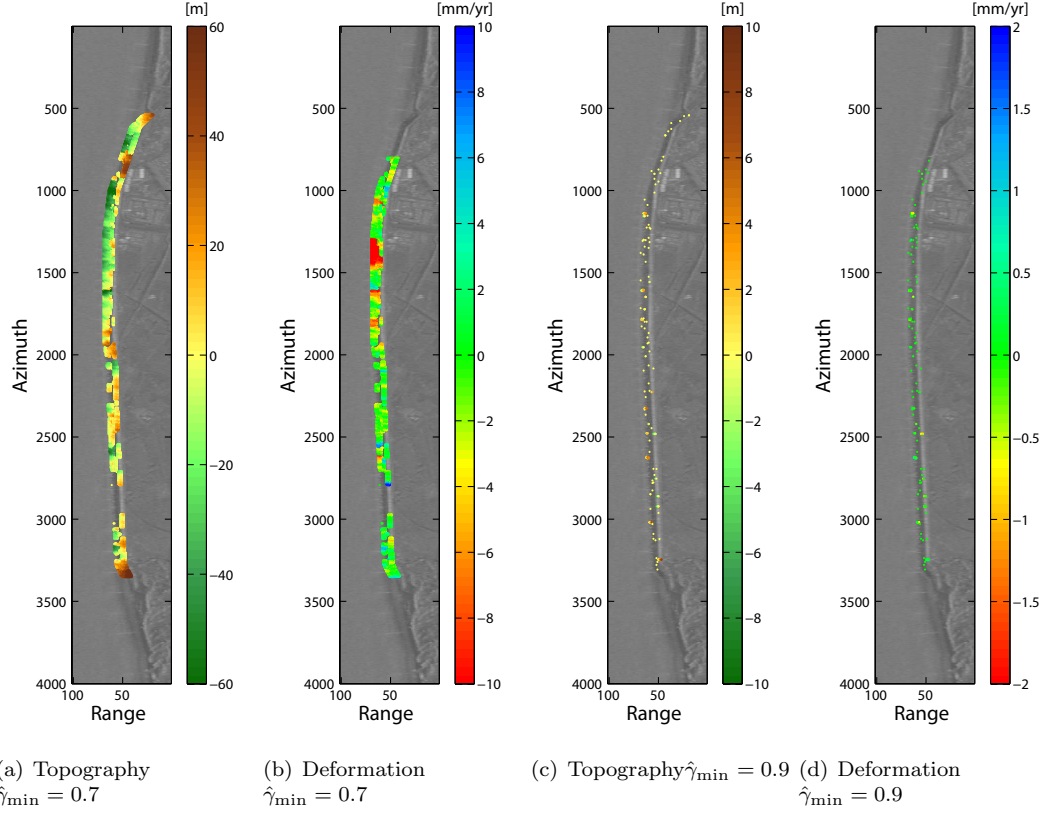


Figure 4.13: The topography and deformation results of processing only adjoining pixels, with the minimum coherence threshold increased to 0.9. The previous results are shown in (a) and (b), which was processed using different seed pixels, i.e., the area where no PS were identified with the lower threshold depends on the seed pixels. Not all identified PS have the same reference point, in other words there are regions that are not merged still present in the result.

meter is used. With a look angle of  $21^\circ$  (the WDS is located more in the far range of the image), the topographic height would then be approximately 3.6 meter. This is close to the 3.1 meter found in the estimated topography, but not exactly. The topography is, however, negative for increasing range, which is the same direction as the images show. The correlation between adjoining pixels is 0.84, if this would be incorporated into the expected value, then this would decrease to approximately 3 meter. This value is extremely close to the estimated mean empirical value, and is assumed to be the reason for the difference.

### Deformation

The other parameter of interest is the deformation. For pixels with random noise, the distribution should be approximately gaussian (random) with a zero mean. In figure 4.12, the distribution of the deformation is shown. The distributions do not show significant differences with increasing spatial separation. Also between range and azimuth the differences are minimal. When the spatial separation increases, the distribution becomes slightly wider and resembles a more gaussian distribution. The correlation therefore does affect the deformation. There is, unlike the topography, no directional dependency, and is therefore not visualized.



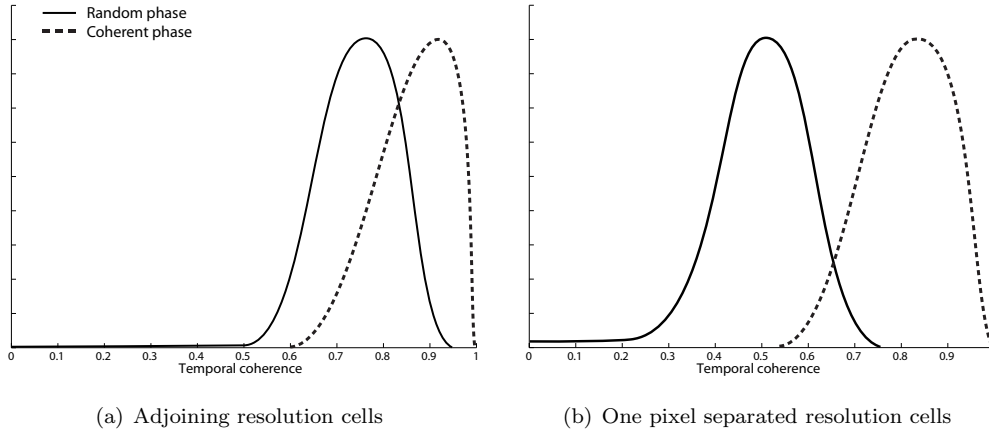


Figure 4.14: Illustration of the temporal coherence for incoherent and coherent phases. If adjoining pixels are used, the overlap in temporal coherence is very high, which makes it difficult to discriminate between incoherent and coherent phases. By incorporating a pixel spacing in the processing this overlap will reduce significantly.

#### 4.3.4 Increased coherence threshold

After the analysis of the adjoining pixels the minimum temporal coherence threshold was increased to minimize the number of falsely accepted PS. Based on figure 4.10, the minimum temporal coherence was increased to a value of 0.9, of which the results are shown in figure 4.13. The previous results are shown as well, in order to compare the results.

From this result no relevant information can be extracted, because each group of identified PS is referenced to a different reference PS. To improve this result the Nibbling method requires a significant reduction in the correlation between the estimation and expanding pixel. It is expected that the temporal coherence of PS and random phases overlap, illustrated in figure 4.14(a). In order to reduce this overlap either the correlation between the neighbors must be taken into account in the mathematical model, or the adjoining pixels must be omitted. Here it is chosen to omit the adjoining resolution cells, which also increases the amount of neighboring pixels to estimate.

#### 4.3.5 Concluding remarks

The main challenge with Nibbling on adjoining resolution cells is to account for the correlation, but still being able to discriminate between coherent and random targets. The overlap (figure 4.14(a)) with the increased minimum threshold causes many actual PS to be unidentified. Furthermore, not all pixels in the area of interest are actually PS, or coherent enough that the temporal coherence is extremely high. This causes the integration path's to stop after a few iterations when the minimum temporal coherence threshold is increased to 0.9.

The analysis of adjoining pixels with random phases gives knowledge about the effects and behavior of the parameters of interest and the quality measure, due to the correlation between adjoining pixels. Also the behavior of these parameters for increasing spatial separation is shown. Because the temporal coherence of adjoining pixels is always high, it is difficult to discriminate between

PS and random phases, which requires some alteration to the methodology of the Nibbling algorithm. Furthermore, the topography is directionally dependent for pixels with a small spatial separation. However, the effect on the deformation seems to be minimal.

## 4.4 Improving the Nibbling approach

From the analysis of adjoining resolution cells it was shown that the temporal coherence of two resolution cells with a separation distance of one resolution cell decreases significantly. The correlation will not be zero, as the scatterers in a resolution cell influence more neighboring resolution cells. Figures 4.10(d) to 4.10(f) show the distribution of the temporal coherence of neighboring resolution cells that are not adjoining. Here the term neighboring is still used, because of the small spatial distance between the resolution cells. Figure 4.14(b) illustrates how the temporal coherence distribution will overlap if a pixel separation is incorporated. It is expected that the temporal coherence of PS decreases only minimally, whereas the temporal coherence of incoherent pixels decreases significantly.

There are several reasons for applying a non-neighboring pixel approach to improve the result obtained by the neighboring pixel approach. Firstly the correlation reduces significantly when the arcs span distances of more than the adjoining one. Furthermore, if the WDS is not completely covered by coherent scatterers the result will be in patches of estimated PS which are not related to the same reference point. The probability of estimated PS to become relative with respect to each other increases when allowing arcs to span larger distances. When the PS are not referenced with respect to each other, the result can not be interpreted.

This section elaborates on results obtained by including a pixel separation, i.e., omitting only the adjoining resolution cells. Because of this, the assumption that no ambiguities will occur on neighboring pixels may not be valid. As is previously discussed in section 3.3.2, ambiguities can occur with topographic heights of as small as six meter. If larger separation distances will be applied, the topographic differences will become increasingly important. For neighboring pixels, the topographic differences are approximately 3 meter across the WDS. However, for topographic differences of 6 meter (1 pixel separation) or more, it is possible for ambiguities to occur at baselines larger than 400 meter, see section 3.3.1. Furthermore, the subpixel position in range also depends on the perpendicular baseline, which further decreases this minimum baseline. Therefore the ambiguity resolution step is now important in order to remove any ambiguities in the phase differences and consequently estimating the topography and the deformation correctly.

### 4.4.1 Results of improved Nibbling

The results of the improved technique are shown in figure 4.15. There is an increase in the number of identified PS, which is seen as a significant improvement. However, the result remains uninterpretable because the different patches are unreferenced (not connected) with respect to each other.

The main reason for the patches is the fact that not all resolution cells contain coherent phases, such that these are identified as PS. The approach therefore stops at a certain point (for each seed), because the residual phases do not meet the acceptance criterion. This can not be solved only by lowering the coherence threshold any more, because of the increasing number of falsely accepted pixels. Large spanning arcs could be incorporated (omit two or three adjoining pixels), but in this way the method starts to converge towards the conventional method. If this would

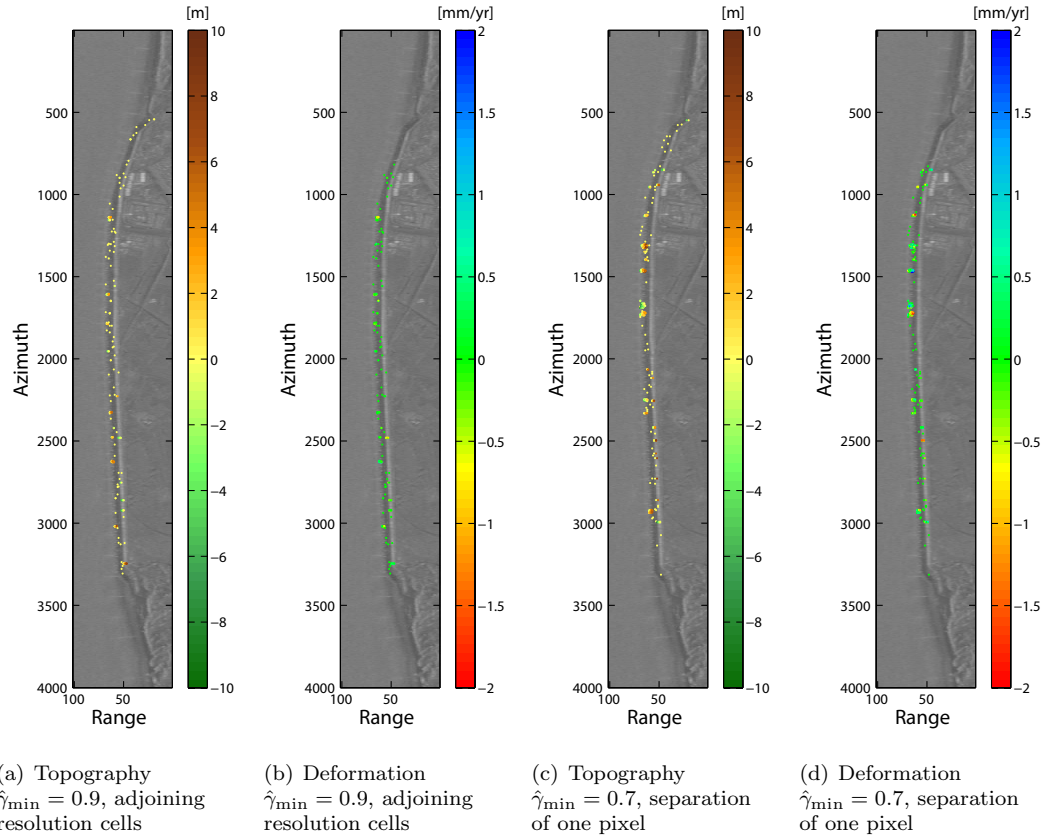


Figure 4.15: The results of Nibbling including a pixel separation of one in the estimation kernel. Figures (a) and (b) show the results of the adjoining pixel approach, to compare the results. Note that processing of both methods started with different seed pixels.

be applied, the correlation between resolution cells will decrease and the temporal coherence threshold could be chosen even lower. A coherence threshold below a certain value, will eventually lead to many falsely accepted PS.

## 4.5 Nibbling with increased kernel size

To further improve the result, such that it becomes interpretable, requires the estimation kernel to become larger. This increases the chance that PS nearby are found, because more pixels are estimated. However, with increasing arc length, the influences of atmosphere, deformation, and orbital errors can become significant.

### 4.5.1 Search area expansion

By enlarging the estimation kernel, the search area from a reference pixel is expanded which increases the probability of correctly identifying PS. Hence, the probability of referencing more patches of PS with respect to each other increases. A kernel which is too large, however, will increase the influence of different phase components, e.g., atmosphere, orbital errors, and defor-

mation. These components are spatially correlated, and therefore influence the double-difference phases over small distances minimally. An increasing influence of these components relates to an increasingly more complex estimation procedure, and the processing algorithm will converge towards the conventional method (DePSI).

An increasing contribution of the phase component related to the atmosphere only occurs if the arcs span distances of over 1 kilometer (Williams et al., 1998). Within this distance the atmosphere is expected only to contribute minimally to the total measured phase. This is the first limitation to the size of the estimation kernel. Secondly, the deformation is generally spatially correlated, although extremely local, spatially uncorrelated deformation can occur. In this case a spatial correlation of the deformation of 40 meter along the WDS is assumed, which limits the size of the estimation kernel even more. Finally the topography must be taken into account, which in this case is also spatially correlated. In the longitudinal direction of the WDS, the topography does not change much, but across the WDS it does. The topographic height between the base and the top of the WDS is approximately 15 meter, which is a spatial distance of approximately 80 meter, see figure 4.2.

The size of the estimation kernel is limited by the component with the smallest spatial correlation, which is the deformation. In azimuth the kernel size is set to 18 lines (36 meter). In range the kernel is smaller, because of the elongated shape of the resolution cells and the topography of the specific area. The size of the kernel in range direction is limited to 4 pixels (40 meter), to reduce influences of the topography across the WDS. This is not a general size which will work for any WDS, i.e., it is case dependent.

#### 4.5.2 Results with increased kernel size

The increased size of the kernel leads to an interpretable result, because the patches are merged to a single patch with only one reference point. Some pixels, often those that are initially not PS, are filtered out by only selecting the pixels of the largest region. The minimum coherence threshold is set to 0.7, to decrease the probability of falsely accepting PS. Because the result has a common reference point, an indication of the quality of the result can be made. Here it is assumed that the result from DePSI is correct, and both methods are referenced to the same resolution cell, a point on the WDS that has a high estimated temporal coherence with DePSI.

The result from DePSI is now only shown for those pixels within the area of interest. This is done in order to compare the results of both methods within this area. The amount of identified PS has increased using the Nibbling approach, however, this does not imply that qualitatively good information is gathered from these resolution cells. With DePSI 5285 PS are identified, whereas with Nibbling 16840 PS are identified. This is more than triple the number of points, but a more extensive analysis of the results is required to validate the quality of the information from these PS.

#### 4.5.3 Topography

Figure 4.16 shows the resulting topography of the WDS both with DePSI, and Nibbling with increased kernel size. The standard deviation of the topography for Nibbling is approximately 12.7 m, whereas for DePSI it is only 2.3 m. This shows that approximately six times more variation is present in the topography of Nibbling. Interestingly enough, the topography does increase towards the crown of the WDS, but the increase in topography is much larger than

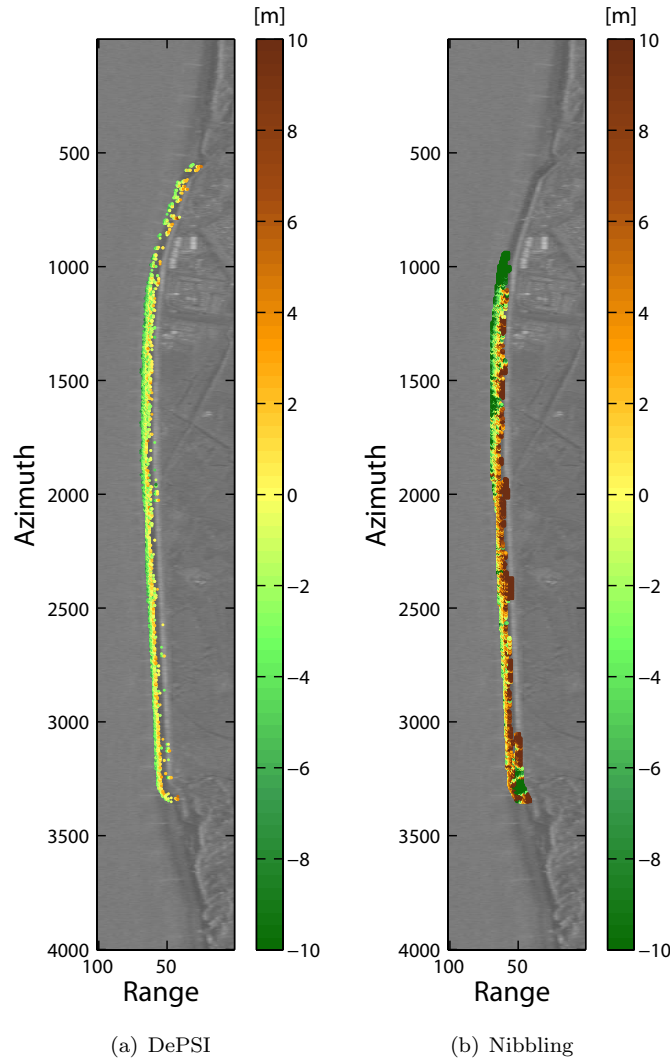


Figure 4.16: The resulting topography of DePSI and Nibbling with increased kernel size. The topography in both cases increases towards the crown of the WDS, but the variation of the Nibbling approach is much larger.

the actual increase of the WDS. The information received by using DePSI is much closer to the actual topography.

The histograms of the topography of both methods are shown in figure 4.17. This shows that there are identified PS which have a topographic height of over  $\pm 50$  meter, which is obviously incorrect. This could be caused by an extreme case of a misestimated topographic component, but could also be a cumulative error caused by a number of smaller misestimation. Another interesting point here is that a small peak is showing at  $-30$  meter, which leads to believe that two regions were merged together with an offset. However, it is difficult to analyse the result only from the distributions, therefore the resulting topography of both methods are shown with

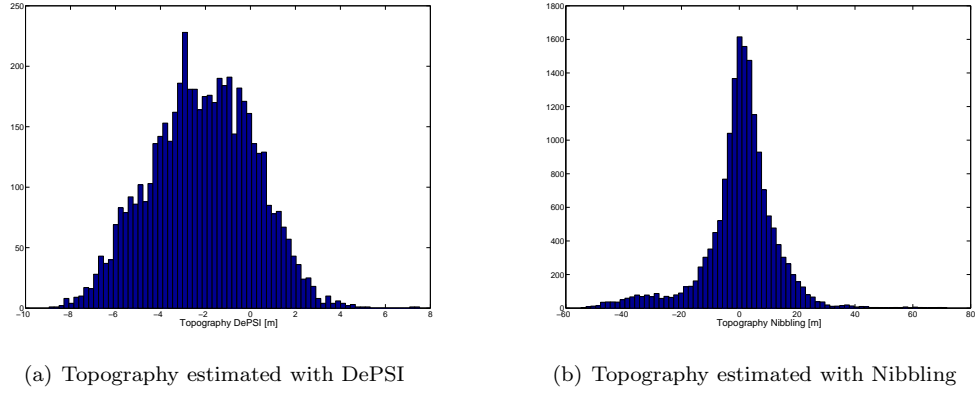


Figure 4.17: The histograms of the topography distribution of DePSI and Nibbling with increased kernel size.

respect to each other.

The resulting topography acquired using conventional PSI and the Nibbling approach are plotted with respect to each other in figure 4.18. The dashed line in this figure indicates a perfect correlation between both methods. A small variation of both methods is expected, however, the scale of the Nibbling approach is six times larger than DePSI in order to visualize the result better. The largest part of the point cloud is above the dashed line, which is an offset and can be corrected for. On close inspection it seems that a second point cloud is below the main cloud, which is offset differently. These offsets could be caused by an incorrect merging of two regions, but possibly could also be a misestimation between two regions. Finally in this figure, the peak at  $-30$  m (see figure 4.17(b)), is barely visible as three small clouds, uncorrelated to DePSI. The reason for these clouds is unclear. A possible hypothesis is that the unwrapping procedure finds a wrong solution, such that the residuals of a noisy pixel (not a coherent point) are accepted.

#### 4.5.4 Deformation

The deformation is both estimated functionally and stochastically using the mathematical model described in section 3.4. Both these deformation estimations, together with the deformation estimated with DePSI are shown in figure 4.19. The first observation of these results is the difference between the estimated deformation using a stochastic model and a functional model. It seems that the functional model estimates the deformation better than the stochastic model, because the trend from north to south is very well visible with the functional estimation. However, the scale of the magnitudes with Nibbling is again larger than DePSI. The standard deviation for the Nibbling approach using the functional estimation of the deformation is approximately 6.51 mm, for the stochastically estimated deformation it is 2.39 mm, and for DePSI it is only 1.05 mm. The variation, even in the stochastically modeled deformation, is larger than that of DePSI.

Similarly to the topography, again the histograms of the deformation estimations are shown in figure 4.20. In the histogram of DePSI, two distinct peaks in the mean peak can be distinguished. The histogram of the functionally modeled deformation shows three peaks, with a large distribution between  $\pm 3$  cm per year. The stochastically estimated deformation shows a smaller variance, with mean of zero.

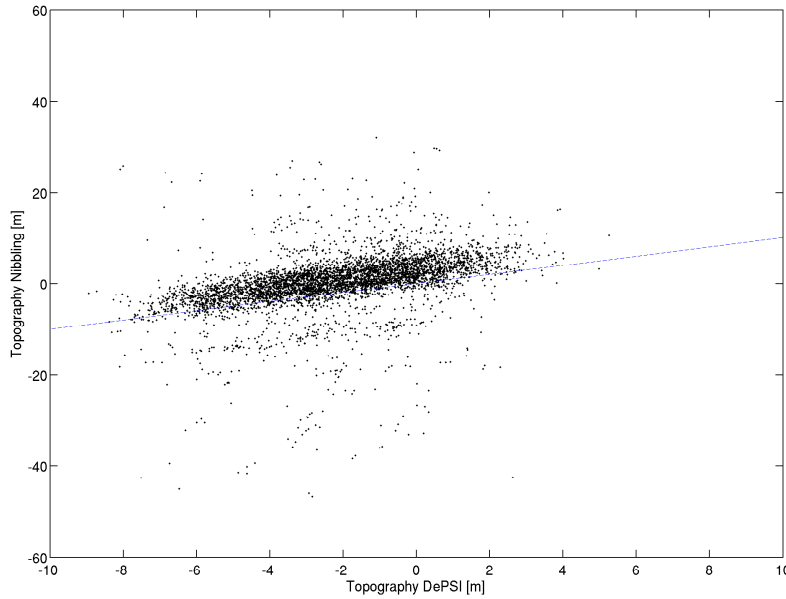


Figure 4.18: Topography of DePSI and Nibbling with respect to each other, indicating the correlation of the two methods. The dashed line indicates perfect correlation. Three small clouds can just be distinguished between  $-20$  and  $-40$  meter topography for Nibbling which produces the small peak in the distribution of figure 4.17(b). Also below the main cloud, a second smaller cloud can be distinguished, which does show correlation. For visualization purposes the axis are not set equal.

More information about the differences can be extracted by relating the two methods with respect to each other, which is shown in figure 4.21. Here the deformation obtained with DePSI is plotted with respect to the stochastic and functional deformation, where the dashed line again indicates perfect correlation. For the stochastically modeled deformation there exists only one cloud, but the correlation between these methods is extremely low (0.02). The correlation between the functionally estimated linear deformation rate is much higher (0.55). However, the functionally estimated deformation shows multiple clouds, which are probably caused by ambiguity or merging (implementation) errors. Because both methods still show significant differences with respect to the deformation from DePSI, it cannot be concluded that the stochastic modeling of the deformation is incorrect. On the contrary, It is proven in section 4.3, that the stochastic model is able to determine the deformation within sub-mm precision.

## 4.6 Methodological differences

The differences between the methods can be caused by propagation of random noise, atmosphere, orbital errors, errors in ambiguity resolution (unwrapping errors), implementation, or conceptual errors. Random noise can cause errors in the estimations, which may propagate through the estimations because these are done sequentially in Nibbling, which is different with respect to DePSI. Atmosphere and orbital errors are currently expected to cancel out mostly with short arcs in Nibbling, whereas in DePSI these are modeled and removed. Ambiguities can cause mis-

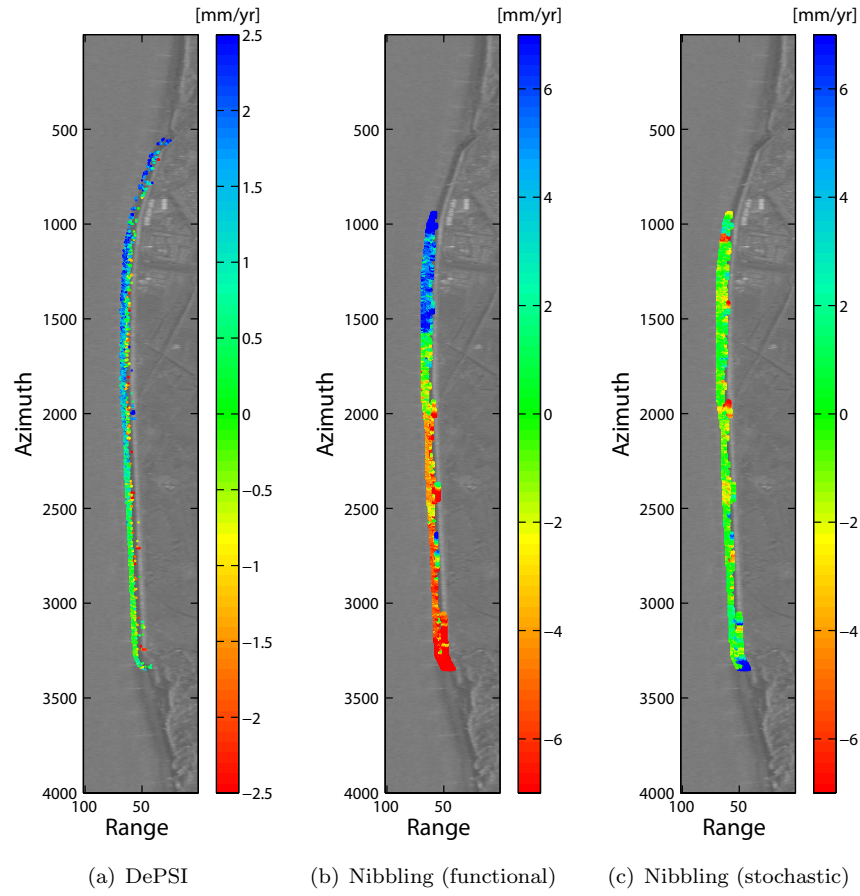


Figure 4.19: The resulting deformation of DePSI and Nibbling (functionally and stochastically modeled) with increased kernel size. The topography in both cases increases towards the crown of the WDS, but the variation of the Nibbling approach is much larger.

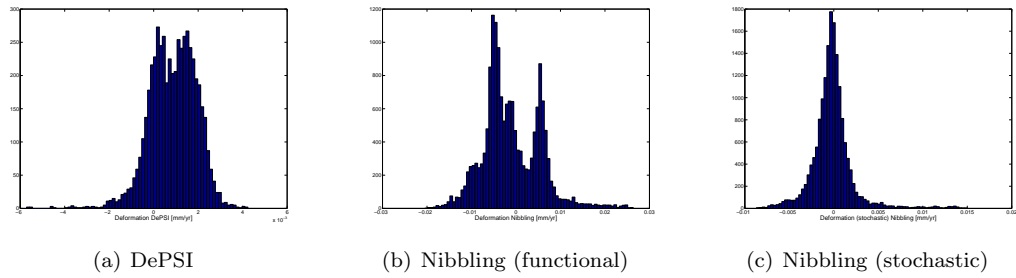


Figure 4.20: The histograms of the deformation distribution of DePSI and Nibbling with increased kernel size.

estimation of the topography which can propagate to the deformation. Finally implementation or conceptual errors of initially unknown challenges within adjoining pixel processing, could be the cause for mis-estimation in both topography and deformation.



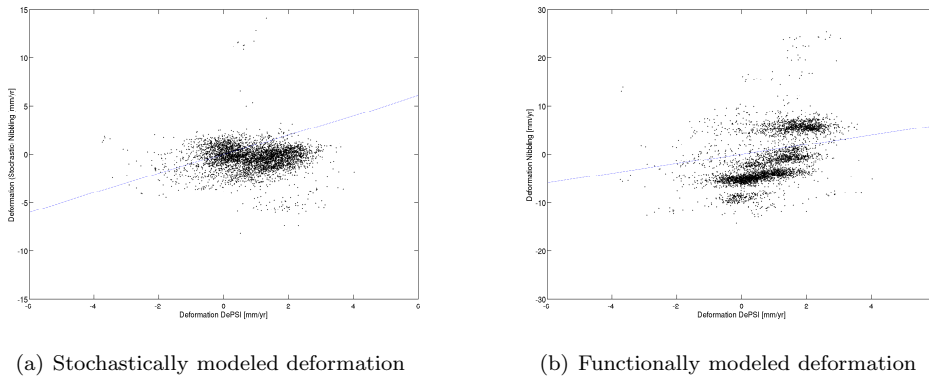


Figure 4.21: Deformation of Nibbling (stochastically and functionally determined) with respect to the deformation acquired by conventional processing. The correlation of the stochastically modeled deformation seems uncorrelated with respect to DePSI. The functionally estimated deformation does show correlation for each cloud separately. For visualization purposes, the axis are not equally scaled.

#### 4.6.1 Random noise

Thermal noise and processing inaccuracies contribute to the random phase component, or random noise. It is a component with a normal distribution and an expected mean of zero. Thermal noise influences the phase of the interferogram and can be derived theoretically by determining the signal-to-noise ratio (SNR) of a system (Zebker et al., 1994; Zebker, 1996; Hanssen, 2001). The processing step to resample the slave (in order to coregister it to the master later) also causes a random phase component, because of interpolation errors.

Random noise is normally distributed and is stochastically modeled, will propagate in the estimated parameters (topography and deformation). A random phase component is different for each pixel, and assumed to be uncorrelated, especially when a pixel separation is incorporated in the processing. Because double differences are used, this term cancels out irrespective of the route from one pixel to another. However, in every estimation of the differences of the parameters between these pixels, a small error is made because of the noise. The noise is expected to be distributed normally, therefore it is expected to be zero when including a large enough stack of interferograms.

Because the noise is modeled stochastically and its distribution is gaussian, it is not expected that this component causes large differences between the methods. Furthermore, the noise components in DePSI are also stochastically modeled. However, in DePSI VCE is performed, which improves the estimation of the noise for PS.

#### 4.6.2 Atmosphere and orbital errors

Atmosphere and orbital errors are currently unmodeled in the Nibbling approach. The contribution of these components is expected to be very limited, because of the temporal decorrelation regarding time sampling of the radar acquisitions, and their spatial correlation. With a large stack of radar images, the atmosphere should be averaged out in the estimated parameters of interest, similar to the random noise. Furthermore, it is independent of perpendicular baseline and should therefore not influence the estimation of the topography.

The resulting deformation is a superposition of the atmosphere and the deformation, therefore the actual deformation can be obscured to some extent. In order to identify if this is the source for the misestimation of the deformation, an analysis should be performed that investigates the contribution of the atmosphere to the deformation time series. This can be achieved by using DePSI to estimate the phase components of the atmosphere and subtracting this from the original phases. The new phases are then accounted for the atmosphere, which reduces this error source significantly. The result of processing with the atmosphere corrected phase observations will show the influence of atmosphere in the Nibbling approach. This research is based on the assumption that the atmosphere does not have to be modeled due to its spatial correlation. It is for this reason not within the scope of this research and is therefore recommended for future research.

### 4.6.3 Ambiguities

Although the ambiguities of the neighboring phases are estimated, it does not imply that all ambiguities are resolved correctly. An ambiguity at a certain epoch will cause an error in the estimation of the topography. This error can be very small, and consequently the estimated temporal coherence can be accepted. In this case the error causes an offset in the estimations relative to this, falsely assumed correct, topography. If this occurs, it will be seen as offsets from the main point cloud if the Nibbling approach and DePSI are plotted against each other.

Small (previously assumed insignificant) errors in a sequential procedure can build up to significant errors over longer integration paths. In the case that this error occurs when merging two regions, the (absolute) difference between those two regions is incorrect, which would result in a point-cloud with an offset. This is also seen in figure 4.21, although the variation of the point clouds is also very large.

### 4.6.4 Sidelobe observations

The PS on the Hondsbossche zeewering are assumed to be coherent distributed scatterers. If this assumption is incorrect, and the PS on the WDS are mostly coherent (dominant) point scatterers, then this introduces errors in the height estimation. A point scatterer spatially characterizes itself as a sinc function (Cumming and Wong, 2005). This pattern causes sidelobes in the radar image in both range and azimuth.

The strength of a scatterer determines the significance of the sidelobes. These sidelobes affect the phase of the adjoining pixels, and consequently the height estimation. The phase at each sidelobe is equal to the phase of the point target observation, and the interleaved sidelobes are shifted with  $\pi$ . Therefore, observations of the pixels neighboring a point scatterer are the same observation of that point scatterer. This results in a perfect correlation between these observations, if the strength of the sidelobe dominates the phase of the scatterer in the neighboring resolution cell. Hence, these neighboring observations are not independent, and no new information is added (Ketelaar, 2008).

In range this phase shift causes a linear decrease in the estimated topography from near to far range. Due to the flat Earth reference phase the estimation of the topography of a sidelobe's height, changes the geographic location of the PS (sidelobe measurement), such that it partially cancels with its range position. In azimuth there is no effect in topography, because all ob-

servations are approximately at equal range. These sidelobes will therefore be given the same reference phase value as the actual target. The deformation (velocity) is not influenced by the sidelobes (Ketelaar, 2008).

In case of the Hondsbossche zeewering, a strong trend towards the crown of the WDS is found, seemingly much steeper than the actual slope of the WDS. Along the dike the topography remains relatively constant. This is in accordance with the expected increasing height due to sidelobe observations, which can introduce topographic difference of approximately 30 meters within eight range samples (oversampled data). It is therefore recommended to further investigate the influence of sidelobes and methods to remove or reduce this effect.

#### 4.6.5 Implementation and conceptual errors

Any designed algorithm can be flawed due to incorrect or inefficient implementation of the described method. These implementation errors can cause any kind of differences in the final results with respect to DePSI. The implementation of the estimation procedure is expected to be correct, because the same deformation is estimated for both DePSI and Nibbling, to prove the concept (see section 4.3.1). The implementation of pixel tracking (flagging) or merging can lead to erroneous results, which are then described as implementation errors.

On the other hand, conceptual errors can be the cause for differences in the results of both methods. Before the method was implemented, the behavior of adjoining pixels was not well understood. The correlation of adjoining pixels is extremely high, which results in two measurements not being independent. The concept furthermore requires that there are no sidelobe observations, which make adjoining resolution cells completely dependent. After the analysis of adjoining resolution cells, it seems that the concept of adjoining pixel processing is challenging due to the correlation. For this reason the Nibbling algorithm was altered to incorporate a larger estimation kernel, which can be seen as a conceptual change.



## Chapter 5

# Conclusions and Recommendations

There are many challenges involved in developing a processing algorithm for adjoining pixels. Important conclusions regarding the processing setup as developed during this research can be drawn. This chapter will discuss the research question and the subquestions posed in the introduction, section 1.2. Next to the conclusions of this research, recommendations for future research are stated.

Initially this research started from the research question;

*Is there valuable information to be retrieved from line-infrastructure where no PS are found using conventional tools for PSI, by incorporating small arcs?*

And was divided in the following sub questions;

1. Are the pixels on a WDS that are not identified as PS using conventional PSI processing coherent enough that information regarding the deformation can be evaluated reliably in terms of ensemble coherence or a posteriori variance?
2. What is the consequence of a adjoining/neighbor pixel processing technique on the estimations of the topography, deformation, and the reliability measure?
3. Does incorporating small arcs, i.e., the double difference between neighboring pixels, imply that the phase differences are within the same phase cycle?

### 5.1 Conclusions

The concept of using adjoining pixels proved to be more complicated than initially anticipated, due to the correlation of the adjoining pixels. How the correlation affects the parameters of interest was not well understood. Improving the approach by omitting the adjoining pixels and enlarging the estimation kernel (a correlation reduction method), still did not yield a reliable result. Based on the analysis performed, with the given assumptions and implementation of the approach, no valuable information was retrieved.

Conventional methods for PS (DePSI), use a temporal coherence threshold to identify PS within an area. This threshold is also used to filter the data within the area of interest, where in conventional processing all pixels are estimated and none are removed. Depending on the value of this threshold, more or less PS are identified, but consequently the quality is decreasing or increasing respectively. The proposed method should improve the number of identified PS without decreasing the quality, but this is currently not the case. The quality measure, the temporal coherence, is high for adjoining pixels, regardless of the signal in the backscatter, see section 4.3.3. This renders the temporal coherence as a quality measure useless in an adjoining pixel processing approach.

The main consequence of adjoining pixel processing is thus the influence of the adjoining pixels to each other, because of the overlap (especially for oversampled data) and the weighting of the frequency spectrum. This correlation also affects the parameters of interest, such that the estimations do not represent the actual values. For this reason an improvement is made to the Nibbling approach where the adjoining pixels are omitted, and a coherence threshold is taken based on the empirical analysis of adjoining pixels in water (assumed random phases). With the increased estimation kernel based on the spatial correlation of the components (see section 4.5) an interpretable result is generated, but the result shows large differences with respect to conventional processing (the result is unreliable).

The double difference phases are assumed to be within the same phase cycle (no ambiguities), but this highly depends on the area. Slopes that increase with a ratio of 3:1 (distance to height), can induce ambiguity cycles for adjoining resolution cells, neglecting any deformation, atmosphere, orbital errors, and noise. If these terms are included in the double difference, it is possible that an increase as small as three meters can cause ambiguities. It is therefore incorrect to assume a priori that there are no ambiguities for adjoining pixels. In the case of short arcs (no more than several pixels long) the spatially correlated components will cancel out mostly, whereas the components dependent on the perpendicular baseline will not. In this is the case, then the ambiguities can be resolved by the new methods ambiguity resolution, as described in section 3.3.2.

The research performed on adjoining pixels provided valuable information on the behavior of the parameters of interest and the quality measure. It shows that an adjoining pixel approach is conceptually flawed if this correlation is not taken into account. It was not expected that the correlation would influence the adjoining pixels in such a way, and was therefore not taken into account in the mathematical framework. To account for it in the mathematical model the values for the covariance are required, which is challenging if the variances are not well known. For this reason the adjoining pixels were omitted.

## 5.2 Recommendations

The conclusions are based on the challenges that occur with adjoining pixel processing, and the potential of the approach. To improve and further develop the approach, the following recommendations are made, taking into account the conclusions and results from this research.

The recommendations for the development of the technique are summarized:

- The spatial correlation of neighboring and non-neighboring pixels can be taken into account within the stochastic model.

This correlation is currently not introduced into the mathematical model, but can improve the stochastic model and consequently the final result of the technique. However, the correlation between the pixels is not strictly constant, especially in the case of sidelobes, where the correlation can become very high. More research and a different implementation of the estimation procedure to account for this correlation. A covariance model with an assumed correlation may be used to calculate the temporal coherence for adjoining resolution cells.

- Develop or use an existing atmosphere filter to reduce this signal in the observations.

Filtering the atmosphere reduces error build-up over the long integration paths, and consequently improves the estimation procedure. The atmosphere should only contain a spatially correlated signal, and not the temporally correlated signal. The improvements of currently developed atmosphere filtering techniques can be tested, with respect to results without this filter.

- Use the algorithm as a complementary technique to improve current results of conventional PSI.

Instead of a stand-alone approach, it can be convenient to use Nibbling as a complementary technique to improve results from conventional PSI. These results are referenced to a single reference, which implies that the estimations to neighboring or non-neighboring pixels with Nibbling are also referenced to the same reference. This also reduces any propagating errors, because more tests with respect to other (assumed correct) estimated PS can be performed.

- Include different interferometric combinations, e.g., Small Baseline Subset (SBAS) analysis.

By minimizing the temporal or perpendicular baseline, the phase components that are related to those baselines are minimized. For instance by minimizing the perpendicular baseline, the sensitivity of the topography reduces and therefore less ambiguities are expected. Furthermore, in case of distributed coherent scatterers, the geometrical decorrelation reduces. However, this baseline approach reduces the distribution of perpendicular baselines and therefore the accuracy to determine the topography. By minimizing the temporal baseline, on the other hand, the phase components, and therefore the signal of the deformation, will be minimized, reducing the accuracy of deformation determination. The use of different interferometric combinations can prove to be very effective in improving the method described in this thesis, but will require adjustments to the mathematical model.

Other recommendations on the validation of the technique are:

- Validate the deformation timeseries on the corner reflectors in delft.

The corner reflectors in delft were leveled over the past five years (Marinkovic et al., 2008). There is an extensive time series available, which can be used to validate the stochastic deformation model and its sensitivity. The stochastic model can be based on the leveling

timeseries, where the sensitivity of a change in the stochastic model can be estimated empirically. The separation between the reflectors is small, and with a-priori knowledge on the deformation and topography, it is assumed that there are no ambiguities in the phase differences between two reflectors. Furthermore, a detailed time-series analysis can be performed on the sidelobes, to research the behavior of Nibbling on those highly correlated pixels, with respect to the empirical tests discussed in section 4.3.3.

- Validate Nibbling along a path of which the deformation is acquired using a different technique, e.g., leveling.

In the Groningen area, for example, many roads are leveled and deformation timeseries are currently available (Ketelaar, 2008). Along such a path the algorithm can be validated to see if the deformation shows the same behavior as the leveling data. The scattering mechanism on such roads, because it is also asphalt concrete, is assumed to be similar as to that on the WDS, which makes this an appropriate validation method.

A final recommendation is based on the dataset itself:

- Use a different subset of the data to acquire other information on the deformation of the Hondsbossche zeewering.

During the period of 2004 and 2005, the reinforcements were placed and the hydrocarbon production near Groet was stopped. It could be very interesting to process the data of 2006 up to present, which should include approximately 25 images (enough for PSI). The reinforcements are likely to be very coherent, and dominant scatterers (see figure 4.2, picture 2). The deformation timeseries could lead to conclusions of the settling and subsiding of the crown of the WDS.



# Bibliography

- Adam, N., B. M. Kampes, and M. Eineder (2004). The development of a scientific persistent scatterer system: Modifications for mixed ERS/ENVISAT time series. In *ENVISAT & ERS Symposium, Salzburg, Austria, 6–10 September, 2004*, pp. 9.
- Amelung, F., S. Jónsson, H. Zebker, and P. Segall (2000, October-26). Widespread uplift and trap door faulting on Galápagos volcanoes observed with radar interferometry. *Nature* 407(6807), 993–996.
- Bamler, R. and P. Hartl (1998). Synthetic aperture radar interferometry. *Inverse Problems* 14, R1–R54.
- Barends, F. (2008a). *Bodemdalingsanalyse bij dijkverzwaring*, Chapter 4.4. In Barends et al. Barends et al. (2008).
- Barends, F. (2008b). *Modellering van lokale relatieve zeespiegelrijzing*, Chapter 4.3. In Barends et al. Barends et al. (2008).
- Barends, F., D. Dillingh, K. van Onselen, and R. Hanssen (Eds.) (2008). *Bodemdaling langs de Nederlandse kust*. IOS Press.
- Berardino, P., G. Fornaro, R. Lanari, and E. Sansosti (2002). A new algorithm for surface deformation monitoring based on small baseline differential SAR interferograms. *IEEE Transactions on Geoscience and Remote Sensing* 40(11), 2375–2383.
- Born, M., E. Wolf, and A. B. Bhatia (1959). *Principle of optics; electromagnetic theory of propagation, interference and diffraction of light*. New York: Pergamon Press.
- Bovenga, F. (2005, October). *Multitemporal SAR interferometry and applications to slope instability monitoring*. Ph. D. thesis, Università Degli Studi Di Bari.
- CIA (2008). Central Intelligence Agency. <<https://www.cia.gov/library/publications/the-world-factbook/geos/nl.html>> Accessed October 2008.
- Colesanti, C., A. Ferretti, R. Locatelli, and G. Savio (2003). Multi-platform permanent scatterers analysis: first results. In *Second GRSS/ISPRS Joint Workshop on “Data Fusion and Remote Sensing over Urban Areas”, Berlin, Germany, 22–23 May, 2003*, pp. 52–56.
- Counselman, C. C. and S. A. Gourevitch (1981). Miniature interferometer terminals for earth surveying: ambiguity and multipath with the Global Positioning System. *IEEE Transactions on Geoscience and Remote Sensing* 19(4), 244–252.
- CSA (2008). Canadian Space Agency. <<http://www.space.gc.ca/>> Accessed October 2008.

- Cumming, I. and F. Wong (2005). *Digital Processing Of Synthetic Aperture Radar Data: Algorithms And Implementation*. New York: Artech House Publishers. ISBN 1580530583.
- Curlander, J. C. and R. N. McDonough (1991). *Synthetic aperture radar: systems and signal processing*. New York: John Wiley & Sons, Inc.
- Dentz, F., L. van Halderen, B. Possel, S. Esfahany, C. Slobbe, and T. Wortel (2006). ‘poseidon’: On the potential of satellite radar interferometry for monitoring dikes of the netherlands. Technical report, Delft Institute of Earth Observation and Space Systems, TU Delft.
- DLR (2008). Deutschen Zentrums für Luft- und Raumfahrt (German space agency). <<http://www.dlr.de/en/>> Accessed October 2008.
- Elachi, C. (1988). *Spaceborne radar remote sensing: applications and techniques*. New York: Institute of Electrical and Electronics Engineers.
- ESA (2008). European Space Agency. <<http://www.esa.int/>> Accessed October 2008.
- Esfahany, S. (2008). Improving persistent scatterer interferometry results for deformation monitoring. Master’s thesis, Delft University of Technology.
- Esfahany, S. S., F. J. van Leijen, P. Marinkovic, G. Ketelaar, and R. F. Hanssen (2008). Lessons learned from PSIC4: Improving PSI results for a constrained test site. In *Fifth International Workshop on ERS/Envisat SAR Interferometry, ‘FRINGE07’, Frascati, Italy, 26 Nov-30 Nov 2007*, pp. 7 pp.
- Ferretti, A., A. Monti-Guarnieri, C. Prati, and F. Rocca (Eds.) (2007). Esa publications.
- Ferretti, A., C. Prati, and F. Rocca (2000a, September). Nonlinear subsidence rate estimation using permanent scatterers in differential SAR interferometry. *IEEE Transactions on Geoscience and Remote Sensing* 38(5), 2202–2212.
- Ferretti, A., C. Prati, and F. Rocca (2000b, November). Process for radar measurements of the movement of city areas and landsliding zones. International Application Published under the Patent Cooperation Treaty (PCT).
- Ferretti, A., C. Prati, and F. Rocca (2001, January). Permanent scatterers in SAR interferometry. *IEEE Transactions on Geoscience and Remote Sensing* 39(1), 8–20.
- Gatelli, F., A. Monti Guarnieri, F. Parizzi, P. Pasquali, C. Prati, and F. Rocca (1994, July). The wavenumber shift in SAR interferometry. *IEEE Transactions on Geoscience and Remote Sensing* 32(4), 855–865.
- Geudtner, D. (1995). *Die Interferometrische Verarbeitung von SAR-Daten des ERS-1*. Ph. D. thesis, Universität Stuttgart. Draft.
- Gradshteyn, I. S., I. M. Ryzhik, and A. Jeffrey (1994). *Table of integrals, series, and products* (5 ed.). Boston: Academic Press. Original Title: Tablitsy integralov, summ, ryadov i proizvediniy, 1965.
- Hanssen, R. (2004). Stochastic modeling of time series radar interferometry. In *International Geoscience and Remote Sensing Symposium, Anchorage, Alaska, 20–24 September 2004*, pp. cdrom, 4 pages.

- Hanssen, R. F. (2001). *Radar Interferometry: Data Interpretation and Error Analysis*. Dordrecht: Kluwer Academic Publishers.
- Hanssen, R. F., F. J. van Leijen, and G. van Zwieten (2008). *Bodemdeling Kennemerland waargenomen met satelliet radarinterferometrie (InSAR)*, Chapter xx. In Barends et al. Barends et al. (2008).
- Henderson, F. M. and A. J. Lewis (Eds.) (1998). *Principles and applications of Imaging Radar* (3 ed.), Volume 2 of *Manual of Remote Sensing*. New York: John Wiley & Sons, Inc.
- Hoogheemraadschap Hollands Noorderkwartier (2008, October). Toets overschrijdingskans Hondsbossche en Pettemer zeewering (Review of the exceedance probability of the Hondsbossche and Pettemer water defense structure). Technical report.
- Hooper, A., H. Zebker, P. Segall, and B. Kampes (2004, December). A new method for measuring deformation on volcanoes and other non-urban areas using InSAR persistent scatterers. *Geophysical Research Letters* 31, L23611, doi:10.1029/2004GL021737.
- Humme, A. (2007, December). Point density optimization for SAR interferometry; a study tested on salt mine areas. Master's thesis, Delft University of Technology.
- JPL (2008). Jet Propulsion Laboratory. <<http://www.jpl.nasa.gov/>> Accessed October 2008.
- Kampes, B. and S. Usai (1999). Doris: the Delft Object-oriented Radar Interferometric Software. In *2nd International Symposium on Operationalization of Remote Sensing, Enschede, The Netherlands, 16–20 August, 1999*.
- Kampes, B. M. (2005, September). *Displacement Parameter Estimation using Permanent Scatterer Interferometry*. Ph. D. thesis, Delft University of Technology, Delft, the Netherlands.
- Kampes, B. M. and R. F. Hanssen (2004, November). Ambiguity resolution for permanent scatterer interferometry. *IEEE Transactions on Geoscience and Remote Sensing* 42(11), 2446–2453.
- Kampes, B. M., R. F. Hanssen, and Z. Perski (2003). Radar interferometry with public domain tools. In *Third International Workshop on ERS SAR Interferometry, 'FRINGE03', Frascati, Italy, 1–5 Dec 2003*, pp. 6 pp.
- Ketelaar, G., F. van Leijen, P. Marinkovic, and R. Hanssen (2005). Initial point selection and validation in PS-InSAR using integrated amplitude calibration. In *International Geoscience and Remote Sensing Symposium, Seoul, Korea, 25–29 July 2005*, pp. 5490–5493.
- Ketelaar, V. B. H. (2008, September). *Monitoring surface deformation induced by hydrocarbon production using satellite radar interferometry*. Ph. D. thesis, Delft University of Technology, Delft, the Netherlands.
- Li, F. K. and R. M. Goldstein (1990, January). Studies of multibaseline spaceborne interferometric synthetic aperture radars. *IEEE Transactions on Geoscience and Remote Sensing* 28(1), 88–97.
- Lim, H., W. Xu, and X. Huang (1995). Two new practical methods for phase unwrapping. In *International Geoscience and Remote Sensing Symposium, Florence, Italy, 10–14 July 1995*, pp. 196–198.

- Marinkovic, P., G. Ketelaar, F. van Leijen, and R. Hanssen (2008). InSAR quality control: Analysis of five years of corner reflector time series. In *Fifth International Workshop on ERS/Envisat SAR Interferometry, 'FRINGE07', Frascati, Italy, 26 Nov-30 Nov 2007*, pp. 8 pp.
- Massonnet, D. and K. L. Feigl (1998, November). Radar interferometry and its application to changes in the earth's surface. *Reviews of Geophysics* 36(4), 441–500.
- Massonnet, D. and H. Vadon (1995, March). ERS-1 internal clock drift measured by interferometry. *IEEE Transactions on Geoscience and Remote Sensing* 33(2), 401–408.
- Prati, C. and F. Rocca (1994, January). Use of the spectral shift in SAR interferometry. In *Second ERS-1 Symposium—Space at the Service of our Environment, Hamburg, Germany, 11–14 October 1993*, ESA SP-361, pp. 691–696.
- Rosen, P., S. Hensley, I. R. Joughin, F. K. Li, S. Madsen, E. Rodríguez, and R. Goldstein (2000, March). Synthetic aperture radar interferometry. *Proceedings of the IEEE* 88(3), 333–382.
- Sandwell, D. T. and E. J. Price (1998, December). Phase gradient approach to stacking interferograms. *Journal of Geophysical Research* 103(B12), 30183–30204.
- Sandwell, D. T. and L. Sichoix (2000). Topographic phase recovery from stacked ERS interferometry and a low resolution digital elevation model. *Journal of Geophysical Research* 105(B12), 28211–28222.
- Scharroo, R. and P. Visser (1998). Precise orbit determination and gravity field improvement for the ERS satellites. *Journal of Geophysical Research* 103(C4), 8113–8127.
- Schreier, G. (Ed.) (1993). *SAR Geocoding: data and systems*. Karlsruhe: Wichmann Verlag.
- SCR (1993, september). Ceos sar calibration workshop. ESTEC, Noordwijk, Netherlands.
- Stimson, G. W. (1998). SciTech Publishing.
- Swart, L. M. T. (2000, December). Spectral filtering and oversampling for radar interferometry. Master's thesis, Faculty of Geodetic Engineering, Delft University of Technology.
- Teunissen, P. J. G. (1993). Least-squares estimation of the integer GPS ambiguities. In *Invited Lecture, Section IV Theory and Methodology, IAG General Meeting, Beijing, China, august 1993*. Also in: Delft Geodetic Computing Centre, LGR Series, No. 6, 1994.
- Teunissen, P. J. G. (1995). The least-squares ambiguity decorrelation adjustment: a method for fast GPS integer ambiguity estimation. *Journal of Geodesy* 70(1-2), 65–82.
- Teunissen, P. J. G. (1999). A theorem on maximizing the probability of correct integer estimation. *Artificial Satellites* 34(1), 3–9.
- Teunissen, P. J. G. (2000). *Adjustment theory; an introduction* (1 ed.). Delft: Delft University Press.
- Teunissen, P. J. G. (2001a). *Dynamic data processing; recursive least-squares* (1 ed.). Delft: Delft University Press.
- Teunissen, P. J. G. (2001b). Integer estimation in the presence of biases. *Journal of Geodesy* 75, 399–407.

- Transport and Water Management Inspectorate (2006). Primaire waterkeringen getoetst (Primary water defense structures tested). Technical report.
- Usai, S. (1997). The use of man-made features for long time scale insar. In *International Geoscience and Remote Sensing Symposium, Singapore, 3–8 Aug 1997*, pp. 1542–1544.
- Usai, S. and R. Hanssen (1997). Long time scale INSAR by means of high coherence features. In *Third ERS Symposium—Space at the Service of our Environment, Florence, Italy, 17–21 March 1997*, pp. 225–228.
- van Leijen, F. J., A. J. M. Humme, and R. F. Hanssen (2008). *Deformatie van de Hondsbossche en Pettemer zeewering geconstateerd met radarinterferometrie*, Chapter 4.5. In Barends et al. (2008).
- Wiley, C. A. (1954, Filed August). Pulsed Doppler radar methods and apparatus. *United States Patent, No. 3196436*.
- Williams, S., Y. Bock, and P. Fang (1998). Integrated satellite interferometry: Tropospheric noise, GPS estimates and implications for interferometric synthetic aperture radar products. *Journal of Geophysical Research* 103(B11), 27,051–27,067.
- Woodward, P. M. (1953). *Probability and Information Theory, with Applications to Radar*. London: Pergamon.
- Xu, W. and I. Cumming (1999, January). A region-growing algorithm for InSAR phase unwrapping. *IEEE Transactions on Geoscience and Remote Sensing* 37(1), 124–134.
- Zebker, H. (1996). Imaging radar and applications. Class notes EE355.
- Zebker, H. A., P. A. Rosen, R. M. Goldstein, A. Gabriel, and C. L. Werner (1994, October-10). On the derivation of coseismic displacement fields using differential radar interferometry: The Landers earthquake. *Journal of Geophysical Research* 99(B10), 19617–19634.
- Zebker, H. A., P. A. Rosen, and S. Hensley (1997, April). Atmospheric effects in interferometric synthetic aperture radar surface deformation and topographic maps. *Journal of Geophysical Research* 102(B4), 7547–7563.
- Zebker, H. A. and J. Villasenor (1992, September). Decorrelation in interferometric radar echoes. *IEEE Transactions on Geoscience and Remote Sensing* 30(5), 950–959.
- Zuidweg, B. (1997). *De verhoging van de Hondsbossche zeewering*. Pirola.



## Appendix A

# Fourier Transform and Convolution

This appendix serves as background information on continuous fourier transforms and convolution, as used in section 3.2. More information and proofs on continuous fourier transforms and convolution can be found in most books on advanced mathematics. Here only the equations and conditions are given for the continous case, without any proofs, and for unitary frequencies.

### A.1 Continous Fourier Transform

The fourier transform is a complex integral transformation of a function that produces another function depending on differet variables. It is a generalization of the complex fourier series, an expansion of a periodic function in sines and cosines. A signal in space or time  $x(t)$  can be presented in the frequency domain or spectrum, giving a frequency distribution  $X(f)$ . The continous fourier transform ( $\mathcal{F}$ ) of a function with unitary frequency (Hz) is the pair

$$\begin{aligned} X(f) &= \mathcal{F}[x(t)](f) \\ &= \int_{-\infty}^{\infty} x(t)e^{-2\pi i f t} dt \end{aligned} \tag{A.1}$$

$$\begin{aligned} x(t) &= \mathcal{F}^{-1}[X(f)](t) \\ &= \int_{-\infty}^{\infty} X(f)e^{2\pi i f t} df \end{aligned} \tag{A.2}$$

provided that

1.  $\int_{-\infty}^{\infty} |f(x)|dx$  exists.
2. There are a finite number of discontinuities.
3. The variation is bounded (or sufficiently, if the Lipschitz condition is fulfilled).

## A.2 Convolution

The convolution is an integral that expresses the amount of overlap of a function  $g$  shifted over a function  $f$ . The convolution of two functions simplifies to a multiplication, when the functions are (fourier) transformed. The transform of a product is generally different from the product of the transforms of its factors. This is unlike addition of two transforms, which is simply the addition of the transforms of the factors

$$\mathcal{F}(f + g) = \mathcal{F}(f) + \mathcal{F}(g) \quad (\text{A.3})$$

$$\mathcal{F}(fg) \neq \mathcal{F}(f)\mathcal{F}(g) \quad (\text{A.4})$$

The multiplication of two transforms is the transform of the convolution of its factors

$$h(t) = (f \otimes g)(t) = \int_0^t f(\tau)g(t - \tau)d\tau \quad (\text{A.5})$$

$$= \int_0^t g(\tau)f(t - \tau)d\tau \quad (\text{A.6})$$

with  $\otimes$  the convolution operator. This is true provided that

1.  $f$  and  $g$  are piecewise continuous.
2. There are finite number of discontinuities
3. The growth condition  $|f(t)| \leq Me^{kt}$  is satisfied for all  $t \geq 0$  and some constants  $M$  and  $k$ .



## Appendix B

# Envisat ASAR Dataset

This addenda serves as a reference to the Envisat ASAR dataset used within this study. All images were acquired from track 423, in the descending orbit.

Aqcuisition date	Orbit nr.	Btemp [days]	Bperp [m]
19-Mar-2003	05487	-875	155.9
02-Jul-2003	06990	-770	-332.8
06-Aug-2003	07491	-735	-386.3
10-Sep-2003	07992	-700	355.6
15-Oct-2003	08493	-665	863.6
19-Nov-2003	08994	-630	-828.9
24-Dec-2003	09495	-595	351.6
28-Jan-2004	09996	-560	764.7
03-Mar-2004	10497	-525	-178.1
07-Apr-2004	10998	-490	939.6
12-May-2004	11499	-455	-408.3
16-Jun-2004	12000	-420	124.0
21-Jul-2004	12501	-385	340.4
25-Aug-2004	13002	-350	194.1
29-Sep-2004	13503	-315	-526.0
03-Nov-2004	14004	-280	217.9
08-Dec-2004	14505	-245	190.2
12-Jan-2005	15006	-210	-530.7
16-Feb-2005	15507	-175	-321.5
23-Mar-2005	16008	-140	-741.5
27-Apr-2005	16509	-105	535.8
01-Jun-2005	17010	-70	-66.9
06-Jul-2005	17511	-35	727.0
10-Aug-2005	18012	0	0

Acquisition date	Orbit nr.	Btemp [days]	Bperp [m]
19-Oct-2005	19014	70	193.8
23-Nov-2005	19515	105	391.2
28-Dec-2005	20016	140	413.6
01-Feb-2006	20517	175	-500.2
08-Mar-2006	21018	210	245.6
12-Apr-2006	21519	245	-425.6
17-May-2006	22020	280	-69.9
21-Jun-2006	22521	315	240.4
26-Jul-2006	23022	350	801.9
30-Aug-2006	23523	385	726.9
04-Oct-2006	24024	420	-659.4
08-Nov-2006	24525	455	-403.5
17-Jan-2007	25527	525	761.5
21-Feb-2007	26028	560	214.5
28-Mar-2007	26529	595	664.3
02-May-2007	27030	630	-85.1
06-Jun-2007	27531	665	114.7
11-Jul-2007	28032	700	43.9
15-Aug-2007	28533	735	132.4
19-Sep-2007	29034	770	681.6
24-Oct-2007	29535	805	-120.3
28-Nov-2007	30036	840	422.6
02-Jan-2008	30537	875	-320.8
06-Feb-2008	31038	910	366.9
12-Mar-2008	31539	945	75.9
16-Apr-2008	32040	980	464.9
21-May-2008	32541	1015	85.4

Table B.1: Envisat ASAR dataset

# Appendix C

## Algorithm construction

To show in short an overview of the algorithm, this is put into pseudo-code. This is a readable format in which the decisions during the algorithm are presented.

Before the code is initiated, the following steps must have been performed:

1. Processing in DORIS to coregister the SLC images, crop the images and form the interferograms.
2. Downloading of the data in the required format. For this a small script was programmed, which included the conventional PSI results for later comparison. It further cropped the area, to only include the area of interest.
3. Masking to only include the area of interest. For this a short script was modified, and some additional helpful steps were implemented.

The data and mask are used as input variables for the algorithm. Other general parameters must be set, which include the number of seeds, the temporal coherence threshold, the temporal coherence reduction stepsize, the kernel size, the number of layers in the kernel, the final crop size, and assumptions for the covariance matrix. With these inputs, the pseudo-code on the following page is executed

The pseudo-code for the implemented algorithm reads:

```

For maximum temporal coherence TO minimum coherence threshold
  For minimum number of layers TO maximum number of layers
    While there are still flags present with Flag = 1
      For all pixels in the kernel
        Estimation of the selected PS
        If temporal coherence > threshold
          Switch flag
            Flag == 0
              Integrate estimations
            Flag == 1
              If region numbers are unequal
                Merge regions
              End
            Flag == 3
              Integrate estimations
          End
        Else If temporal coherence < threshold AND Flag ≠ 1 AND Flag ≠ 2
          Set Flag = 3
        End
      End
    End
  Reset Flags
End
End

```